行政院國家科學委員會專題研究計畫 成果報告

低成本之光學感測器研發及應用於碳氫火焰量測(第 2 年)
研究成果報告(完整版)

計畫類別：個別型
計畫編號：NSC 95-2221-E-216-018-MY2
執行期間：96年08月01日至97年08月31日
執行單位：中華大學機械與航太工程研究所

計畫主持人：鄭藏勝

計畫參與人員：碩士班研究生-兼任助理人員：鄭雅云
碩士班研究生-兼任助理人員：簡毓倩
碩士班研究生-兼任助理人員：陳瑜偉
碩士班研究生-兼任助理人員：陳永軒
博士班研究生-兼任助理人員：李約亨
博士班研究生-兼任助理人員：張智國
博士班研究生-兼任助理人員：周中祺
博士後研究：吳志勇

報告附件：出席國際會議研究心得報告及發表論文

處理方式：本計畫涉及專利或其他智慧財產權，2年後可公開查詢

中 華 民 國 97年11月11日

行政院國家科學委員會補助專題研究計畫 ■ 成果報告
□期中進度報告

低成本之光學感測器研發及應用於碳氫火焰量測
Development of Low Cost Optical Sensors for Hydrocarbon Flame Measurement

計畫類別：■ 個別型計畫 □ 整合型計畫
計畫編號：NSC 95－2221－E －216－018－MY2
執行期間： 95 年 8 月 1 日至 97 年 8 月 31 日

計畫主持人：鄭藏勝 教授
共同主持人：
計畫參與人員：趙怡欽 教授、吳志勇(博士後研究員)、李約亨(博士生)、張智國(博士生)、鄭雅云(碩士生)、簡毓倩(碩士生)、陳瑜偉(碩士生)、周中祺(博士生)、陳永軒(碩士生)

成果報告類型(依經費核定清單規定繳交)：□精簡報告 ■完整報告

本成果報告包括以下應繳交之附件：
□赴國外出差或研習心得報告一份
□赴大陸地區出差或研習心得報告一份
■出席國際學術會議心得報告及發表之論文各一份
□國際合作研究計畫國外研究報告書一份

處理方式：除產學合作研究計畫、提升產業技術及人才培育研究計畫、列管計畫及下列情形者外，得立即公開查詢
□涉及專利或其他智慧財產權，□一年■二年後可公開查詢

執行單位：中華大學機械與航太工程研究所

中 華 民 國 97 年 11 月 9 日

ACKNOWLEDGEMENTS

This research was supported by the National Science Council of Taiwan, Republic of China under the grant number NSC 95-2221-E-216-018-MY2. The computer time was provided by the National Center for High-performance Computing, Taiwan, ROC.

中文摘要

本計畫以二年的時間研發可同時量測紊流預混甲烷火焰當量比及溫度之低成本無雷射光學感測器，為了研發低成本的量測工具，本研究重新設計卡塞格倫反射鏡之鏡座使其具有微米級之焦聚調整精度，並與光纖集光器結合成一體。此外，也自行設計含有二色鏡、濾光鏡及光電增倍管之 CH*、OH*及 C_2*(0, 0)自然螢光分析儀並完成組裝測試。除了自行設計的自然螢光分析儀之外，我們也利用光譜儀結合液態氮冷卻之 CCD 照相機進行自然螢光量測。兩種自然螢光量測儀皆被應用於層流預混本生火焰的量測並進行系統校正，而所量測之最大 C_2*/CH*、C_2*/OH*及 CH*/OH*螢光比值也皆隨著當量比呈線性關係，惟吾人發現，雖然搭配光電增倍管之自然螢光分析儀具有快速的數據存取率，但無法濾除因 CO_2*螢光造成之訊號干擾，而光譜儀搭配液態氮冷卻之 CCD 照相機雖然數據存取率較慢，但可同時量測波長從 250 nm 到 650 nm 之所有 OH*、CH*、C_2*(1, 0)、C_2*(0, 0)、C_2*(0, 1)及 CO_2*螢光光譜，所以由 CO_2*螢光造成之訊號干擾可由後續之數據處理中剔除，同時 C_2*(1, 0)及 C_2*(0, 0)之螢光比值亦可作為溫度量測。因此，本研究最後採用卡塞格倫反射鏡及光纖集光器與光譜儀搭配液態氮冷卻之 CCD 照相機進行系統校正，並將於層流預混本生火焰校正所得之最大 C_2*/CH*、C_2*/OH*及 CH*/OH*螢光比值與當量比關係式及溫度較正常數應用於紊流預混甲烷火焰，以驗證本研究所研發之感測器可同時量測紊流預混甲烷火焰之當量比及溫度，而本研究之最終目標則是發展無雷射之光學感測器作為工業燃燒爐及焚化爐等之即時主動監控感測器。

關鍵詞：光學感測器、自然螢光、當量比、火焰溫度

Abstract

The objective of this research is to develop a low cost, robust, non-laser based optical sensor and to apply this sensor for simultaneous measurements of local equivalence ratio and temperature in turbulent premixed hydrocarbon flames. The sensor system uses Cassegrain optics to eliminate the chromatic aberrations and to improve the spatial resolution for light collection. Two types of light detection units, one is the spectroscopic unit with the PMT array and the other is the spectrometer with the LN-CCD camera, are tested in the experiments to verify their applicability. Both types of light detection units are applied to the laminar premixed flames to demonstrate the capability of the light detection units for chemiluminescence emission measurements. The PMT array provides fast data acquisition rate for chemiluminescence emission measurements but gives no information on the broadband CO_2* emissions. On the other hand, the LN-CCD camera measures the entire spectral range of OH*, CH*, C_2*(1, 0), C_2*(0, 0), C_2*(0, 1) as well as the broadband CO_2* emissions but gives slow data acquisition rate (about 1.5 s per image frame). Although the LN-CCD camera gives slow data acquisition rate, the simultaneous measurements of C_2*(1, 0) and C_2*(0, 0) emissions provide a method for flame temperature measurement using the intensity ratio of C_2*(1, 0)/C_2*(0, 0). Therefore, the linear relationship between the C_2*/CH*, C_2*/OH*, and CH*/OH* intensity ratios and equivalence ratio as well as the instrument constant obtained by the spectrometer coupled with the LN-CCD camera are used for simultaneous measurements of equivalence ratio and flame temperature in turbulent premixed CH_4-air flames to demonstrate the capability of the developed optical sensor. The final goal of the research is to apply the developed inexpensive, non-laser based optical sensor system for real-time active control in industrial burners and hazardous waste incinerators.

Keywords: Optical sensor, Chemiluminescence emission, Equivalence ratio, Flame temperature

CONTENTS

LIST OF TABLES

LIST OF FIGURES

CHAPTER I
INTRODUCTION

1.1 Background

According to the energy consumption report [1], the amount of energy (77,875 KLOE) consumed by the industrial and transportation sectors was 72.1% of the total annual energy consumption in Taiwan during the year of 2007. In these two sectors, about 90% of energy sources (fossil fuels) were used to generate power, process heat, and electricity through combustion. In order to burn the fuel more efficiently and effectively, the development of combustion heating and energy saving technologies is of vital importance. Although the Energy and Resources Laboratories (ERL), ITRI has devoted much efforts to improve the energy efficiency of industrial process heating [2], there are still many combustion related technologies that need to be developed. Also, from the academic point of view, the continuous support of fundamental scientific research and educating students is the essential way to achieve the goal of building up our own combustion technology.

Various types of turbulent flames, premixed, nonpremixed, or partially premixed, are employed in industrial boilers, process heating burners, internal combustion engines, hazardous waste incinerators, and both aircraft and land-based gas turbine engine combustors, etc. In order to control the turbulent combustion [3, 4] for reducing pollutant emission [5-7], increasing combustion efficiency [8], and obtaining stable flame holding [9-11], the detailed compositional structures at turbulent flame-front must be known. In addition, quantitative measurements of reaction zone structure, velocity, temperature, species concentration, flame curvature, and stretch rate in turbulent flames would provide valuable information that not only allow a better understanding of the physics underlines but also improve the applicability of combustion models. In order to quantitatively, spatially, and temporally resolve the turbulent flames, sophisticate laser diagnostic techniques are generally needed.

Laser-induced fluorescence (LIF) technique is a very powerful tool to visualize the reaction zone structures [12-14] and its time evolution [15] in turbulent flames through the excitation of OH and CH radicals from their ground electronic states. LIF can provide useful 2-D information on flame shape and flame front structure, but time-series analysis of the flame front motion is difficult because of the laser repetition rate. Velocity measurements in turbulent flames can be made using laser Doppler velocimetry (LDV) or particle imaging velocimetry (PIV) to acquire 1-D [16-18] or 2-D [19-22] velocity fields, respectively. Flame curvature and strain rate can be deduced using simultaneous OH and CH imaging and PIV techniques [23, 24]. It has been shown that the spontaneous vibrational Raman scattering coupled with LIF techniques can provide simultaneous temperature, major, and minor species concentration measurements [25-28]. The effect of turbulence-chemistry interaction on finite-rate chemistry, pollutant emissions, and liftoff and blowout mechanisms can be understood from Raman/LIF measurements.

Literature survey indicates that more advanced instruments, such as high power lasers, spectrometers, intensified CCD (ICCD) cameras, fast data acquisition systems, and so on, are required in order to obtain more information non-intrusively from turbulent combustion. These measurements are usually named as “noble experiments”. It is well known that the research budget would be cut more and more in the coming years due to an increased budget in Defense sector. Thus, the development of low cost, non-laser based optical sensors for turbulent hydrocarbon flames measurements is an alternative to continuous building up our own localized combustion technology.

1.2 Motivations and Objectives

There are a number of optical methods that can give information about the combustion process non-intrusively, e.g., optical emission, absorption, fluorescence, and other spectroscopic methods. The focus of this research is on the simplest of all these techniques, viz., observing the naturally occurring, optical emissions from the turbulent flames. While there are a number of sources for optical radiation from a flame, the source most directly connected to the combustion reactions is chemiluminescence. The chemiluminescence emissions are from electronically excited states of molecules (e.g., $\mathrm{OH}^*[A^2\Sigma^+ \rightarrow X^2\Pi]$, $\mathrm{CH}^*[A^2\Delta \rightarrow X^2\Pi]$, and $\mathrm{C}_2^*[d^3\mathit{\Pi} \rightarrow a^2\mathit{\Pi}]$) that are produced by chemical reactions. The excited molecules will transfer to lower energy states, in part by emitting light. This is known as chemiluminescence. Since the intensity of emission is proportional to the chemical production rate of the particular molecule, the chemiluminescence intensity can be related to chemical reaction rates [29]. For this reason, chemiluminescence has been used previously as a rough measure of reaction rate and heat release rate [30-35]. Thus, chemiluminescence can provide information on the presence and strength of the combustion process in a specific region of the combustor, making it well-suited for diagnostics and flame monitoring.

Since the chemiluminescence intensities are produced during the chemical reaction process, the light intensity is related to the rate of production/consumption of that species. The reaction rate varies with reaction pathways which is a function of equivalence ratio, making it easier to deduce the equivalence ratio from the chemiluminescence intensity. It has been shown that the ratio of OH*/CH*, C_2*/OH*, and C_2*/CH* vary with equivalence ratio in laminar premixed flames [36]. This non-laser based diagnostic technique has been applied to turbulent premixed flames for local flame-front structure measurement [37], to high-pressure laminar flame for local spectral measurement [38], to premixed-spray flame for observation of droplet group combustion behavior [39], to an atmospheric pressure micro-gas turbine combustor for detecting local equivalence ratio [40], to gas turbine combustors for developing optical equivalence ratio sensors [41], to turbulent premixed flames for flame-front motion analysis [42], and to gas turbine engines for active control [43].

Although the application of optical emission technique is being quite successful for various type of reacting flow measurements, simultaneous measurements of local equivalence ratio (mixture fraction) and temperature using chemiluminescence emissions from turbulent flames have not been reported. It has been the goal of considerable research effort to find universal state relationship for temperature and species concentrations as functions of a single variable, the mixture fraction, in order to create flamelet libraries for use in the modeling of turbulent combustion. However, in order that the comparison of experimental and computational data set is to be meaningful, both the mixture fraction and at least one additional variable, such as temperature, must be match in some fashion.

The objectives of this research project are to develop a low cost, robust, non-laser based optical sensor system and to apply this system for simultaneous temperature and equivalence ratio (mixture fraction) measurements in hydrocarbon flames.

CHAPTER II
RESEARCH METHODS

2.1 Experimental Setup

In order to gain a better understanding of the physics of turbulent flames and their associated pollutant emission mechanisms, the thermophysical properties of the flames must be measured. Simultaneous multi-point measurements of temperature, species concentration, mixture fraction, and hence scalar dissipation rate have been made in turbulent jet flames using line-Raman/LIPF techniques [44, 45]. However, these techniques require expansive equipments such as narrowband excimer lasers, spectrometers, and ICCD cameras. For example, the Combustion Research Facility at Sandia National Laboratories, Livermore, California, USA used ***four lasers, one spectrometer, and six ICCD cameras*** (see Fig. 1) to measure flame orientation and scalar dissipation in turbulent partially premixed flames [46]. This type of experiment is out of our research funding capability. Thus in this work, a much simpler and cheaper method is used to accomplish the same job. That is chemiluminescence optical sensor.

In the past, most of the chemiluminescence measurements used typical collecting lenses to monitor global emissions along the line-of-sight, and hence there was insufficient spatial resolution to detect the local flame-front structure. The use of a 2-D chemiluminescence imaging system can overcome this problem [33, 48]. However, it is difficult to apply this technique to obtain chemical information about the local flame-front in turbulent premixed flames. Therefore, an optical measurement technique using spatially designed Cassegrain optics to detect local flame emissions has been reported [49]. The schematic diagram of the Cassegrain optics is shown in Fig. 2. The Cassegrain optics consists of a primary and a secondary mirror, which avoids the generation of chromatic aberrations for different wavelengths. The Cassegrain optics is designed by the ray-tracing method. The designed rms spot size of Cassegrain optics is 328 μm and the magnification ratio is 2.36. In order to improve the Cassegrain optics for a micro-level adjustment and to connect with the optical fiber for light collection, the optical holder is re-designed. In addition, a circular mask with different slit widths at the center can be placed in front of Cassegrain optics at the secondary mirror so that the background flame emission signals located away from the effective sample volume is minimized [50].

The schematic diagram and photograph of the measurement system are shown in Fig. 3. Chemiluminescence signals emanating from the sample volume are collected and focused by the Cassegrain optics and relayed to the entrance slit of a spectroscopic unit through a 2-m long optical fiber (core diameter = 100 μm). A collimated lens is coupled to the end of optical fiber for expanding the light rays. In the spectroscopic unit, three dichroic mirrors are used to separate different wavelengths of optical emissions. Particular regions of wavelength corresponding to OH*, CH*, and C_2* are extracted through the narrowband interference filters and detected by the side-on type photomultiplier tubes (PMTs). The specifications (center wavelength/full width at half maximum) of the interference filters for OH*, CH*, and C_2* are 307.3/22.2 nm, 432.1/10.5 nm, and 516.3/8.5 nm, respectively. The current output from the PMTs are simultaneously amplified and digitized with a 12-bit A/D converter. The output signals are stored in a personal computer for data reduction.

It is noted that although the use of PMTs for chemiluminescence measurements poses faster data acquisition rate than that of a 2D detector such as a CCD camera, the PMT provides no information on the emission spectra of OH*, CH*, and C_2*. Therefore, in addition to the spectroscopic unit, a monochromator (Spectral Products, DSK 242, 1/4 m, *f*/# = 3.9) coupled with liquid nitrogen cooled charge-coupled device (LN-CCD) is also employed in the present study. The photograph of measurement system is shown in Fig. 4.

2.2 Bunsen Burner

A Bunsen type jet burner (i.d. = 10 mm) is used to produce laminar premixed methane-air flames operated at several different equivalence ratios ranging from fuel-lean to fuel-rich conditions (ϕ = 0.85-1.5) for the emission measurements and system calibration. To generate the laminar premixed flames, the exit velocity of the flow is kept at 1 m/s so that the flowrates of fuel and air are varied. The operation conditions of the laminar premixed flames are listed in Table 1. For turbulent premixed flames, a larger diameter jet burner (i.d. = 20 mm) is employed. Typical flame features for laminar and turbulent premixed CH_4/air flames at $\phi = 1.0$ are shown in Fig. 5.

CHAPTER III
THEORETICAL BACKGROUND OF VIBRATIONAL TEMPERATURE MEASUREMENT

3.1 Vibrational Temperature Measurement

The flame temperature can be measured using the intensity ratio of C_2* emission intensities at two vibrational bands as proposed by Ishiguro et al. [51]. Fig. 6 shows the typical emission spectra of the two C_2* bands [51]. The intensity ratio I_1/I_2 of the two vibrational bands is given by

$$\frac{I_{ip}}{I_2} = \frac{\sum_i v_u A_{rel,i} \exp(-E_i / kT)}{\sum_j v_j A_{rel,j} \exp(-E_j / kT)} \tag{1}$$

where v is the frequency, A_{rel} the relative Einstein transition probability for spontaneous emission, E the upper vibrational energy (erg), k the Boltzmann constant, T the vibrational temperature (K), and p a constant for the instrument. The subscripts i and j indicate the individual emission lines of the two vibrational bands. The vibrational energy for the vibrational quantum number υ', $E_{\upsilon'}$ is given by the following [52]:

$$E_{\upsilon'} = hc\omega_e\left(\upsilon + \frac{1}{2}\right) - hc\omega_e x_e\left(\upsilon + \frac{1}{2}\right)^2 + hc\omega_e y_e\left(\upsilon + \frac{1}{2}\right)^3 - \text{-----} \tag{2}$$

Here ω_e is the vibrational wave number, x_e and y_e are the anharmonicity constants. For $\upsilon' \rightarrow \upsilon''$, the transition probability $A_{\upsilon',\upsilon''}$ is expressed by the following [52]:

$$A_{\upsilon',\upsilon''} \propto \left[\int \psi_{\upsilon'} \psi_{\upsilon''}\, dx\right]^2 \tag{3}$$

For a harmonic oscillator ψ_υ is given by [52]:

$$\psi_\upsilon = N_\upsilon \exp\left(-\frac{1}{2}\alpha x^2\right) H_\upsilon\left(\alpha^{1/2} x\right) \tag{4}$$

where N_υ is the normalization constant,

$$N_\upsilon = \left(2^\upsilon \upsilon!\right)^{-1/2} (\alpha / \pi)^{1/4} \tag{5a}$$

$$\alpha = 4\pi^2 \mu v_0 / h = 2\pi(\mu k)^{1/2} / h \tag{5b}$$

μ is the reduced mass of the molecules and equals $m_1 m_2 / (m_1 + m_2)$, and H_υ is the Hermite polynomial of the υth degree and is given as

$$H_0(X) = 1$$

$$H_1(X) = 2X$$

$H_2(X) = 4X^2 - 2$

$H_3(X) = 8X^3 - 12X$

$H_3(X) = 8X^3 - 12X$

$H_4(X) = 16X^4 - 48X^2 + 12$

$X = \alpha^{1/2}x.$

$A_{rel,\upsilon',\upsilon''}$ is calculated as the ratio of $A_{\upsilon',\upsilon''}$ to $A_{0,0}$:

$$A_{rel,\upsilon',\upsilon''} = A_{\upsilon',\upsilon''} / A_{0,0} \tag{6}$$

The instrument constant *p* can be determined from the calibration and the values of λ, (υ',υ''), $E_{\upsilon',\upsilon''}$ and $A_{rel,\upsilon',\upsilon''}$ for the band components are listed in Table 2.

The method of vibrational temperature measurement described by Ishiguro et al. [51] involves many calculations of spectral properties. It seems that the summation of emission intensity for each vibration band has to be made by summing over all the vibrational state and the temperature is determined by comparing the calculated spectra with the measured ones. Moreover, it is not clear where the calibration constant *p* is involved in Eq. (1). Therefore, we decided to derive the relation of intensity ratio with the flame temperature based on fundamental theory of emission.

3.2 Theory of Vibrational Temperature Measurement

The intensity of a spectral line in emission I_{em}^{nm} is defined as the energy emitted by the source per second. If there are N_n atoms in the initial state and if A_{nm} is the fraction of atoms in the initial state carrying out the transition to *m* per second then [52]

$$I_{em}^{nm} = N_n hc\nu_{nm} A_{nm} \tag{7}$$

where *h* is the Planck constant, *c* is the speed of light, and $hc\nu_{nm}$ is the energy of each light quantum of wave number ν_{nm} emitted in the transition. A_{nm} is the Einstein transition probability of spontaneous emission which is related to the matrix element of the transition as follows:

$$A_{nm} = \frac{64\pi^4\nu_{nm}^3}{3h}\left|R^{nm}\right|^2 \tag{8}$$

For the band emission from higher vibrational levels υ′ to lower vibrational levels υ″, Eq. (7) can be expressed as [52]:

$$I_{em}^{\upsilon'\upsilon''} = \frac{64}{3}\pi^4 N_{\upsilon'} c \nu^4 \left(R_{vib}^{\upsilon'\upsilon''}\right)^2 \left[\int \psi_{\upsilon'}\psi_{\upsilon''} dr\right]^2 \tag{9}$$

where $N_{\upsilon'}$ is the number of molecules in the upper vibrational levels, $R_{vib}^{\upsilon'\upsilon''}$ is the vibrational transition moment, and ψ_{υ} is the vibrational eigenfunction. If we sum the transition probability over all transitions that can occur from a given vibrational level, we obtain on account of the sum rules [52]

$$\sum_{\upsilon'} \left|R_{vib}^{\upsilon'\upsilon''}\right|^2 = 1, \quad \sum_{\upsilon'} \left[\int \psi_{\upsilon'}\psi_{\upsilon''} dr\right]^2 = 1 \tag{10}$$

The total emission intensity from a band becomes

$$I = \sum_{\upsilon''} \frac{I_{em}^{\upsilon'\upsilon''}}{\nu^4} = \frac{64}{3}\pi^4 c \sum_{\upsilon'} N_{\upsilon'} \tag{11}$$

In thermal equilibrium the number of molecules in the upper vibrational state is

$$N_{\upsilon'} = \frac{N}{Q_{\upsilon}} e^{-G_0(\upsilon')hc/kT} \tag{12}$$

where Q_{υ} is the vibrational partition function and $G_0(\upsilon')$ is the energy term value above the zero-point energy. The vibrational partition function is defined as:

$$\begin{aligned} Q_{\upsilon} &\equiv \sum_{\upsilon=0}^{\infty} e^{-(\varepsilon_{\upsilon}-\varepsilon_{\upsilon 0})/kT} = \sum_{\upsilon=0}^{\infty} e^{-G_0(\upsilon)hc/kT} = \sum_{\upsilon=0}^{\infty} e^{-hc\omega_e \upsilon/kT} = \sum_{\upsilon=0}^{\infty} e^{-(T_{\upsilon}/T)\upsilon} \\ &= 1 + e^{-(T_{\upsilon}/T)} + e^{-2(T_{\upsilon}/T)} + \ldots \\ &= 1 + x + x^2 + \ldots\ldots = \frac{1}{1-x} \end{aligned} \tag{13}$$

where $x = e^{-T_{\upsilon}/T}$. Thus,

$$Q_{\upsilon} = \frac{1}{1-e^{-T_{\upsilon}/T}} \tag{14}$$

where the characteristic vibrational temperature T_{υ} is defined as

$$T_{\upsilon} = \frac{hc\omega_e}{k} \tag{15}$$

Substituting Eqs. (12) and (13) into Eq. (11), it becomes

$$I = \sum_{\upsilon''} \frac{I_{em}^{\upsilon'\upsilon''}}{\nu^4} = \frac{64}{3}\pi^4 c \frac{N}{Q_{\upsilon}} \sum_{\upsilon'} e^{-G_0(\upsilon')hc/kT} = \frac{C}{Q_{\upsilon}} \sum_{\upsilon'} e^{-G_0(\upsilon')hc/kT} \tag{16}$$

Note that C is the grouped constant.

Because the emission of C_2*(1, 0) band starts from υ′ = 1 and that of C_2*(0, 0) band starts from υ′ = 0, therefore the intensity ratio of the two vibrational bands can be expressed as:

$$\frac{I_{\Delta\upsilon=1}}{I_{\Delta\upsilon=0}} = \frac{C_1 \sum_{\upsilon'=1}^{\infty} e^{-G_0(\upsilon')hc/kT}}{C_2 \sum_{\upsilon'=0}^{\infty} e^{-G_0(\upsilon')hc/kT}} = \frac{C_1}{C_2} \frac{\sum_{\upsilon'=0}^{\infty} e^{-G_0(\upsilon')hc/kT} - 1}{\sum_{\upsilon'=0}^{\infty} e^{-G_0(\upsilon')hc/kT}} = \frac{C_1}{C_2} \frac{\dfrac{e^{-T_\upsilon/T}}{1-e^{-T_\upsilon/T}}}{\dfrac{1}{1-e^{-T_\upsilon/T}}} = C_3 e^{-T_\upsilon/T} \tag{17}$$

$$\ln(I_{ratio}) = \ln(C_3) - \frac{T_\upsilon}{T} \tag{18}$$

$$T = \frac{T_\upsilon}{\ln(C_3) - \ln(I_{ratio})} \tag{19}$$

where the characteristic vibrational temperature for C_2 is T_υ = 2572.89 K and C_3 is the instrument constant which can be determined from the calibration.

CHAPTER IV
NUMERICAL SIMULATION

4.1 Governing Equations

In the present study, numerical simulations of the laminar premixed CH_4/air flames using a commercial package CFD-ACE are also performed to investigate the flame structures. The governing equations of mass, momentum, energy, and chemical species for a steady axisymmetric reacting flow can be written in the cylindrical (r, x) coordinate system as

$$\nabla \cdot (\rho v) = 0 \tag{20}$$

$$\nabla \cdot (\rho v v) = -\nabla p + \nabla \cdot (\mu \nabla v) + \rho g_x \tag{21}$$

$$\nabla \cdot (\rho v T) = \frac{1}{c_p} \nabla \cdot (\lambda \nabla T) - \frac{1}{c_p} \sum_i h_i \left\{ w_i + \nabla \cdot [\rho D_i \nabla Y_i + \rho D_i^T \nabla (lnT)] \right\} \tag{22}$$

$$\nabla \cdot (\rho v Y_i) = \nabla \cdot [\rho D_i \nabla Y_i + \rho D_i^T \nabla (lnT)] + w_i \tag{23}$$

and the state equation

$$p = \rho R_0 T \sum_i \frac{Y_i}{M_i} \tag{24}$$

where ρ, p, T, Y, c_p, h, w, R_0, M, g_x, and $v = (u, \upsilon)$ are the density, pressure, temperature, mass fraction, specific heat capacity of the mixture, enthalpy, species production rate, universal gas constant, molecular weight, gravitational acceleration in x-direction, and velocity vector, respectively. μ, λ, and D are the viscosity, thermal conductivity, and mass diffusivity, respectively. The subscript i in equations (22)-(24) stand for the i-th chemical species. The second term in the bracket of equations (22) and (23) is the thermo-diffusion or Soret diffusion due to the effect of temperature gradient. The concentration-driven diffusion coefficient is calculated as:

$$D_i = \frac{1 - x_i}{\left[\sum_{j=1}^{N} \frac{x_j}{D_{ij}} \right]_{j \neq i}} \tag{25}$$

where D_{ij} is the binary diffusion coefficient. The binary mass diffusivity is determined by the Chapman-Enskog kinetic theory using Lennard-Jones parameters. The thermo-diffusion coefficient is calculated as:

$$D_i^T = \left[\sum_{j=1}^{N} \frac{M_i M_j}{M^2} k_{ij} D_{ij} \right]_{j \neq i} \tag{26}$$

where M is the mixture molecular weight and k_{ij} is the thermo-diffusion ratio.

4.2 Numerical Method

The governing equations are solved using commercial package CFD-ACE. An orthogonal, non-uniform staggered-grid system is used for solving the discretized equations with a control volume formulation in accordance with the SIMPLEC algorithm. The momentum equations are solved using the second-order upwind scheme while the central difference method is used for the energy and species equations. The above equations are solved along the mesh lines in the computational domain using an iterative ADI and TDMA techniques. Input of the molecular transport data is obtained from the CHEMKIN package [53] and then the code calculates the thermal conductivity and viscosity of the mixture using Wilke's formula. Thermal diffusion and buoyancy effects are included in this analysis but radiation heat loss is neglected. The GRI-Mech 3.0 chemical kinetic mechanisms (53 species, 279 elementary reactions) [54] are coupled to the CFD package. In order to calculate the OH*, OH*, and C_2* emission intensities, additional CH*, OH*, and C_2* kinetics (as shown in Table 3) in consideration of reaction rate, quenching rate, and spontaneous emission rate [50] are also included in the chemical mechanisms with GRI-Mech 3.0.

4.3 Boundary Conditions

The computational domain and the boundary conditions employed are shown in Fig. 7. Uniform flow (1 m/s) of premixed methane/air mixtures is specified at the inflow boundary of the computational domain, which includes flow computation in the tube, and the velocity at the exit of burner port (tube exit) has been carefully checked and found to be in fully developed parabolic profile. As seen in the figure, the burner is placed inside the computational domain, and hence the property located inside as well as outside the burner is calculated. This takes into account the back-diffusion of species into the tube and the heat transfer between the tube and flame. The wall temperature is kept constant at 300 K. Far field boundary conditions are imposed to the open boundaries as shown in the figure. Non-slip and non-catalytic reaction conditions are applied on the burner surface. Burner specifications (inner/outer diameter, conductivity etc.) and inlet velocity for the corresponding burner are set to meet the current experiments. Total number of meshes is 135 in the radial and 310 in axial direction for a physical domain of 30 mm × 250 mm. The inner diameter and wall thickness of the tube are d = 10 mm and 1.5 mm, respectively. The fuel tube exit plane is placed 50 mm downstream from the inflow boundary in the computational domain. Stretched meshes are applied in both directions; a minimum grid size of 0.1 mm is placed near the burner and an enlarged grid size is set forth toward the outer boundaries. The grid-independence study suggests that 0.1 mm grid spacing is sufficient for resolving the flame features. Convergence of solution is declared when the ratio of change of the dependent variables to the maximum variables in that iteration is within 1 × 10^{-4}.

CHAPTER V
RESULTS AND DISCUSSION

5.1 Characteristics of Cassegrain Mirror

In order to understand the capability of the Cassegrain optics for “point” measurements of optical emissions, the spatial resolution of the Cassegrain optics is measured using an inverse ray tracing method. A diode laser is used to shine the red-light from the back-end of the optical fiber and to form a red spot at the focal point of the Cassegrain mirror. A CCD camera is directly placed at the focal point and moved along the optical axis to measure the light intensity profile. The measured light intensity distribution is depicted in Fig. 8. Fig. 8a shows the light-collection rate distribution at the focal point. It can be seen that the distribution of light intensity is not in a perfectly circular shape. This could be due to slightly misalignment between the laser light and the optical fiber or due to non-uniformity of the CCD chip. However, the high-intensity region indicates that a circular focal point with approximately 40 μm in diameter is achieved for the Cassegrain optics. The light intensity, defined by setting the threshold value at e^{-2} times the peak value, along the optical axis and its 3-D distribution are shown in Figs. 8b and 8c, respectively. The effective probe volume determined from Fig. 8c is found to be 40 μm in diameter and 600 μm in length. The effective probe volume of the present Cassegrain optics is slightly better than that (100 μm in diameter and 800 μm in length) designed by Kojima et al. [50].

Prior to the chemiluminescence emission measurements using the spectroscopic unit with PMT array, the effect of the slit width of the eye-mask on the reduction of background flame emissions is examined. Fig. 9 shows that the measured OH* with the mask have narrower profiles, while that without the mask yields a broader profile due to a contribution from background flame emissions collected outside the effective probe volume. We also rotate the slit angles and found that the measured OH* has a narrower profiles when the slit centerline is parallel to the flame axis. This findings is in agreement with that observed by Kojima et al. [50]. After considering a trade-off relation between the slit width and the signal-to-noise ratio of the peak value, we found that the best performance of the eye-mask for the present study is a 5-mm-wide slit with the slit centerline arranged parallel to the flame axis (see Fig. 3).

5.2 Chemiluminescence Emission Spectra

Typical chemiluminescence emission spectra from the laminar premixed CH_4/air Bunsen flames operated at $\phi = 0.85$, 1.0, and 1.3 are shown in Fig. 10. These spectra are obtained by a double monochromator coupled with a LN-CCD camera (see Fig. 4). In order to obtain the spectrum for wavelength covered from 208 to 835 nm, a 150 grooves/mm grating (12.8 nm/mm) is used. It can be seen from Fig. 10 that for $\phi = 0.85$, the peak emissions of OH*(0, 0) at 307 nm, CH*(0, 0) at 430 nm, C_2*(1, 0) at 470 nm, and C_2*(0, 0) at 516 nm are visible in the spectrum. These emissions are due to following molecular transitions in the flame: OH*($A^2\Sigma^+ - X^2\Pi$), CH*($A^2\Delta - X^2\Pi$), and C_2*($d^3\Pi - a^3\Pi$) [55, 56]. Previous studies [57, 58] have confirmed that the primary source of flame CH* is from the reaction $C_2H + O \rightarrow CH^* + CO$, which might then provide a measure of the final steps in the $C_{(2)}$ reaction chain. The formation of OH* is from the reaction $CH + O_2 \rightarrow OH^* + CO$, which might provide a measure of the final steps in the CH_x reduction chain. The formation mechanism of C_2*, however, remains unclear. There are a couple of reactions proposed for the formation of C_2* such as $CH_2 + C \rightarrow C_2^* + H_2$, $CH + C \rightarrow C_2^* + H$, $CH + CH \rightarrow C_2^* + H_2$, or $O + C_3 \rightarrow C_2^* + CO$. The reaction mechanisms and rate constants of OH*, CH*, and C_2* have been recently investigated in low-pressure hydrocarbon flames [55, 56]. In addition to the peak emissions, there is also a broad underlying CO_2* continuum [29] that extends from 280 nm throughout the sampled spectral region. This broadband emission varies with equivalence ratio and is especially significant when the spectral bandwidth of the detection system is broad [41]. Therefore, to obtain a more accurate measurement of chemiluminescence intensities, background correction based on the side bands must be made. The polynomial fits of the side bands used for background corrections are also shown in the figure (red dashed curves). A linear or quadratic fit to the spectrum around the primary peak is employed, depending on the spectrum of side bands. The curve fit value at ~310 nm is subtracted from the intensity measured, to obtain a corrected OH* peak intensity, and likewise at ~430 nm for CH* and from ~450 to ~590 nm for C_2*. In addition, the emission intensity varies with spectral location when the image is taken. This is due to that the grating has higher quantum efficiency at wavelength around visible and lower quantum efficiency near UV. During data processing, the emission intensity is corrected to compensate the quantum efficiency effect.

When the equivalence ratio is increased to 1.0, the peak intensities of OH*(0, 0), CH*(0, 0), and C_2* Swan band all increase. The intensity of C_2* Swan band reaches to a maximum value at $\phi = 1.3$. Since the chemiluminescence intensity of OH*, CH*, and C_2* varies with flame equivalence ratio, the ratio of CH*/OH*, C_2*/OH*, and C_2*/CH* can be used to determine flame local equivalence ratio. Generally, the strongest intensity of OH*, CH*, and C_2* located at 306, 431.4, and 516.5 nm, respectively, is independently monitored when the spectroscopic unit coupled with PMT array is used for chemiluminescence measurements. It should be noted that the detector gate time must be long enough to measure sufficient chemiluminescence light, but short enough to reject stray light from background, if a LN-CCD camera is used. However, the detector gate time is not an issue if a photomultiplier tube (PMT) is used.

5.3 Chemiluminescence Emissions in Laminar Premixed Flames

In the present study, two sensor systems are developed; one is the spectroscopic unit coupled with the PMT array, and the other is the double monochromator coupled with a LN-CCD camera. The use of PMT array provides prompt data acquisition rate which is more suitable for turbulent premixed flame measurements. However, the PMT array gives no information on the broadband CO_2* emissions. The broadband CO_2* emissions could affect the quantitative measurements of OH*, CH*, and C_2* if they are not subtracted out from the measured total intensities. On the other hand, the use of a LN-CCD camera gives all the information including the OH*, CH*, and C_2* peak intensities as well as the broadband CO_2* emissions. But the data acquisition rate is very slow because each image requires about 1.5 s to store in the personal computer. In order to verify the applicability of the sensor system using the double monochromator coupled with a LN-CCD camera to turbulent flame measurement, we also perform some measurements in turbulent premixed flames.

5.3.1 Measurements Using PMT Array

Simultaneous measurements of OH*, CH*, and C_2* chemiluminescence emissions using PMT array are made in laminar premixed methane-air jet flames ($\phi = 0.85$-2.0) to examine the applicability of the developed sensor system. The radial distributions of normalized OH*, CH*, and C_2* intensities at $h = 3$ and 9 mm for $\phi = 0.85$, 1.0, and 1.3 flames are shown in Figs. 11-13, respectively. The measured maximum intensity of OH*, CH*, and C_2* in the flames studied is used to respectively normalize each of emission signals, so that direct comparison of chemiluminescence intensity for different flame conditions can be made. It is noted that the radial location of local maximum chemiluminescence intensity is an indication of flame front position. In addition, the OH*, CH*, and C_2* intensities of the hydrocarbon flames are functions of the relative heat release rate and their concentrations. Moreover, the profile of the OH* spectra has been correlated to the flame temperature and the CH* is an important indicator of the prompt NO formation [59].

Fig. 11 shows the radial distributions of OH*, CH*, and C_2* intensities at $h = 3$ and 9 mm for $\phi = 0.85$ flame. It can be seen that the peak OH* and CH* chemiluminescence signals occur at $r = 3.51$ mm and no C_2* signal is detected near the burner exit ($h = 3$ mm). At downstream location ($h = 9$ mm), the C_2* signal increases and three emission signals peak at $r = 2.25$ mm. The shift of peak intensity location from $r = 3.51$ to 2.25 mm indicates that the flame front position moves towards the center of the flame with increasing downstream location. The low C_2* emissions in lean flame conditions have also been observed by Kojima et al. [36]. Similar radial distributions of OH*, CH*, and C_2* intensities at $h = 3$ and

9 mm for ϕ = 1.0 and 1.3 flames are shown in Figs. 12 and 13. It is noted that the high level of intensities between the two peaks is due to flame emissions coming from outside the probe volume. This fact suggests that although the present sensor is designed for "point" measurement, the emissions outside the probe volume are not completely eliminated by the eye mask. Figs. 11-13 also indicate that the flame width is increased as the euqivalence ratio is increased from fuel-lean to fuel-rich conditions. For instance, the peak OH* intensity locates at r = 3.51 mm for the ϕ = 0.85 flame at h = 3 mm and it shifts to r = 4.14 mm for ϕ = 1.3 at the same height. The increase of the flame width in the richer flames indicates that it requires a broader region for the fuel to be consumed.

Comparisons of the measured maximum intensity for ϕ = 0.85-2.0 at h = 3 and 9 mm are shown in Fig. 14. Results indicate that at both heights the maximum OH*, CH*, and C_2* intensities occur approximately at ϕ = 1.0, 1.1, and 1.2-1.25 respectively. These findings are in good agreement with experimental results of Kojima et al. [36], but depart from those measured by Jeong et al. [60]. Kojima et al. found that the peak OH* intensity occurred at ϕ = 1.1, CH* at ϕ = 1.2, and C_2* at ϕ = 1.3. Whereas Jeong et al. measured the peak intensities of OH*, CH*, and C_2* at ϕ = 0.86, 0.91, and 1.06, respectively. The closer agreement between our results and the data of Kojima et al. could be due to that a similar Cassegrain light collection system was used for the measurements.

It has been suggested that the chemiluminescence intensity ratio of CH* to OH* or C_2* to CH* or OH* and the equivalence ratio in hydrocarbob flames have a nearly linear relationship [36, 40, 61]. These suggestions were based on results showing that the chemiluminescence intensity was very sensitive to the equivalence ratio. In addition, the possibilities that the effects of temperature, pressure, and the size of the flame on the emission intensity could be canceled to detect the equivalence ratio. Therefore, the correlation between the chemiluminescence intensity ratio and euqivalence ratio at the flame front is investigated.

Fig. 15 shows the results of C_2*/CH*, C_2*/OH*, and CH*/OH* against the equivalence ratio for the local flame front of the laminar premixed methane-air jet flames at h = 3 and 9 mm. In Fig. 15, the peak emission intensities of OH*, CH*, and C_2* shown in Fig. 14 are used to determine C_2*/CH*, C_2*/OH*, and CH*/OH*. It can be seen in Fig. 15b that near the burner exit (h = 3 mm) the fluctuational levels of C_2*/CH* and C_2*/CH* are higher than that of CH*/OH* due to low C_2* emissions are produced at this downstream location. At h = 9 mm (Fig. 15a), the scatter of the C_2*/CH*, C_2*/OH*, and CH*/OH* is greatly reduced because higher emission intensities of OH*, CH*, and C_2* are generated. Figure 15 shows that the correlation of C_2*/CH*, C_2*/OH*, and CH*/OH* to the equivalence ratio is nearly linear when the equivalence ratio is less than 1.35. The high degree of correlation suggests that the local flame stoichiometry at the flame front of premixed methane-air flames can be determined by the spatially resolved chemiluminescence measurements. However, it seems difficult to measure the equivalence ratio in methane-air flames for $\phi > 1.35$ by using this system because nonlinear relationship is observed within this range. These findings are in excellent agreement with those obtained by Kojima et al [36].

Figure 15 also indicates that the variation of C_2*/OH* curve is most sensitive to the equivalence ratio and C_2*/CH* is the next most sensitive. However, the use of C_2*/OH* and C_2*/CH* correlations for determining the local equivalence ratio becomes less reliable for lean flame conditions, because the C_2* emission intensity is very low at $\phi < 1.0$, as shown in Fig. 11. On the other hand, the correlation of CH*/OH* can be used for determining the equivalence ratio in lean premixed flame conditions, because the CH* and OH* emissions can be observed clearly, as shown in Fig. 11. These results suggest that the spatially resolved emission intensity ratio of CH*/OH* can be used to determine the local flame stoichiometry in the reaction zone of premixed hydrocarbon flames for a wider range of equivalence ratios.

5.3.2 Measurements Using LN-CCD Camera

In order to validate the sensor system that consists of a double monochromator with a LN-CCD camera, chemiluminescence emission measurements of OH*, CH*, and C_2* are also made in the similar laminar premixed methane-air flames (ϕ = 0.85-2.0). The radial distributions of normalized OH*, CH*, and C_2* intensities at h = 3 and 9 mm for ϕ = 0.85, 0.95, 1.0, 1.2, 1.35, and 1.5 flames are shown in Figs. 16-21, respectively. It can be seen that for ϕ = 0.85 flame the peak OH* and CH* chemiluminescence signals occur at r = 4.14 mm and very low C_2* signal is detected near the burner exit (h = 3 mm). At downstream location (h = 9 mm), the peak intensity location shifts from r = 4.41 to 3.06 mm that indicates the flame front position moving towards the center of the flame with increasing downstream location. Comparison of Figs. 16 and 11 indicates that the measured peak intensity locations are slightly different using both sensor systems. This could be due to that the scanning step (0.18 mm) used for Fig. 16 measurements are twice of that for Fig. 11.

Similar radial distributions of OH*, CH*, and C_2* intensities at h = 3 and 9 mm for ϕ = 1.0, 1.2, 1.35, and 1.5 flames are shown in Figs. 17-21. It is noted that the high level of intensities between the two peaks is due to flame emissions coming from outside the probe volume. Figs. 17-21 also indicate that the flame width is increased as the equivalence ratio is increased from fuel-lean to fuel-rich conditions. In general, the measurements of chemiluminescence intensity using the double monochromator with a LN-CCD camera give better signal-to-noise ratio than those measured by the PMT array because the interferences due to broadband CO_2* emissions can be subtracted out.

Comparisons of the measured maximum intensity for ϕ = 0.85-1.5 at h = 3 and 9 mm are shown in Fig. 22. Results indicate that at both heights the maximum OH*, CH*, and C_2* intensities occur approximately at ϕ = 0.95-1.05, 1.15-1.2, and 1.3 respectively. These findings are in good agreement with experimental results of Kojima et al. [36], but depart from those measured by Jeong et al. [60]. Kojima et al. found that the peak OH* intensity occurred at ϕ = 1.1, CH* at ϕ = 1.2, and C_2* at ϕ = 1.3. Whereas Jeong et al. measured the peak intensities of OH*, CH*, and C_2* at ϕ = 0.86, 0.91, and 1.06, respectively. The closer agreement between our results and the data of Kojima et al. could be, again, due to that a similar Cassegrain light collection system was used for the measurements. Comparison of Figs. 22 and 14 reveals that the uncertainty of ϕ in maximum intensity measuremeents is within ±0.05.

In order to obtain a relationship between the intensity ratio and equivalence ratio for turbulent flame measurements, the intensity ratio of C_2*/CH*, C_2*/OH*, and CH*/OH* against the equivalence ratio for the local flame front of the laminar premixed methane-air jet flames at h = 9 mm is shown in Fig. 23. The intensity ratios are calculated from the time-averaged integrated intensities that are corrected for broadband emission of CO_2* and detector quantum efficiency. It can be seen that the C_2*/CH*, C_2*/OH*, and CH*/OH* ratios increase linearly with increasing equivalence ratio over the range from ϕ = 0.85 to 1.3. The high degree of correlation suggests that the local flame stoichiometry at the flame front of premixed methane-air flames can be determined by the spatially resolved chemiluminescence measurements. However, it seems difficult to measure the equivalence ratio in methane-air flames for $\phi > 1.35$ by using this system because nonlinear relationship is observed within this range. These findings are in excellent agreement with those obtained by Kojima et al. [36]. The log curve fit equations of the dependence of C_2*/CH*, C_2*/OH*, and CH*/OH* on the equivalence ratio are also shown in Fig. 23. These curve fit equations will be used for equivalence ratio measurements in turbulent flames. For all calibration conditions and for a given value of equivalence ratio, the C_2*/CH*, C_2*/OH*, and CH*/OH* ratios are within ±10% of the value given by each curve fit equation, which leads to an uncertainty of approximately ±0.1 for determination of equivalence ratio for $0.85 \leq \phi \leq 1.3$. It should be noted that the uncertainty of our measurement system is approximately twice as large as those reported by Kojima et al. [36] and Hardalupas et al. [40], due to lower quantum efficiency of the LN-CCD detectors used in this study.

5.4 Numerical Simulation of Laminar Premixed Flames

Numerical simulations of the laminar premixed CH_4-air Bunsen flames at ϕ = 0.85, 1.0, and 1.2 are performed to investigate the flame structures. Comparisons of the computed temperature isopleths for three different equivalence ratios are shown in Fig.24. It can be seen that the potential core exists in these laminar flames and the high temperature appears in the inner region of the jet. And the high temperature region is broader for the $\phi = 1.2$ flame because it requires more space for the fuel to be consumed. Computed OH*, CH*, and C_2* mass fraction isopleths are shown in Figs. 25, 26, and 27, respectively. Comparisons of the computed OH*, CH*, and C_2* mass fraction isopleths reveal that the CH* emissions exist in a very narrow region around the potential core of the jet flame. While the OH* and C_2* emissions distribute in a broader region. It is noted that the double peaks of C_2* emission appeared at the flame tip for the $\phi = 1.2$ flame suggest that the calculation of this flame may not reach the steady state condition. This flame requires further investigations.

Comparisons of the measured and predicted radial profiles of OH*, CH*, and C_2* emissions for the $\phi = 0.85$, 1.0, and 1.2 flames at $h = 3$ mm are shown in Fig. 28. The measured emission intensities and the calculated mass fractions of OH*, CH*, and C_2* are normalized by their respective maximum values so that direct comparison between the measured and predicted emission intensities at different equivalence ratios can be made. It is noted that the purpose of this comparison is to examine the differences between the measured and predicted intensity profiles and the locations of peak intensity. The high level of emissions appeared in the region from $r = 0$ to 3 mm is due to flame emissions coming from outside the probe volume. Fig. 28 indicates that the calculated OH* and C_2* intensity profiles are much broader that the measured data. However, the measured and calculated peak intensity locations are within ± 1 mm.

5.5 Measurements of Turbulent Premixed Flames

In order to verify the applicability of developed sensor system for simultaneous measurements of equivalence ratio and temperature in turbulent flame, the sensor system is calibrated with the laminar premixed flames as described in Sec.5.3.2. The obtained correlation equations that relate intensity ratio of C_2*/CH*, C_2*/OH*, and CH*/OH* to the equivalence ratio as shown in Fig. 23 are used for equivalence ratio measurements in turbulent flame. For temperature measurement, the instrument constant C_3 appeared in Eq. (19) must be determined. Thermocouple temperature measurements are performed in laminar premixed flames at $h = 9$ mm and at the radial location where the maximum emission intensity occurs. Comparison of the measured and calculated adiabatic equilibrium temperature as a function of equivalence ratio is shown in Fig. 29. Fig. 29 shows that the measured flame temperatures are much lower than the adiabatic flame temperatures. The lower measured flame temperatures could be due to the effects of radiation heat loss and mixing of the ambient air with the burned gas. Nonetheless, the measured flame temperatures and the intensity ratios of C_2*(1, 0)/ C_2*(0, 0) are used to obtain the instrument constant C_3 from Eq. (19). An average value of 1.7759 is obtained for the ϕ = 1.0-1.5 flames. The ϕ = 0.85-0.95 flames are not considered for the determination of the instrument constant because the low emission intensity of C_2*(1, 0) band in these flames may result in large uncertainty in temperature measurements.

Simultaneous measurements of OH*, CH*, C_2*(1, 0), and C_2*(0, 0) chemiluminescence emissions are made in turbulent premixed methane-air jet flames (ϕ = 1.0 and 1.3) to examine the applicability of the developed sensor system for simultaneous measurements of equivalence ratio and temperature. The exit velocity and Reynolds number are 2.5 m/s and 3200 for both ϕ = 1.0 and 1.3 turbulent flames. The radial distributions of average OH*, CH*, and C_2*(0, 0) intensities at h = 10 mm for ϕ = 1.0 and 1.3 turbulent flames are shown in Figs. 30 and 31, respectively. Note that at each radial location a total of 50 spectra are measured. It can be seen that for ϕ = 1.0 flame the OH* intensity is much higher than the CH* and C_2*(0, 0) intensities. While for ϕ = 1.3 flame, the CH* and C_2*(0, 0) intensities are increased remarkably. By applying the equations obtained from the laminar premixed flames, the histograms of measured equivalence ratio in turbulent premixed stoichiometric CH_4-air flame at h = 10 mm and r = -9 mm are shown in Fig. 32. The measured average equivalence ratios from the emission intensity ratio of C_2*/CH*, C_2*/OH*, and CH*/OH* are ϕ = 0.984, 0.987, and 0.992, respectively. The rms of the local equivalence ratio is less than 0.015. Similar measurements of the local equivalence ratio in turbulent premixed rich CH_4-air flame at h = 10 mm and r = -9.18 mm are shown in Fig. 33. The measured average equivalence ratios from the emission intensity ratio of C_2*/CH*, C_2*/OH*, and CH*/OH* are ϕ = 1.29, 1.275, and 1.231, respectively. The rms of the local equivalence ratio is also less than 0.015. Comparison of Figs. 32 and 33 suggests that the emission intensity ratio of CH*/OH* provides better result for equivalence ratio measurement in fuel-lean to stoichiometric flames. While the intensity ratio of C_2*/CH* is more suitable for equivalence ratio measurement in fuel-rich flames.

Radial distributions of mean and rms equivalence ratio at h = 10 mm measured by the emission intensity ratio of C_2*/CH*, C_2*/OH*, and CH*/OH* are compared in Figs. 34 for ϕ = 1.0 turbulent premixed flames. The measured mean equivalence ratio indicates that the stoichiometry of the flame is relatively uniform in the inner flame region. The decrease of the equivalence ratio near the jet outer boundary is due to mixing with the ambient air. Note that the equivalence ratio measured by the emission intensity ratio of C_2*/CH* shows no decrease near the jet boundary. This is because weak intensity of C_2* is observed in this region. Fig. 35 shows the radial distributions of mean and rms equivalence ratio at h = 10 mm for ϕ = 1.3 turbulent premixed flames. The intensity ratio of C_2*/CH* estimates an equivalence ratio closer to a preset value of 1.3 than the intensity ratio of C_2*/OH* and CH*/OH*. This fact suggests that the intensity ratio of C_2*/CH* is more suitable for equivalence ratio measurement in turbulent rich flames.

The histograms of measured mean and rms temperatures in turbulent premixed stoichiometric and rich CH_4-air flames at h = 10 mm and r = -9 mm are shown in Fig. 36. The measured mean temperatures using the emission intensity ratio of C_2*(1, 0)/C_2*(0, 0) for ϕ = 1.0 and 1.3 are 1825 and 1682 K, respectively. And the rms of the local temperature is 79 and 13 K for ϕ = 1.0 and 1.3, respectively. Because the Reynolds number for both turbulent flames is about the same, the higher fluctuation of the measured temperature for ϕ = 1.0 flame could be due to the lower C_2* emissions in stoichiometric flame. Radial distributions of the measured mean and rms temperatures for ϕ = 1.0 and 1.3 turbulent flames at h = 10 mm are shown in Fig. 37. It can be seen that the mean temperatures of ϕ = 1.0 flame are, as expected, higher than those of ϕ = 1.3 flame. The higher fluctuation of the rms temperatures for ϕ = 1.0 flame could be, again, due to the lower C_2* emissions in stoichiometric flame.

CHAPTER VI
SUMMARY AND CONCLUSIONS

In the present study, a low cost, robust, non-laser based optical sensor system has been developed and applied to turbulent premixed CH_4-air flames for simultaneous measurements of equivalence ratio and temperature. The sensor system uses Cassegrain optics to eliminate the chromatic aberrations and to improve the spatial resolution for light collection. Two types of light detection units, one is the spectroscopic unit with the PMT array and the other is the spectrometer with the LN-CCD camera, are tested in the experiments to verify their applicability. The PMT array provides fast data acquisition rate for chemiluminescence emission measurements but gives no information on the broadband CO_2* emissions. On the other hand, the LN-CCD camera measures the entire spectral range of OH*, CH*, C_2*(1, 0), C_2*(0, 0), C_2*(0, 1) as well as the broadband CO_2* emissions but gives slow data acquisition rate (about 1.5 s per image frame). Although the LN-CCD camera gives slow data acquisition rate, the simultaneous measurements of C_2*(1, 0) and C_2*(0, 0) emissions provide a method for flame temperature measurement using the intensity ratio of C_2*(1, 0)/C_2*(0, 0). Both types of light detection units are applied to the laminar premixed flames to demonstrate the capability of the light detection units for chemiluminescence emission measurements. The measured radial distributions of OH*, CH*, and C_2*(0, 0) suggest that although the Cassegrain optics improves the spatial resolution, the light emissions outside the focal volume are also collected by the Cassegrain optics. The maximum intensity occurs at the radial position which indicates the location of flame front. The flame front position varies with the equivalence ratio. Comparisons of the measured maximum intensity for ϕ = 0.85-1.5 at h = 3 and 9 mm indicate that at both heights the maximum OH*, CH*, and C_2* intensities occur approximately at ϕ = 0.95-1.05, 1.15-1.2, and 1.3 respectively. These findings are in good agreement with experimental results of Kojima et al. [36], but depart from those measured by Jeong et al. [60]. The chemiluminescence intensity ratio of C_2*/CH*, C_2*/OH*, and CH*/OH* ratios increase linearly with increasing equivalence ratio over the range from ϕ = 0.85 to 1.3. The high degree of correlation suggests that the local flame stoichiometry at the flame front of premixed methane-air flames can be determined by the spatially resolved chemiluminescence measurements. However, it seems difficult to measure the equivalence ratio in methane-air flames for $\phi > 1.35$ by using this system because nonlinear relationship is observed within this range. The log curve fit equations of the dependence of C_2*/CH*, C_2*/OH*, and CH*/OH* on the equivalence ratio are used for equivalence ratio measurements in turbulent flames. For all calibration conditions and for a given value of equivalence ratio, the C_2*/CH*, C_2*/OH*, and CH*/OH* ratios are within ±10% of the value given by each curve fit equation, which leads to an uncertainty of approximately ±0.1 for determination of equivalence ratio for $0.85 \leq \phi \leq 1.3$. In addition, the maximum intensity ratios of C_2*(1, 0)/ C_2*(0, 0) measured in the laminar flames are used to obtain the instrument constant C_3 for turbulent flame temperature measurements. An average value of 1.7759 is obtained for the $\phi = 1.0\text{-}1.5$ flames. The $\phi = 0.85\text{-}0.95$ flames are not considered for the determination of the instrument constant because the low emission intensity of $C_2^*(1, 0)$ band in these flames may result in large uncertainty in temperature measurements.

Numerical simulations of the laminar premixed CH_4-air Bunsen flames at $\phi = 0.85$, 1.0, and 1.2 are performed to investigate the flame structures. Comparisons of the computed OH*, CH*, and C_2^* mass fraction isopleths reveal that the CH* emissions exist in a very narrow region around the potential core of the jet flame. While the OH* and C_2^* emissions distribute in a broader region. The double peaks of C_2^* emission appeared at the flame tip for the $\phi = 1.2$ flame are observed which suggest that the calculation of this flame may not reach the steady state condition and this flame requires further investigations. Comparisons of the measured and predicted radial profiles of OH*, CH*, and C_2^* emissions for the $\phi = 0.85$, 1.0, and 1.2 flames at $h = 3$ mm indicate that the calculated OH* and C_2^* intensity profiles are much broader that the measured data. However, the measured and calculated peak intensity locations are within ± 1 mm.

Simultaneous measurements of OH*, CH*, $C_2^*(1, 0)$, and $C_2^*(0, 0)$ chemiluminescence emissions are made in turbulent premixed methane-air jet flames ($\phi = 1.0$ and 1.3) to examine the applicability of the developed sensor system for simultaneous measurements of equivalence ratio and temperature. The obtained correlation equations that relate intensity ratio of C_2^*/CH^*, C_2^*/OH^*, and CH^*/OH^* to the equivalence ratio and the instrument constant are used to determine the equivalence ratio and temperature in turbulent flame. The measured histograms of equivalence ratio show that the average equivalence ratios from the intensity ratio of C_2^*/CH^*, C_2^*/OH^*, and CH^*/OH^* are $\phi = 0.984$, 0.987, and 0.992, respectively, in turbulent premixed stoichiometric CH_4-air flame at $h = 10$ mm and $r = -9$ mm. The rms of the local equivalence ratio is less than 0.015. The measured average equivalence ratios from the emission intensity ratio of C_2^*/CH^*, C_2^*/OH^*, and CH^*/OH^* are $\phi = 1.29$, 1.275, and 1.231, respectively, in turbulent premixed rich CH_4-air flame at $h = 10$ mm and $r = -9.18$ mm. The rms of the local equivalence ratio is also less than 0.015. Comparison of the measured mean equivalence ratios in both turbulent flames suggests that the emission intensity ratio of CH^*/OH^* provides better result for equivalence ratio measurement in fuel-lean to stoichiometric flames. While the intensity ratio of C_2^*/CH^* is more suitable for equivalence ratio measurement in fuel-rich flames. The histograms of measured mean and rms temperatures in turbulent premixed stoichiometric and rich CH_4-air flames at $h = 10$ mm and $r = -9$ mm show that the mean temperatures using the emission intensity ratio of $C_2^*(1, 0)/C_2^*(0, 0)$ for $\phi = 1.0$ and 1.3 are 1825 and 1682 K, respectively. And the rms of the local temperature is 79 and 13 K for $\phi = 1.0$ and 1.3, respectively. The higher fluctuation of the measured temperature for $\phi = 1.0$ flame could be due to the lower C_2* emissions in stoichiometric flame.

SELF EVALUATION

In the present study, a low cost, robust, non-laser based optical sensor has been developed for simultaneous measurements of local equivalence ratio and temperature in premixed hydrocarbon flames. The developed sensor is applied to the turbulent premixed CH_4-air flames and demonstrated its capability for simultaneous measurements of local equivalence ratio and temperature. Although the use of chemiluminescence intensity ratios of C_2*/CH*, C_2*/OH*, and CH*/OH* for local equivalence ratio measurements has been reported in the literature, simultaneous measurements of local equivalence ratio and temperature were not reported. Therefore, we will submit the results of the present study to SCI Journals for publication as soon as possible. In addition, we will continuously improve the non-laser based optical sensor system for future real-time active control in industrial burners and hazardous waste incinerators.

REFERENCES

1. Bureau of Energy, Ministry of Economic Affairs. http://www.moeaec.gov.tw/ecw.asp
2. 『蓄熱式燃燒技術開發』期末報告(2001-2003)，經濟部能源委員會。.
3. Johnson, C. E., Neumeier, Y., Lieuwen, T. and Zinn, B. T., Experimental Determination of the Stability Margin of a Combustor Using Exhaust Flow and Fuel Injection Rate Modulations. *Proc. Comb. Inst.* **28**: 757-763 (2000).
4. Neumeier, Y. and Zinn, B. T., Active Control of Combustion Instabilities with Real Time Observation of Unstable Combustor Modes. AIAA-96-0758 (1996).
5. Lefebvre, A. H., Gas Turbine Combustion (2nd ed), Taylor & Francis, Philadelphia, 1999.
6. Grosshandler, W., Hamins, A., McGrattan, K. and Rao Charagundla, S. and Presser, C., Suppression of a Non-Premixed Flame Behind a Step. *Proc. Comb. Inst.* **28**: 2957-2964 (2000).
7. Demayo, T. N., Miyasato, M. M. and Samuelsen, G. S., Hazardous Air Pollutant and Ozone Precursor Emissions From a Low-NOx Natural Gas-Fired Industrial Burner. *Proc. Comb. Inst.* **27**: 1283-1291 (1998)
8. Kuo, K. K., Principles of Combustion, John Wiley and Sons, Inc., NY, 1986.
9. Hayashi, S., Yamada, H., Shimodaira, K. and Machida, T., NOx Emissions From Non-Premixed, Direct Fuel Injection Methane Burners at High-Temperature and Elevated Pressure Conditions. *Proc. Comb. Inst.* **27**: 1833-1839 (1998).
10. Lieuwen, T. and Zinn, B. T., The Role of Equivalence Ratio Oscillations in Driving Combustion Instabilities in Low NOx Gas Turbines. *Proc. Comb. Inst.* **27**: 1809-1816 (1998).
11. Paschereit, C. O., Gutmark, E., Weisenstein, W., Control of Thermoacoustic Instabilities and Emissions an an Industrial-Type Gas-Turbine Combustor. *Proc. Comb. Inst.* **27**: 1817-1824 (2000).
12. Buschman, A., Dinkelacker, F., Schäfer,M. and Wolfrum, J., Measurement of the Instantaneous Detailed Flame Structure in Turbulent Premixed Combustion. *Proc. Combust. Inst.* **26**: 437-445 (1996).
13. Han, D., Mungal, M.G., Simultaneous Measurement of Velocity and CH Layer Distribution in Turbulent Non-Premixed Flames. *Proc. Combust. Inst.* **28**: 261-267 (2000).
14. Barlow, R.S., Fiechtner, G.J. and Chen, J.-Y., Oxygen Atom Concentrations and NO Production Rates in a Turbulent H2/N2 Jet Flame. *Proc. Combust Inst.* **26**: 2199-2205 (1996).
15. Nguyen, Quang-Viet. and Paul, P.H., The Time Evolution of a Vortex-Flame Interaction Observed via Planar Imaging of CH and OH. *Proc. Combust. Inst.* **26**: 357-364 (1996).

16. Cheng, T. S., Chao, Y.-C., Wu, D.-C., Yuan, T., Lu, C.-C., Cheng, C.-K. and Chang, J.-M., Effects of Fuel-Air Mixing on Flame Structures and NOx Formations in Swirling Methane Jet Flames. *Proc. Combust. Inst.* **27**: 1229-1237 (1998).
17. Al-Abdeli, Y. M. and Masri, A. R, Stability characteristics and flowfields of turbulent non-premixed swirling flames. *Combust. Theory Modelling* 7: 731-766 (2003).
18. Landenfeld, T., Kremer, A., Hassel, E. P., Janicka, J., Schäfer, T., Kazenwadel, Schulz, J. C. and Wolfrum, J., Laser-diagnostic and Numerical Study of Strongly Swirling Natural Gas Flames. *Proc. Combust. Inst.* **27**: 1023-1029 (1998).
19. Muniz, L. and Mungal, M. G., Instantaneous Flame-Stabilization Velocities in Lifted-Jet Flames. *Combust. Flame*, Vol. 112, pp. 16-31 (1997).
20. Kalt, P. A. M., Frack, J. H. and Bilger, R. W., Laser Imaging of Conditional Velocities in Premixed Propane-Air Flames by Simultaneous OH PLIF and PIV. *Proc. Combust. Inst.*, **27**: 751-758 (1998).
21. Sinibaldi, J. O., Driscoll, J. F., Mueller, C. J., Donbar, J. M. and Carter, C. D., Propagation Speeds and Stretch Rates Measured Along Wrinkled Flames to Assess The Theory of Flame Stretch. *Combust. Flame*, **133**: 323-334 (2003).
22. Kothnur, P. S., Tsurikov, M. S., Clemens, N. T., Donbar, J. M. and Carter, C. D., Planar Imaging of CH, OH, and Velocity in Turbulent Non-Premixed Jet Flames. *Proc. Combust. Inst.*, **29**: 1921-1927 (2002).
23. Watson, K. A., Lyons, K. M., Donbar, J. M. and Carter, C. D. Scalar and Velocity Field Measurements in Lifted Methane Diffusion Flames. *Combust. Flame,* **117**: 257-271 (1999).
24. Watson, K. A., Lyons, K. M., Donbar, J. M. and Carter, C. D. Observations on the Leading Edge in Lifted Flame Stabilization. *Combust. Flame,* **119**: 199-202 (1999).
25. Dibble, R. W., Masri, A. R., and Bilger, R. W., "The Spontaneous Raman Scattering Technique Applied to Nonpremixed Flames of Methane," *Combust. Flame,* Vol. 67, pp. 189, (1987).
26. Barlow, R. S. and Carter, C. D., "Raman/Rayleigh/LIF Measurements of Nitric Oxide Formation in Turbulent Hydrogen Jet Flames," *Comb. Flame,* Vol. 97, pp. 261-280, (1994).
27. Cheng, T. S., Wehrmeyer, 1. A., and Pitz, R. W., Simultaneous Temperature and Multispecies Measurement in a Lifted Hydrogen Diffusion Flame. *Comb. Flame,* Vol. 91, pp. 323-345, (1992).
28. Cheng, T. S., Wehrmeyer, J. A., Pitz, R. W., Jarrett, O. Jr., and Northam, G. B., Raman Measurement of Mixing and Finite-Rate Chemistry in a Supersonic Hydrogen/Air Diffusion Flame. *Combust. Flame,* Vol. 99, pp. 157-173 (1994).
29. Gaydon, A.G. and Wolfhard, H.G., *Flames: Their Structure, Radiation, and Temperature*. Fourth edition, Chapman and Hall, 1978.
30. Keller, J.O. and Saito, K., Measurements of the Combusting Flow in a Pulse

Combustor. *Combust. Sci. Tech.*, **53**: 137-163 (1987).

31. Lawn, C.J., Distributions of Instantaneous Heat Release by the Cross-Correlation of Chemiluminescent Emissions. *Combust. Flame*, Vol. 132, pp. 227-240 (2000).
32. Mehta, G.K., Ramachandra, M.K., and Strahle, W.C., Correlations between Light Emission, Acoustic Emission and Ion Density in Premixed Turbulent Flames. *Proc. Combust. Inst.*, **18**: 1051-1059 (1981).
33. Najm, H. N., Paul, P.H., Mueller, C. J., and Wyckoff, P. S., On adequacy of certain experimental observables as measurements of flame burning rate. *Combust. Flame*, Vol 113, pp 312-332 (1998).
34. Khanna,V. K., Vandsburger, U., Saunders W. R., and Baumann, W. T., Dynamic analysis of swirl stabilized turbulent gaseous flames. Paper GT-2002-30061, Proceedings of ASME Turbo Expo 2002, Amsterdam, Netherlands, Jun 3-6, 2002.
35. Ikeda, Y., Kojima, J., and Nakajima, T., Local Damkohler number measurement in turbulent methane/air premixed flames by local OH*, CH* and C2* chemiluminescence. Paper AIAA-2000-3395, 36th AIAA/ASME/SAE/ASEE Joint Propulsion Conference and Exhibit, Huntsville, Alabama, Jul 16-19, 2000.
36. Kojima, J., Ikeda, Y., and Nakajima, T., Spatially resolved measurement of OH*, CH* and C_2* chemiluminescence in the reaction zone of laminar methane/air premixed flames. *Proc. Combust. Inst.*, **28**: 1757-1764 (2000).
37. Ikeda, Y., Kojima, J., Nakajima, T., Akamatsu, F. and Katsuki, M., Measurement of the local flamefront structure of turbulent premixed flames by local chemiluminescence. *Proc. Combust. Inst.*, **28**: 343-350 (2000).
38. Ikeda, Y., Kojima, J., Hashimoto, H., and Nakajima, T., Detailed local spectra measurement in high-pressure premixed laminar flame. Paper AIAA-2002-0191, 40th Aerospace sciences meeting and exhibit, Reno, Nevada, Jan 14-17, 2002.
39. Tsushima, S., Saitoh, H., Akamatsu, F. and Katsuki, M., Observation of combustion characteristics of droplet clusters in a premixed-spray flame by simultaneous monitoring of planar spray images and local chemiluminescence. *Proc. Combust. Inst.*, **27**: 1967-1974 (1998).
40. Hardalupas, Y., Orain, M., Panoutsos, C. S., Taylor, A.M.K.P., Olofsson, J., Seyfried, H., Richter, M., Hult, J., Aldén, M., Hermann, F., and Klingmann, J., Chemiluminescence sensor for local equivalence ratio of reacting mixtures of fuel and air (FLAMESEEK). *Appl. Therm. Eng.* **24**: 1619-1632 (2004).
41. Muruganandam, T. M., Kim, B.-H., Morrell, M. R., Nori, V., Patel, M., Romig, B. W. and Seitzman, J. M., Optical equivalence ratio sensors for gas turbine combustors. *Proc. Combust. Inst.*, **30**, 1601-1609 (2004).
42. Kojima, J., Ikeda, Y., and Nakajima, T., Multi-point time-series observation of optical emissions for flame-front motion analysis. *Meas. Sci. Technol.* **14**, 1714–1724 (2003).
43. Thiruchengode, M., Nair, S., Prakash, S., Scarborough, D., Neumeier, Y. Lieuwen, T.,

Jagoda, J., Seitzman, J., and Zinn, B., An control system for LBO margin reduction in turbine engines. Paper AIAA-2003-1008, 41stAerospace sciences meeting and exhibit, Reno, Nevada, Jan 6-9, 2003.

44. Nandula, S. P., Brown, T. M., and Pitz, R. W., Measurements of scalar dissipation in the reaction zone of turbulent nonpremixed H_2-air flames. *Combust. Flame*, **99**, pp. 775-783 (1994).

45. Chen, Y.-C. and Mansour, M. S., Measurements of the detailed flame structure in turbulent H_2-Ar jet diffusion flames with line-Raman/Rayleigh/LIPF-OH technique. *Proc. Combust. Inst.*, **26**, 97-103 (1996).

46. Karpetis, A. N. and Barlow R. S., Measurements of flame orientation and scalar dissipation in turbulent partially premixed flames. *Proc. Combust. Inst.*, **30**, (In press).

47. Cheng,T. S., Yuan, T., Chao, Y.-C., Wu, D.-C. and Lu, C.-C., Premixed Methane-Air Flame Spectra Measurements Using UV Raman Scattering. *Combust. Sci. and Technol.*, Vol. 135, pp. 65-84 (1998).

48. Walsh, K. T., Long, M. B., Tanoff, M. A. and Smooke, M. D., Experimental and computational study of CH, CH*, and OH* in an axisymmetric laminar diffusion flames. *Proc. Combust. Inst.* **27**: 615-623 (1998).

49. Akamatsu, F., Wakabayashi, T., Tsushima, S., Katsuki, M., Mizutani, Y., Ikeda, Y., Kawahara, N., and Nakajima, T., Development of light-collecting probe with high spatial resolution applicable to randomly fluctuating combustion fields. *Meas. Sci. Technol.* **10**:1240–1246 (1999).

50. Kojima, J., Ikeda, Y. And Nakajima, T., Basic aspects of OH(A), CH(A), and C_2(d) chemiluminescence in the reaction zone of laminar methane-air premixed flames. *Combust. Flame*, **140**, 34-45, 2006.

51. Ishiguro, T., Tsuge, S., Furuhata, T., Kitagawa, K., Arai, N., Hasegawa, T., Tanak, R., and Gupta, A. K., Homogenization and stabilization during combustion of hydrocarbons with preheated air. *Proc. Combust. Inst.* **27**: 3205-3213 (1998).

52. Herzberg, G., “Molecular Spectra and Molecular Structure,” *Spectra of Diatomic Molecules,* Van Nostrand Reinhold, New York, 1950.

53. Kee, R. J. Rupley, F. Miller, J. Coltrin, M. Grcar, J. Meeks, E. Moffat, H. Lutz, A. Dixon-Lewis, G. Smooke, M. D. Warnatz, J. Evans, G. Larson, R. Mitchell, R. Petzold, L. Reynolds, L. Caracotsios, M. Stewart, W. and Glarborg, P. *User Manual, The CHEMKIN Collection Release 3.5,* Reaction Design, Inc., San Diego, CA, 1999.

54. Bowman, C. T., Hanson, R. K., Davidson, D. F., Gardiner Jr., W. C., Lissianski, V., Smith, G. P., Golden, D. M., Frenklach, M., Wang, H., and Goldenberg, M., *GRI-Mech Version 3.0,* Gas Research Institute, Chicago, http://www.gri.org, 2000.

55. Smith G. P., Luque, J., Park, C., Jeffeies, J. B., Crosley, D. R., Low pressure flame determinations of rate constants for OH(A) and CH(A) chemiluminescence. *Combust. Flame*, **131**, pp. 59-69 (2002).

56. Smith G. P., Park, C., Schneiderman, J., Luque, J., C_2 Swan band laser-induced fluorescence and chemiluminescence in low-pressure hydrocarbon flames. *Combust. Flame*, **141**, pp. 66-77 (2005).
57. Devriendt, K. and Peeters, J., Direct Identification of the $C_2H(X^2\Sigma^+) + O(^3P) \rightarrow CH(A^2\Delta) + CO$ Reaction as the Source of the $CH(A^2\Delta \rightarrow X^2\Pi)$ Chemiluminescence in C_2H_2/O/H Atomic Flames. *J. Phys. Chem. A 101*(14) pp 2546 – 2551 (1997).
58. Devriendt; K., Van Look, H., Ceursters, B. and Peeters, J., Kinetics of formation of chemiluminescent $CH(A^2\Delta)$ by the elementary reactions of $C_2H(X^2\Sigma^+)$ with $O(^3P)$ and $O_2(X^3\Sigma^-_g)$: a pulse laser photolysis study. Chem. Phys. Lett., 261, 450-456 (1996).
59. Lee, C. L., Oh, C. B. and Kim, J. H., "Numerical and experimental investigations of the NO_x emission characteristics of CH_4-air co-flow jet flames", Fuel, 83, 2323-2334, 2004.
60. Jeong, Y. K., Jeon, C. H. and Chang, Y. J., "Evaluation of the equivalence ratio of the reacting mixture using intensity ratio of chemiluminescence in laminar partially premixed CH_4-air flames", *Experimental Thermal and Fluid Science.* **30**: 663-673, 2006.
61. Chou, T. and Patterson, D. J., "In-cylinder measurement of mixture maldistribution in a L-head engine", *Combustion and Flame.* **101**(1-2): 45-57, 1995.
62.

Table 1. Operating conditions for laminar premixed CH_4-air Bunsen flames.

ϕ	CH_4 (l/min)	Air (l/min)
0.80	0.37	4.35
0.85	0.39	4.33
0.90	0.41	4.31
0.95	0.43	4.29
1.00	0.45	4.27
1.05	0.47	4.24
1.10	0.49	4.22
1.15	0.51	4.21
1.20	0.53	4.19
1.25	0.55	4.17
1.30	0.57	4.15
1.35	0.59	4.13
1.40	0.60	4.11
1.45	0.62	4.09
1.50	0.64	4.07

Table 2. Physical properties of the C_2* vibrational bands [51].

	λ (nm)	υ′, υ″	$E_{\upsilon'}$ (erg)	$A_{rel,\ \upsilon',\ \upsilon''}$
1	468.48	4, 3	7.67×10^{-13}	0.358
2	469.76	3, 2	6.02×10^{-13}	0.477
3	471.52	2, 1	4.34×10^{-13}	0.318
4	473.71	1, 0	2.63×10^{-13}	0.637
5	509.77	2, 2	4.34×10^{-13}	1.000
6	512.93	1, 1	2.63×10^{-13}	1.000
7	516.52	0, 0	0.88×10^{-13}	1.000

Table 3. Reaction mechanism for the excited state species OH(A), CH(A), and C_2(d) [50].

$$k = AT^n exp(-E_a / RT)$$

Reaction	A (cm^3/mol/s)	n	E_a (cal/mol)
$C_2H + O = CH^* + CO$	1.08E+13	0	0
$C_2H + O_2 = CH^* + CO_2$	2.17E+10	0	0
$CH^* = CH$	1.85E+06	0	0
$CH^* + N_2 = CH + N_2$	3.03E+02	3.4	-381
$CH^* + O_2 = CH + O_2$	2.48E+06	2.14	-1720
$CH^* + H_2O = CH + H_2O$	5.30E+13	0	0
$CH^* + H_2 = CH + H_2$	1.47E+14	0	1361
$CH^* + CO_2 = CH + CO_2$	2.40E-01	4.3	-1694
$CH^* + CO = CH + CO$	2.44E+12	0.5	0
$CH^* + CH_4 = CH + CH_4$	1.73E+13	0	167
$CH + O_2 = OH^* + CO$	3.25E+13	0	0
$OH^* = OH$	1.45E+06	0	0
$OH^* + N_2 = OH + N_2$	1.08E+11	0.5	-1238
$OH^* + O_2 = OH + O_2$	2.10E+12	0.5	-482
$OH^* + H_2O = OH + H_2O$	5.92E+12	0.5	-861
$OH^* + H_2 = OH + H_2$	2.95E+12	0.5	-444
$OH^* + CO_2 = OH + CO_2$	2.75E+12	0.5	-968
$OH^* + CO = OH + CO$	3.23E+12	0.5	-787
$OH^* + CH_4 = OH + CH_4$	3.36E+12	0.5	-635
$CH_2 + C = C_2^* + H_2$	7.50E+13	0	0
$C_2^* = C_2$	8.33E+03	0	0

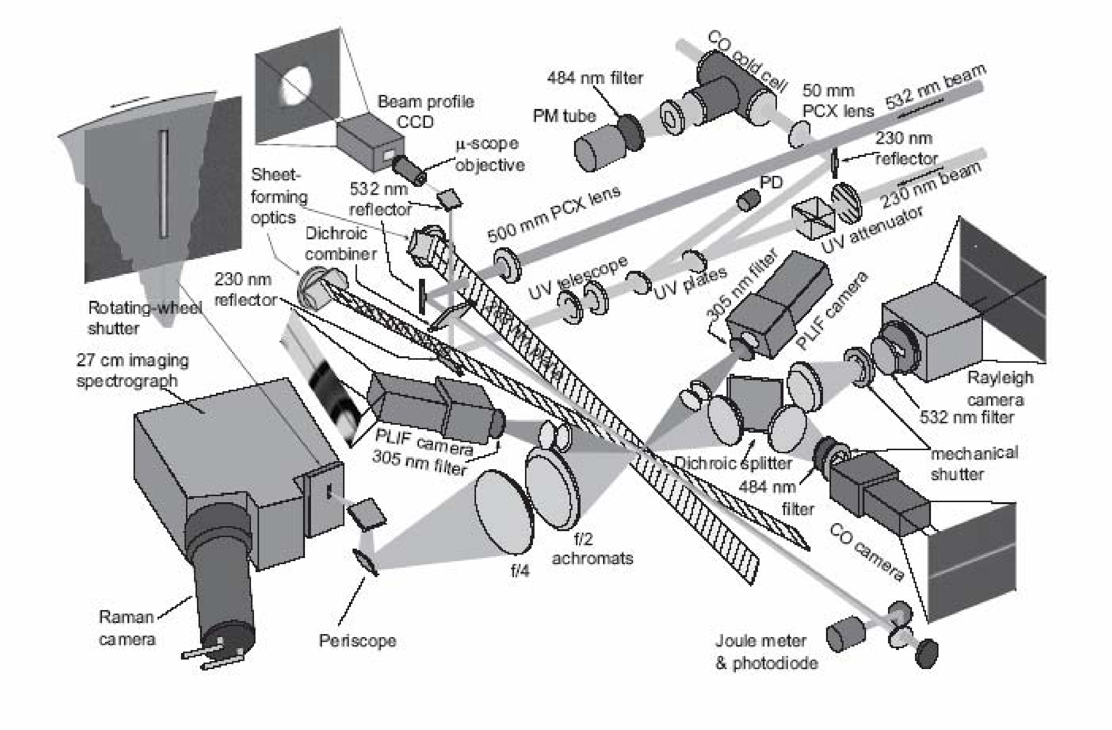

Fig. 1. Schematic diagram of the Raman/Rayleigh/CO LIF line imaging and crossed PLIF imaging experiment [44].

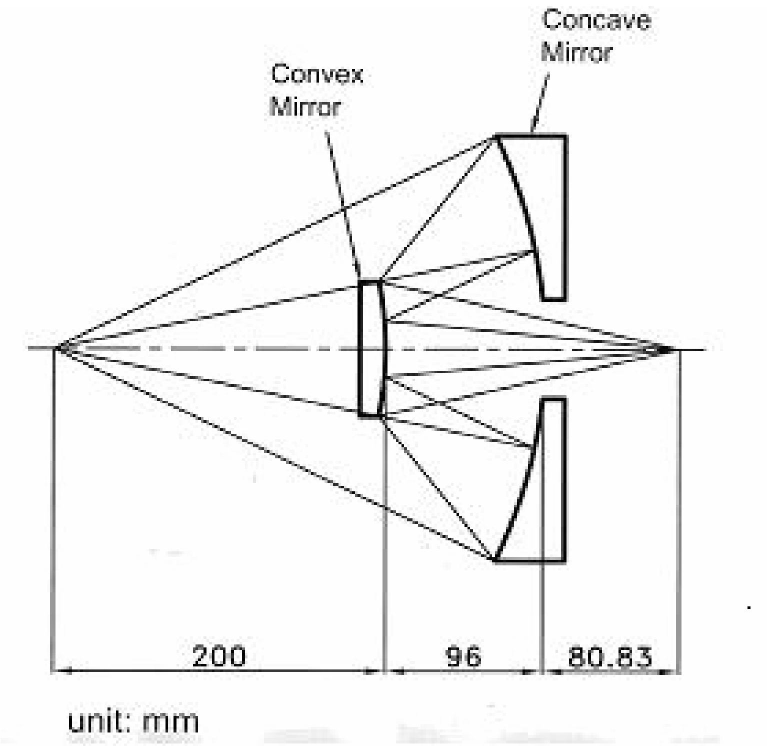

Fig. 2. Schematic diagram of Cassegrain optics.

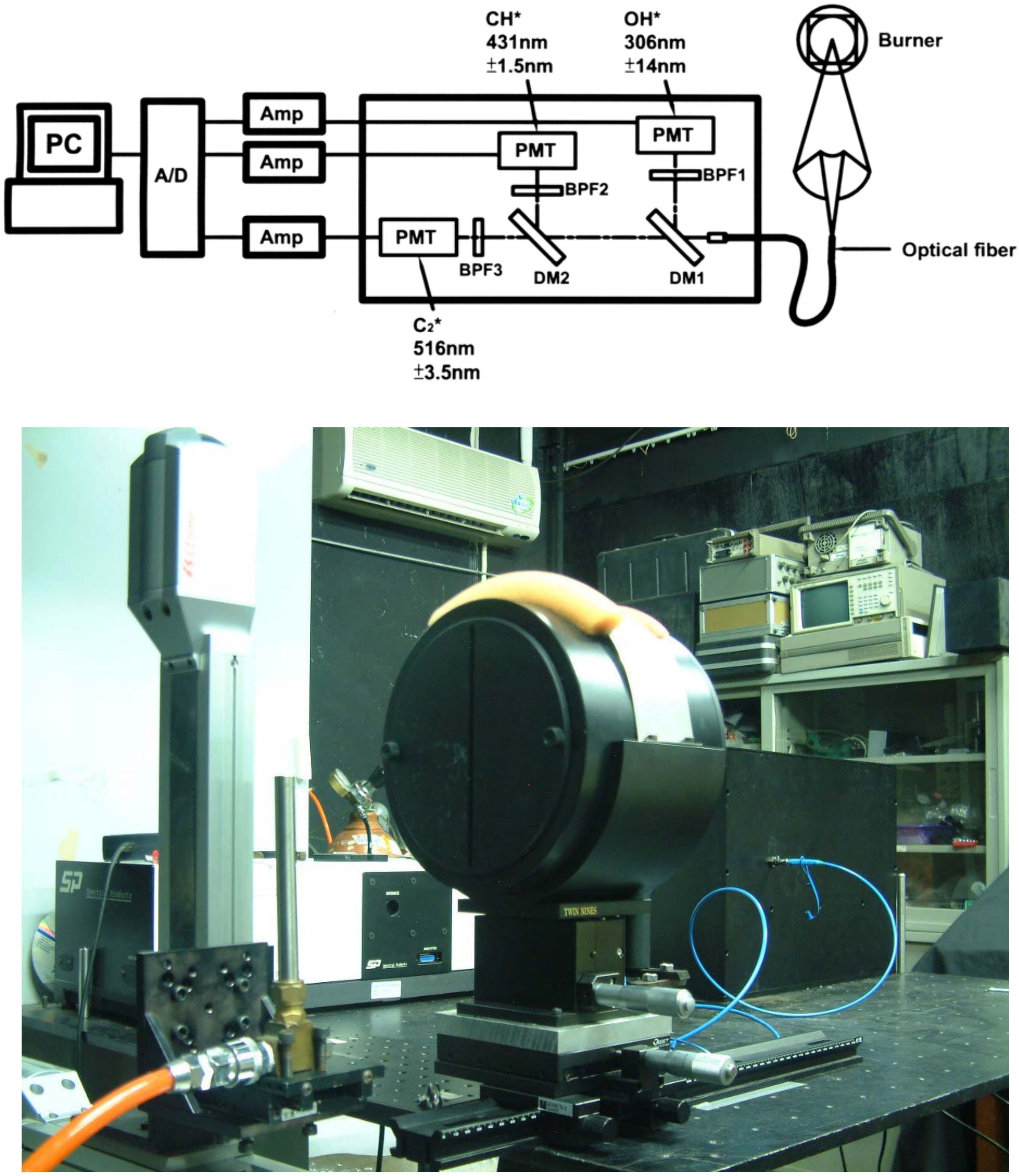

Fig. 3. Schematic diagram and photograph of the measurement system using the PMTs.

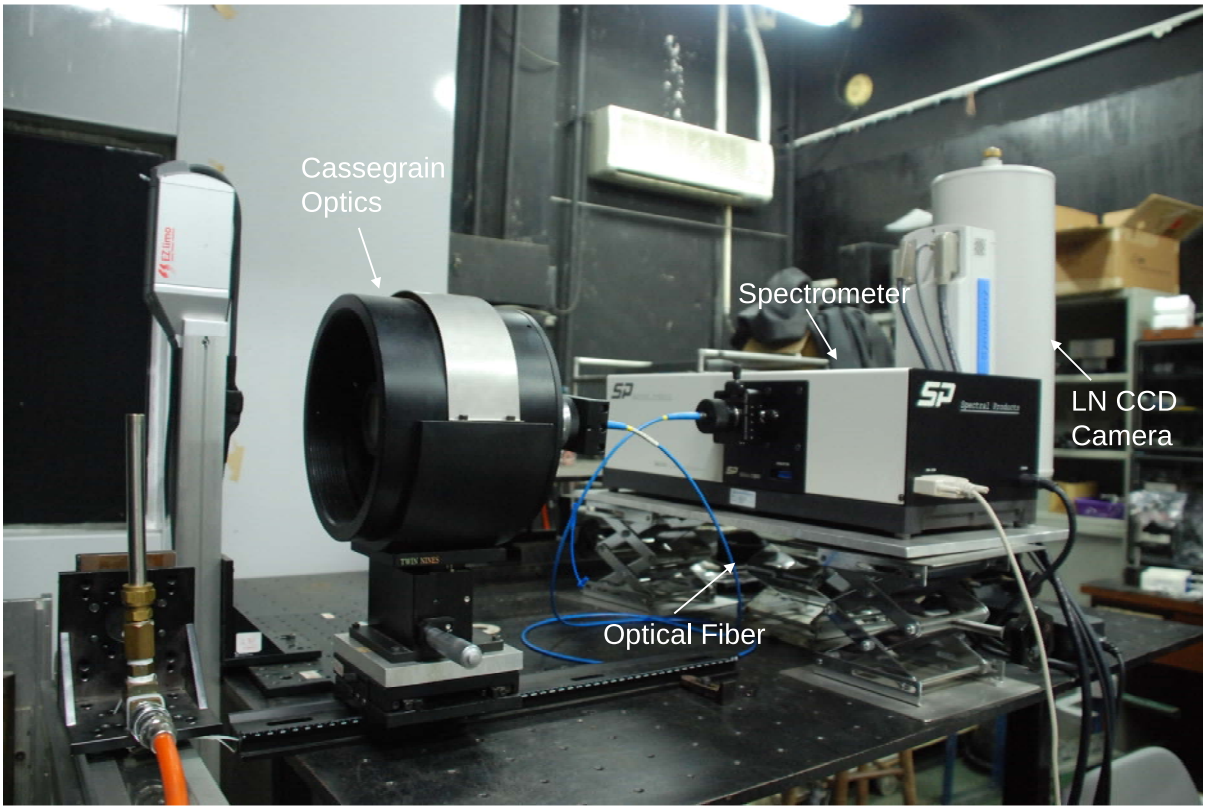

Fig. 4. Photograph of measurement system using a spectrometer coupled with a LN-CCD camera.

(a) Laminar (b) Turbulent

Fig. 5. Photograph of laminar (a) and turbulent (b) premixed CH_4/air flames at $\phi = 1.0$.

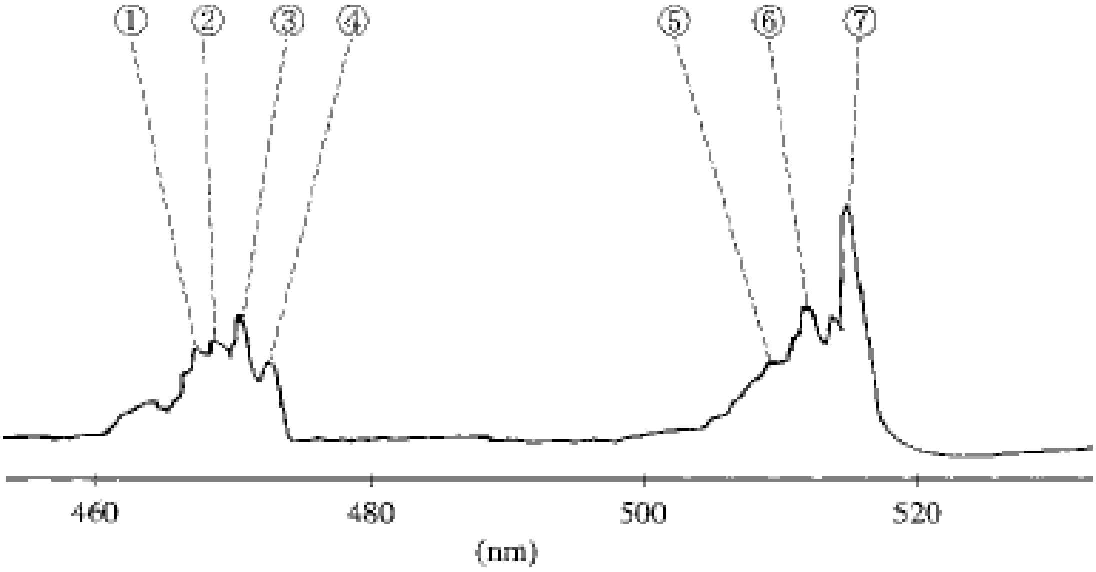

Fig. 6. Typical emission spectra of the two C_2^* bands between 460 and 520 nm for CH_4 flame under conditions of T_{N2+O2} = 20°C [51]. The numbers in the figure correspond to those given in Table 2.

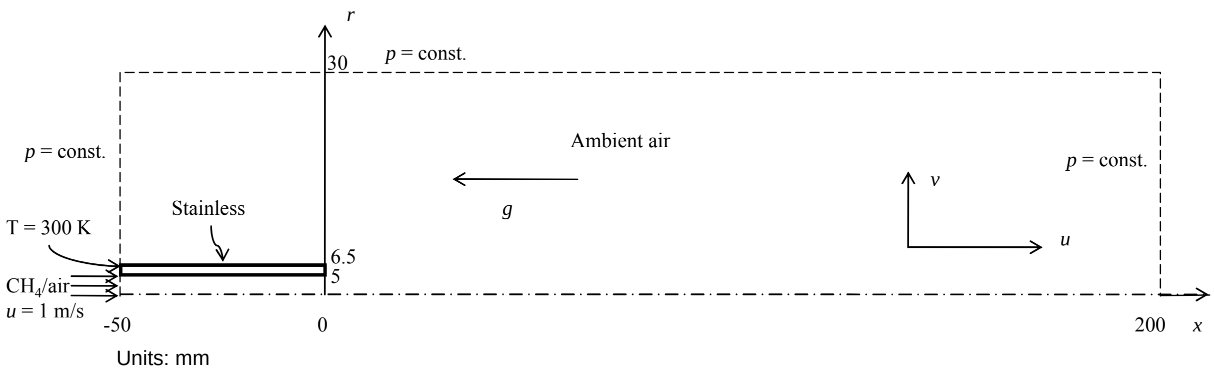

Fig. 7. Computational domain with boundary conditions.

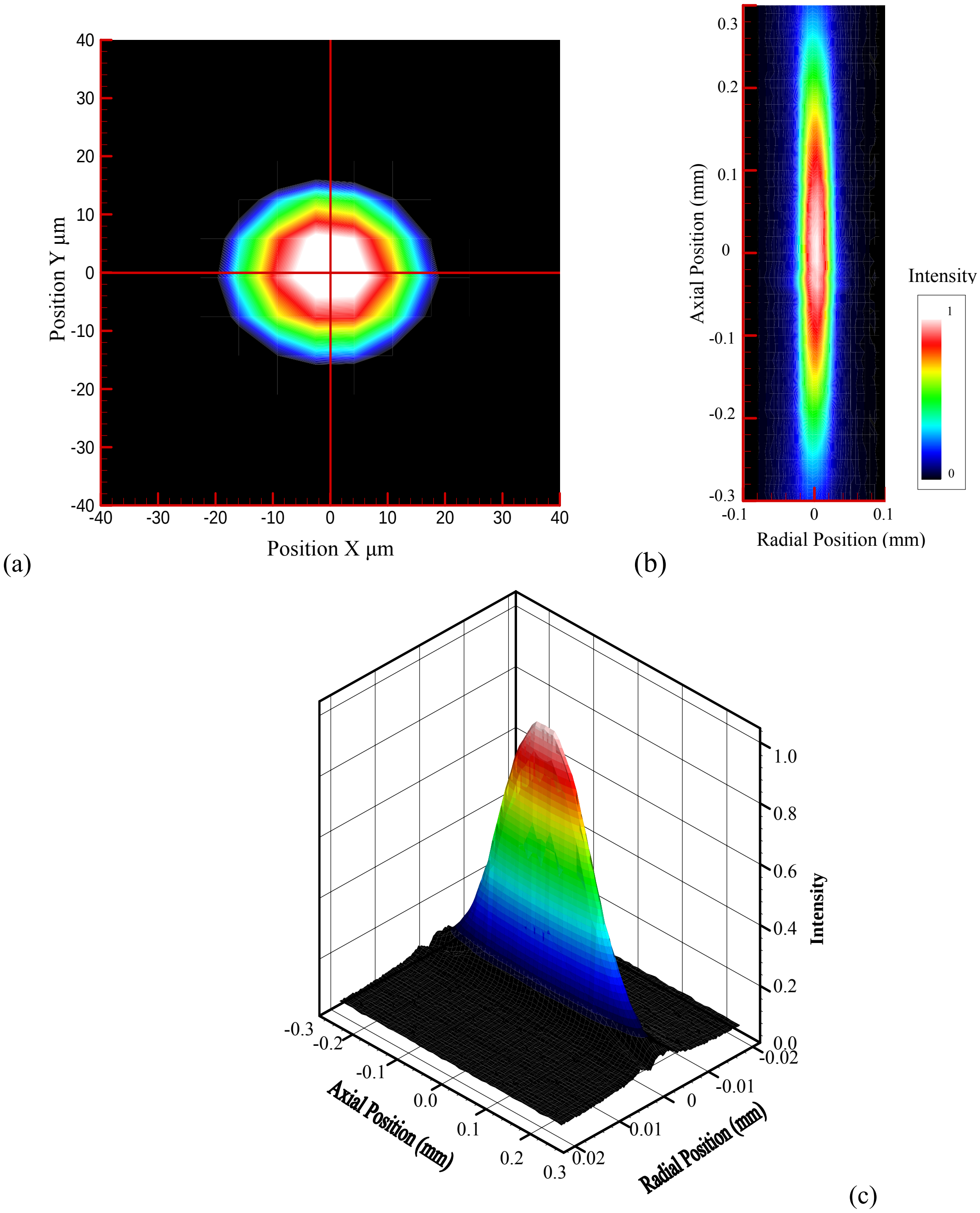

Fig. 8. The light-collection-rate distribution around the probe volume. (a) at the focal point, (b) 2-D distribution, and (c) 3-D profile.

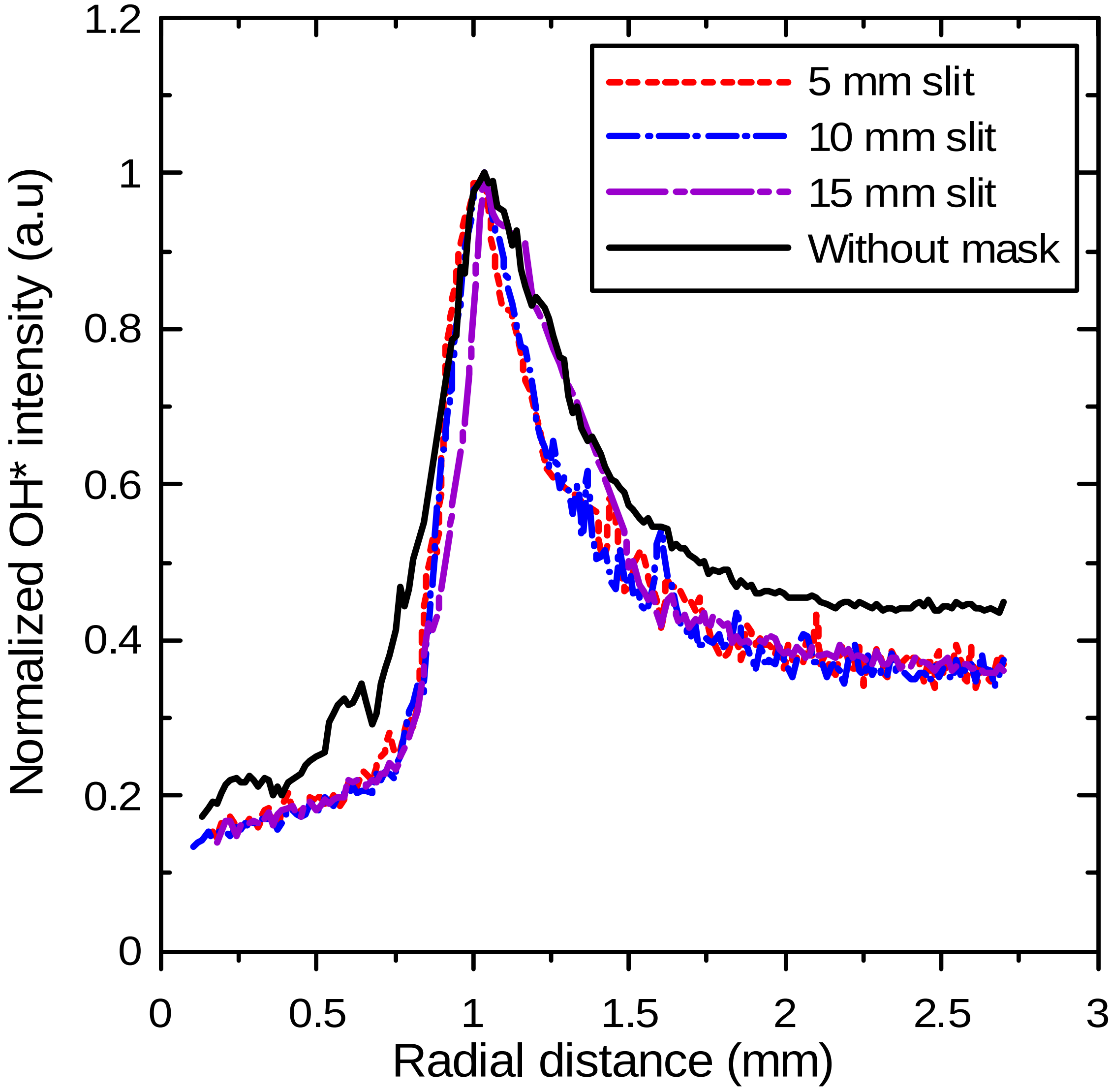

Fig. 9. Effect of the different slit widths of the eye mask on the OH* chemiluminescence intensity profiles (premixed CH_4-air jet flame, $\phi = 1.35$).

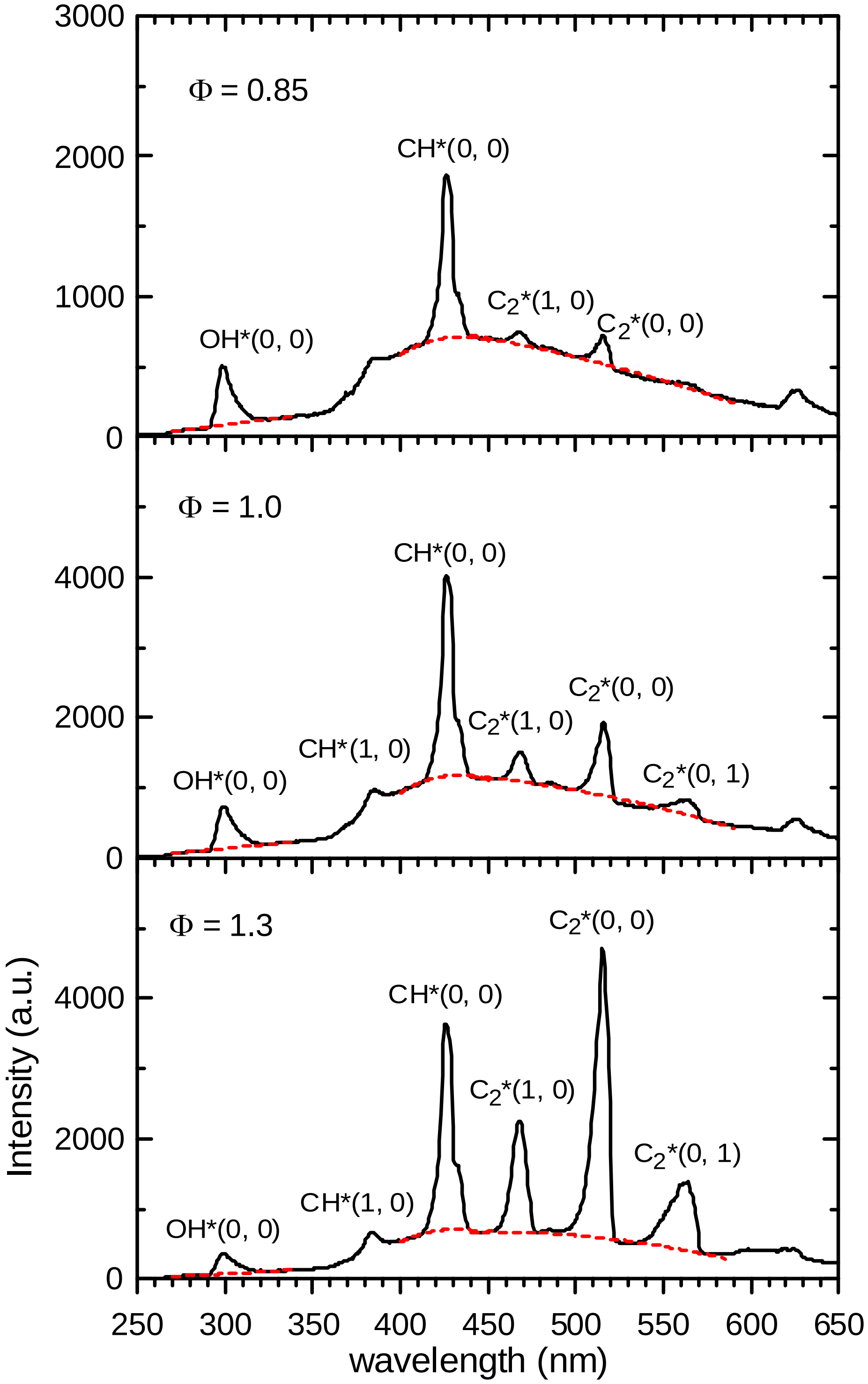

Fig. 10. Flame emission spectra measured from laminar premixed methane-air flames at ϕ = 0.85, 1.0, and 1.3.

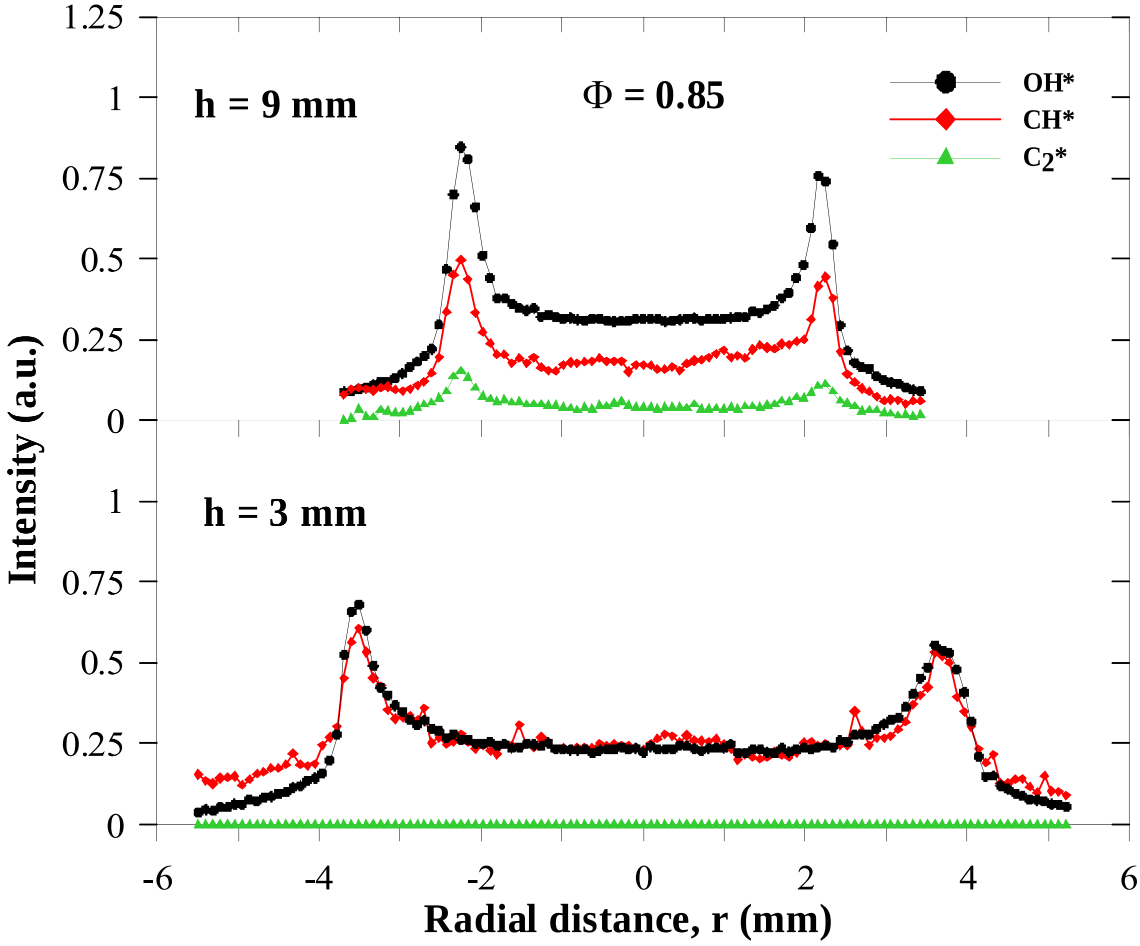

Fig. 11. Radial distribution of the OH*, CH*, and C_2* chemiluminescence intensities at *h* = 3 and 9 mm for $\phi = 0.85$ flame.

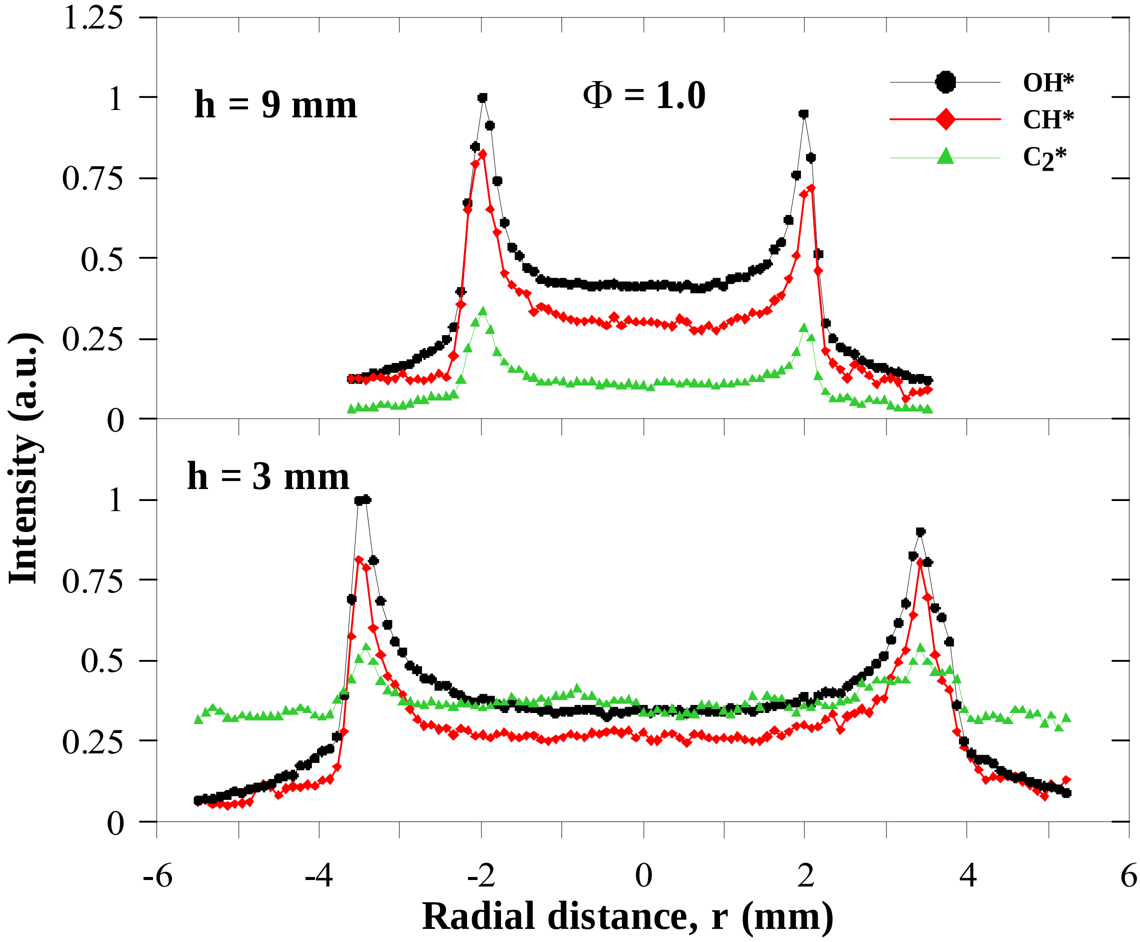

Fig. 12. Radial distribution of the OH*, CH*, and C_2* chemiluminescence intensities at *h* = 3 and 9 mm for ϕ = 1.0 flame.

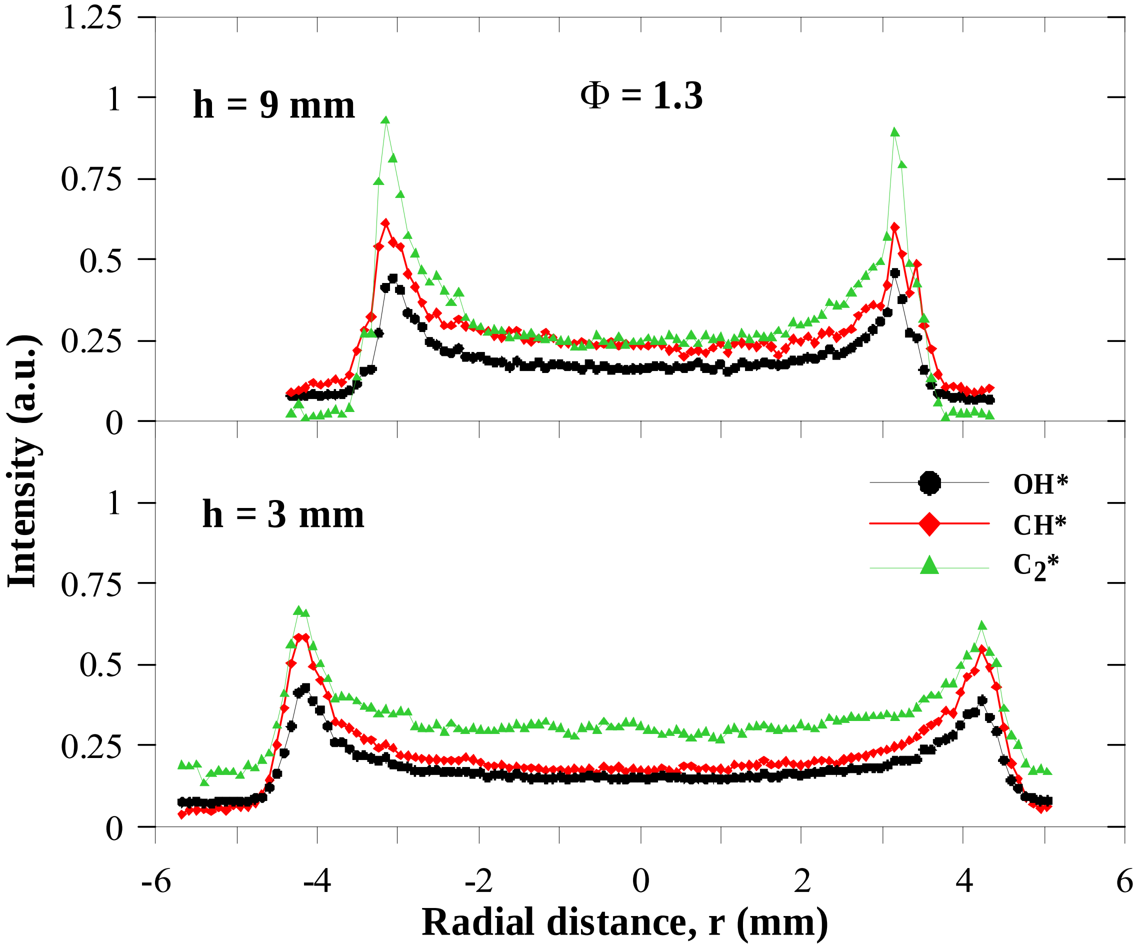

Fig. 13. Radial distribution of the OH*, CH*, and C_2* chemiluminescence intensities at *h* = 3 and 9 mm for ϕ = 1.3 flame.

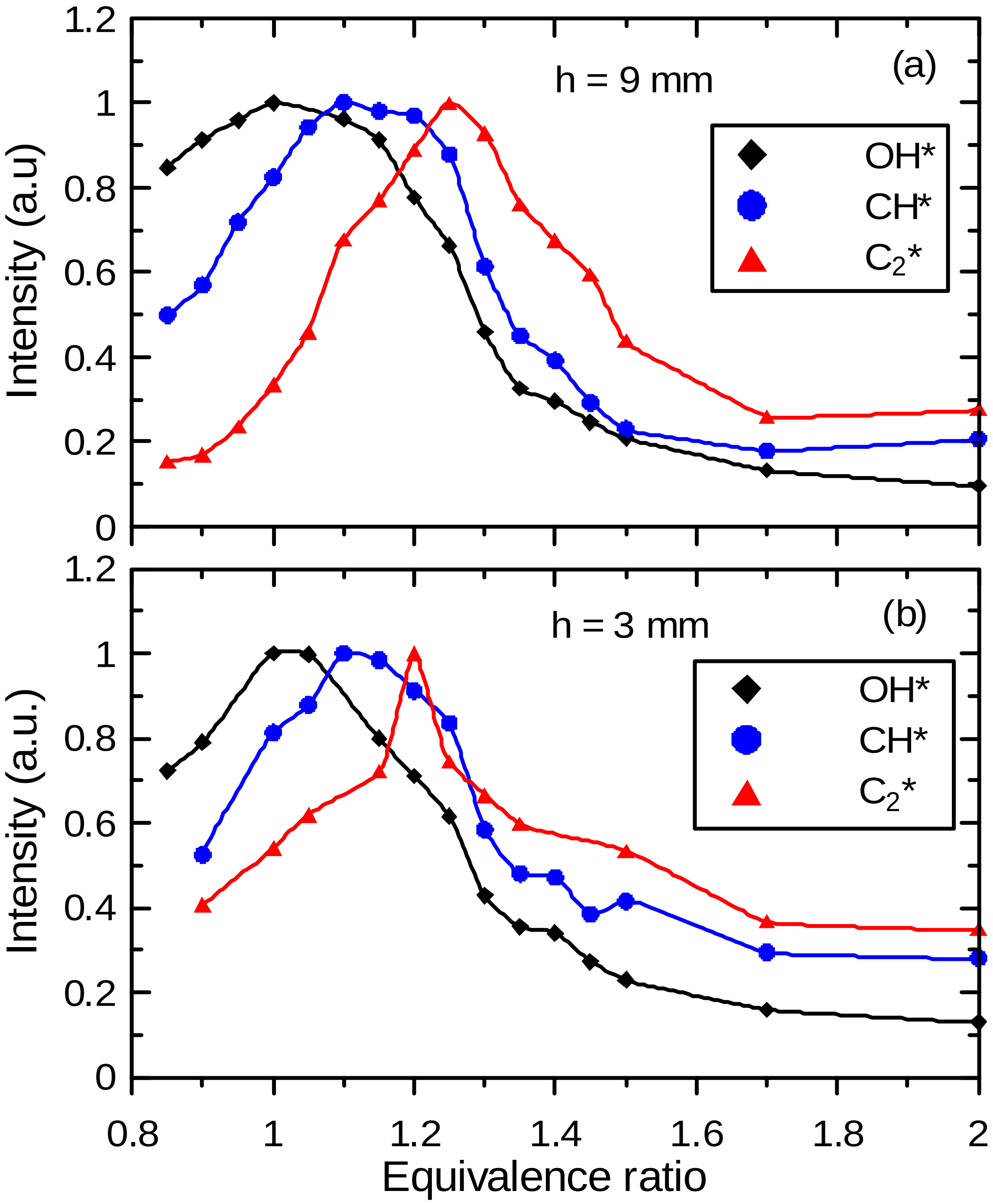

Fig. 14. Variations of the maximum chemiluminescence intensities with the equivalence ratio at *h* = 3 and 9 mm.

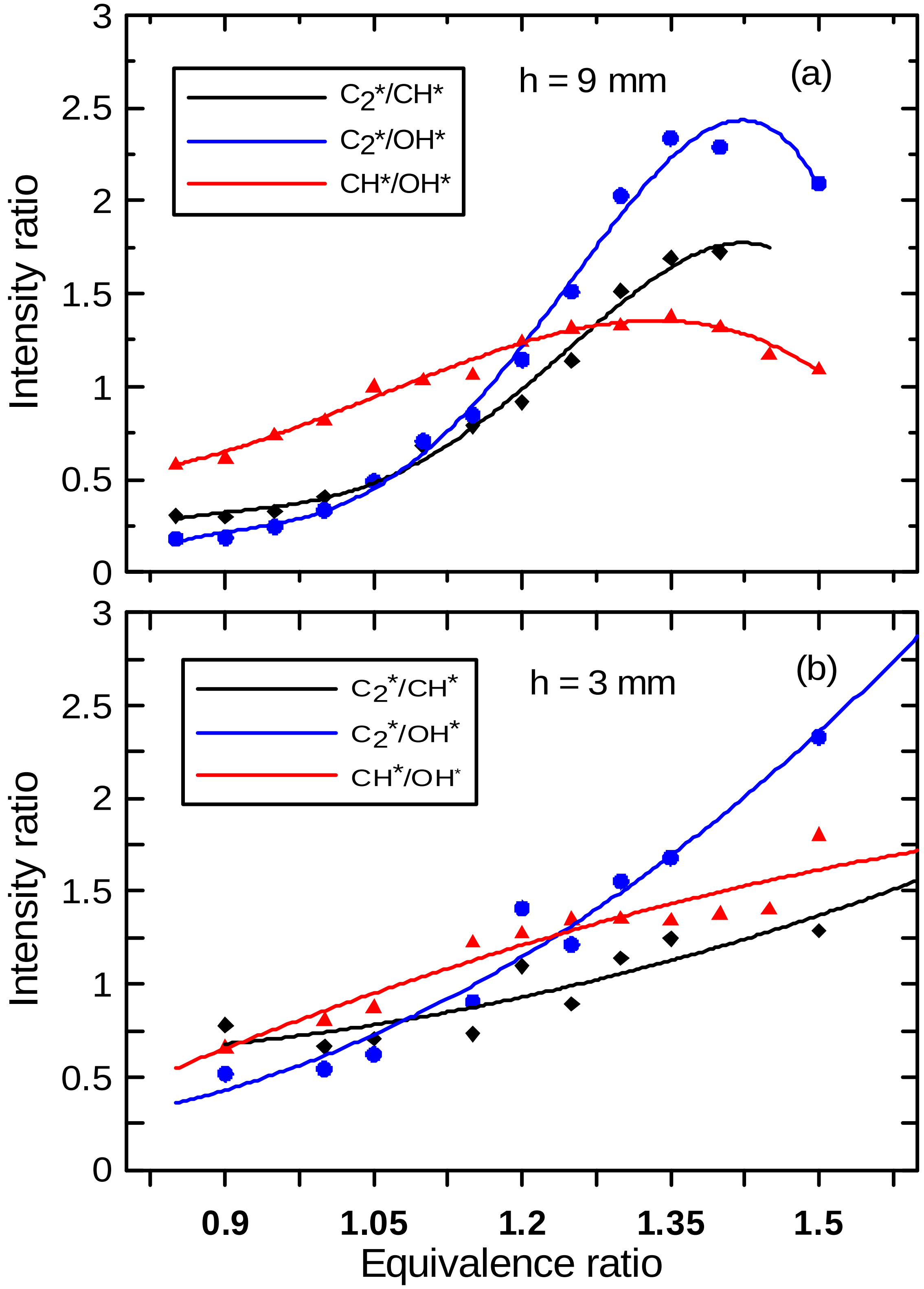

Fig. 15. Correlation of the intensity ratios of C2*/CH*, C2*/OH* and CH*/OH* to the equivalence ratios at *h* = 3 and 9 mm.

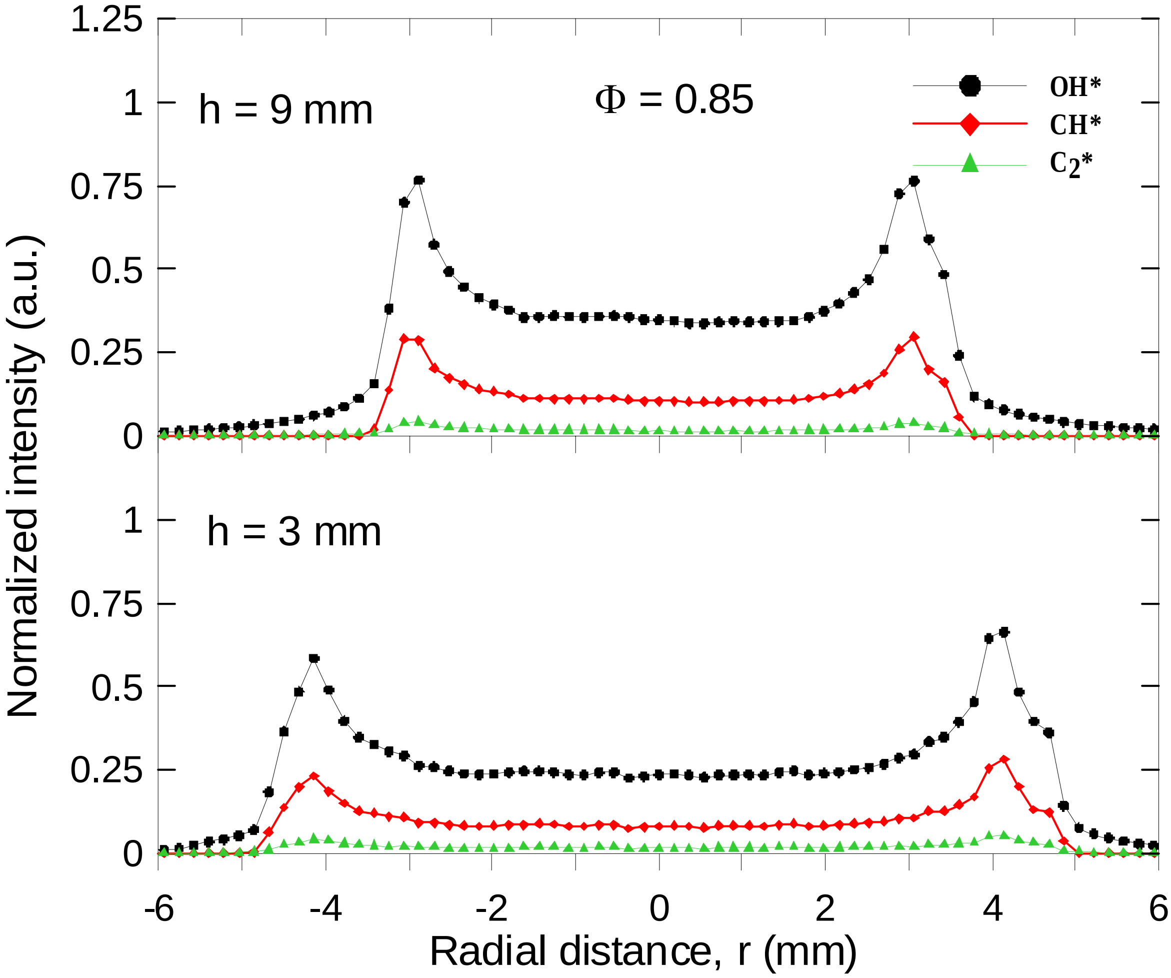

Fig. 16. Radial distribution of the OH*, CH*, and C_2* chemiluminescence intensities at *h* = 3 and 9 mm for $\phi = 0.85$ flame.

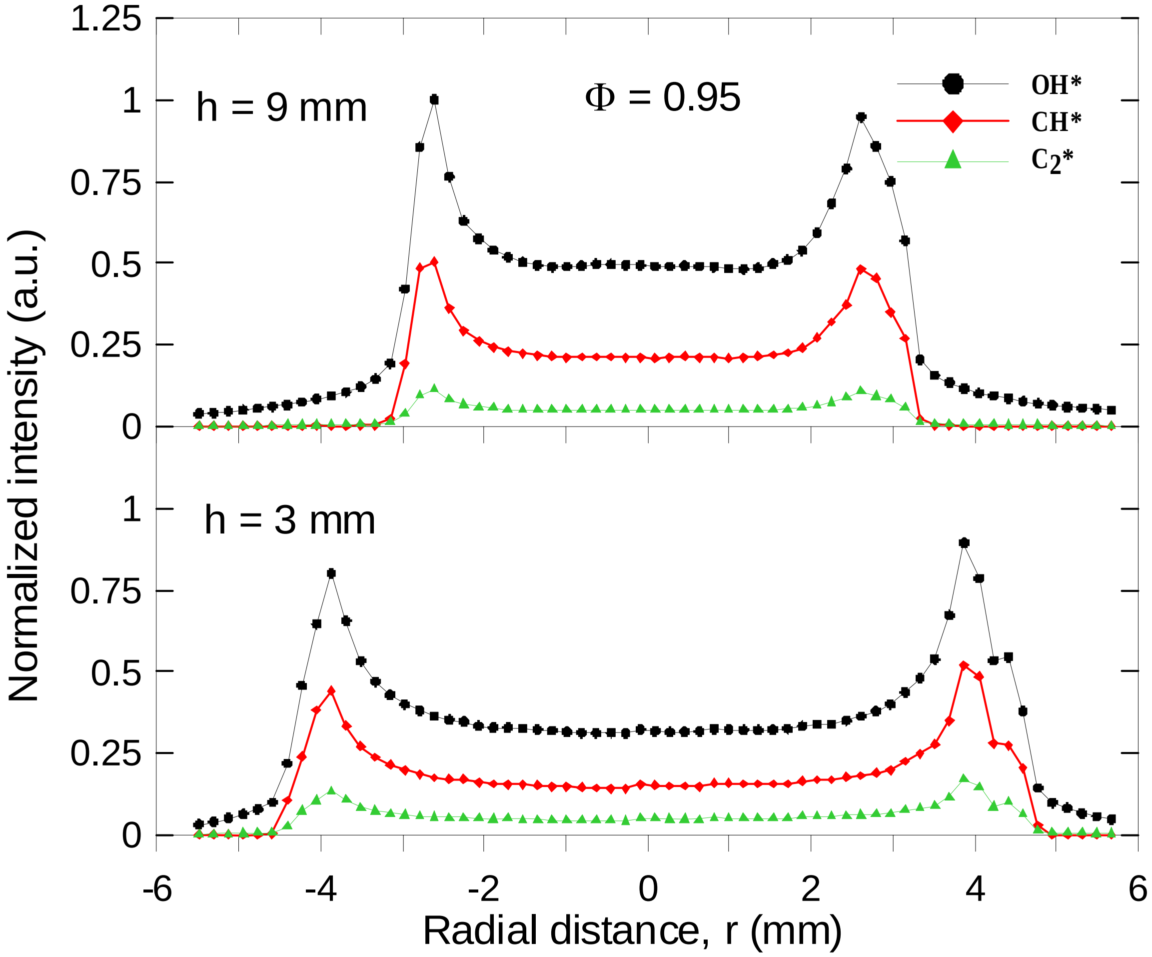

Fig. 17. Radial distribution of the OH*, CH*, and C_2* chemiluminescence intensities at *h* = 3 and 9 mm for ϕ = 0.95 flame.

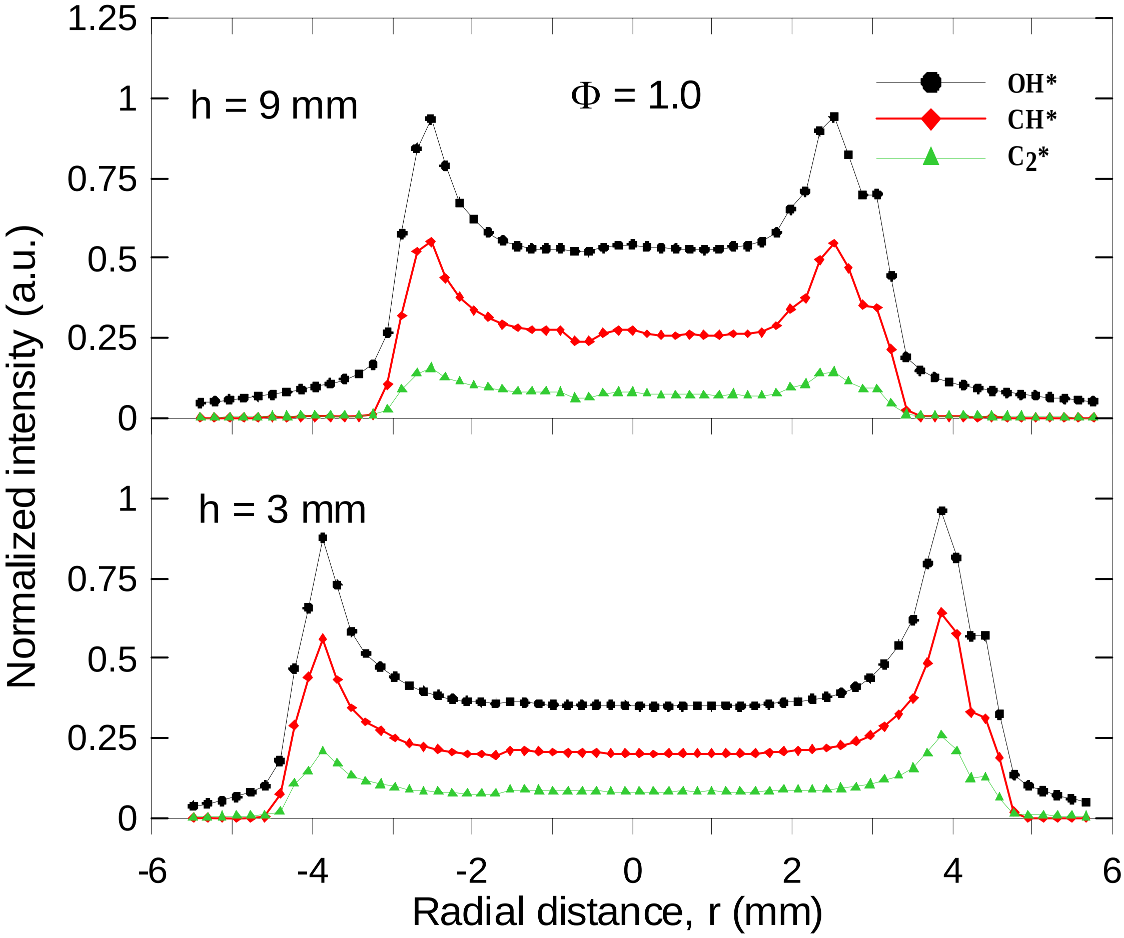

Fig. 18. Radial distribution of the OH*, CH*, and C_2* chemiluminescence intensities at *h* = 3 and 9 mm for $\phi = 1.0$ flame.

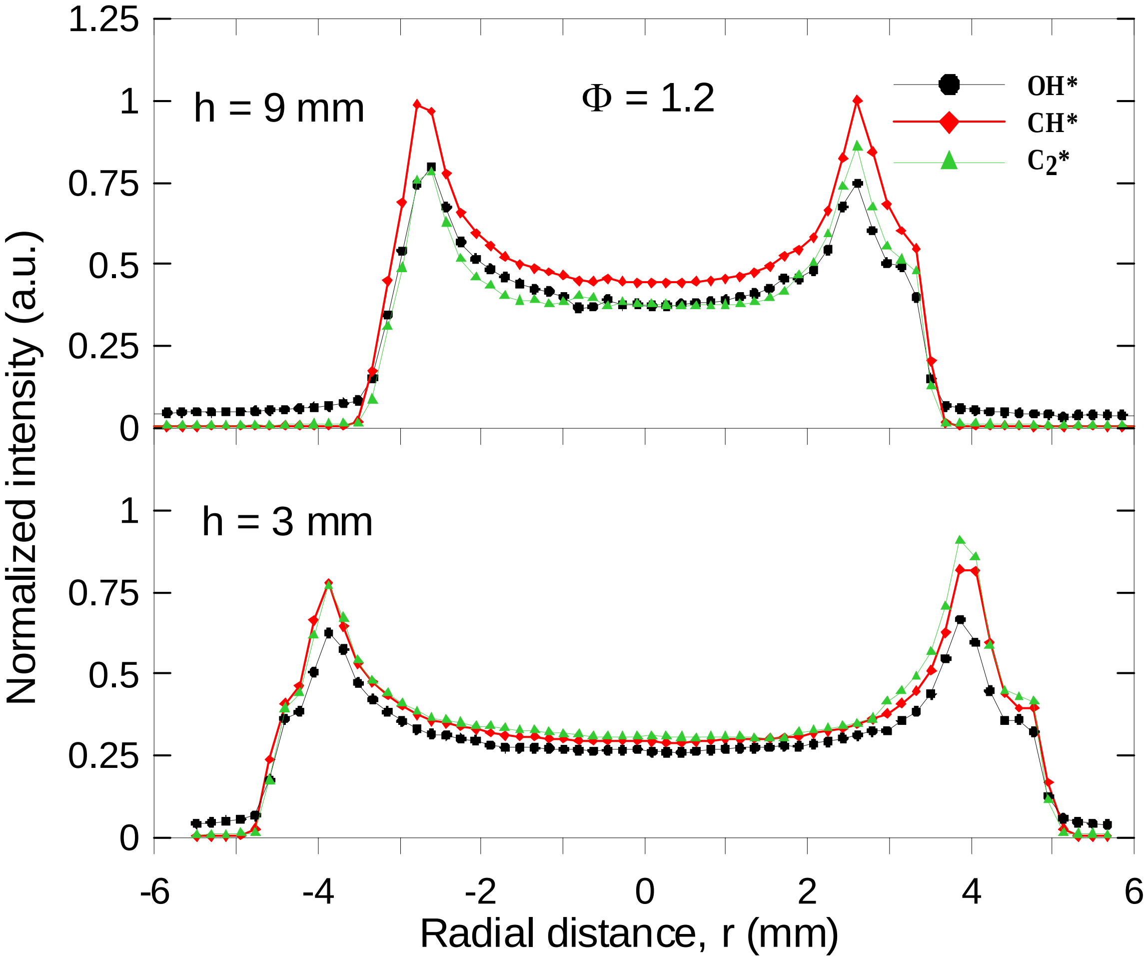

Fig. 19. Radial distribution of the OH*, CH*, and C_2* chemiluminescence intensities at *h* = 3 and 9 mm for ϕ = 1.2 flame.

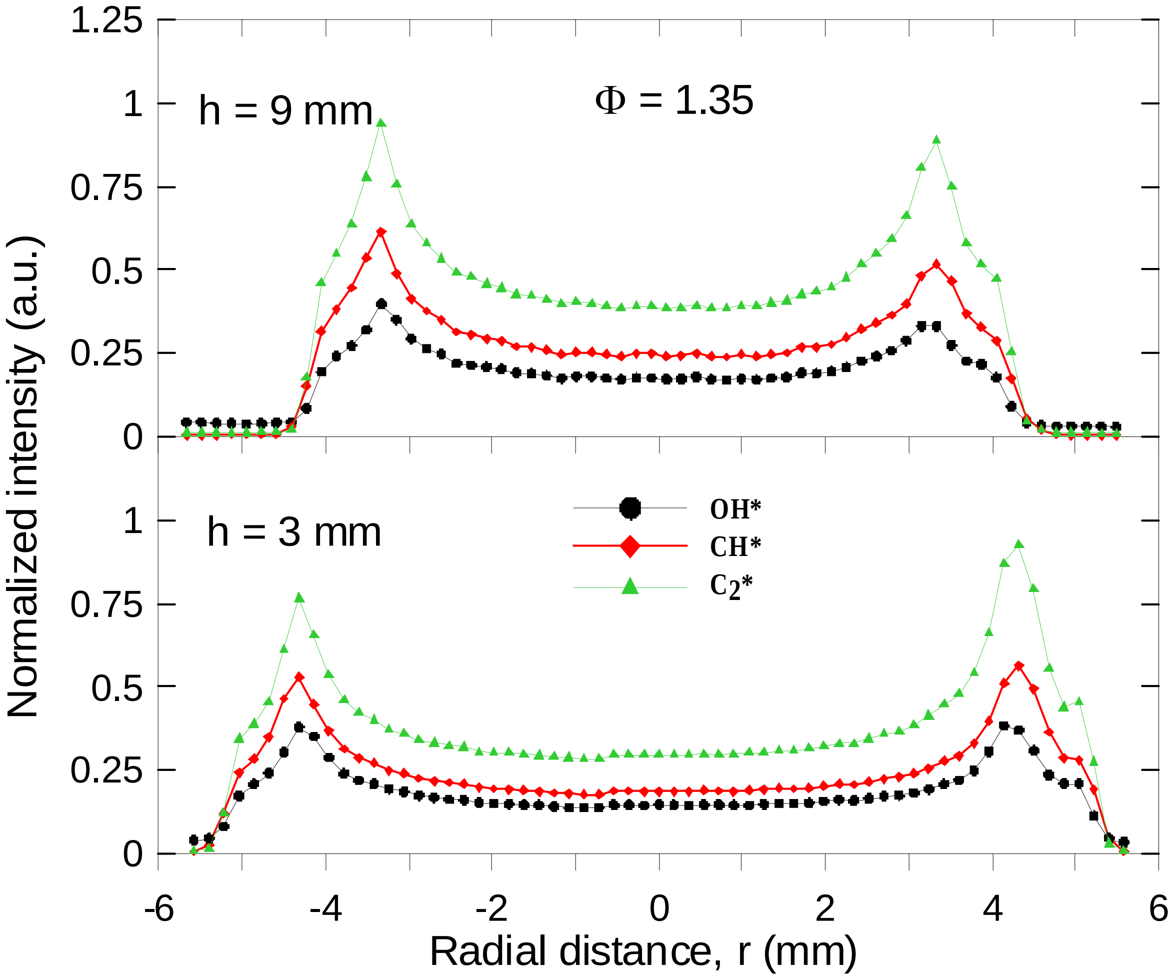

Fig. 20. Radial distribution of the OH*, CH*, and C_2* chemiluminescence intensities at *h* = 3 and 9 mm for ϕ = 1.35 flame.

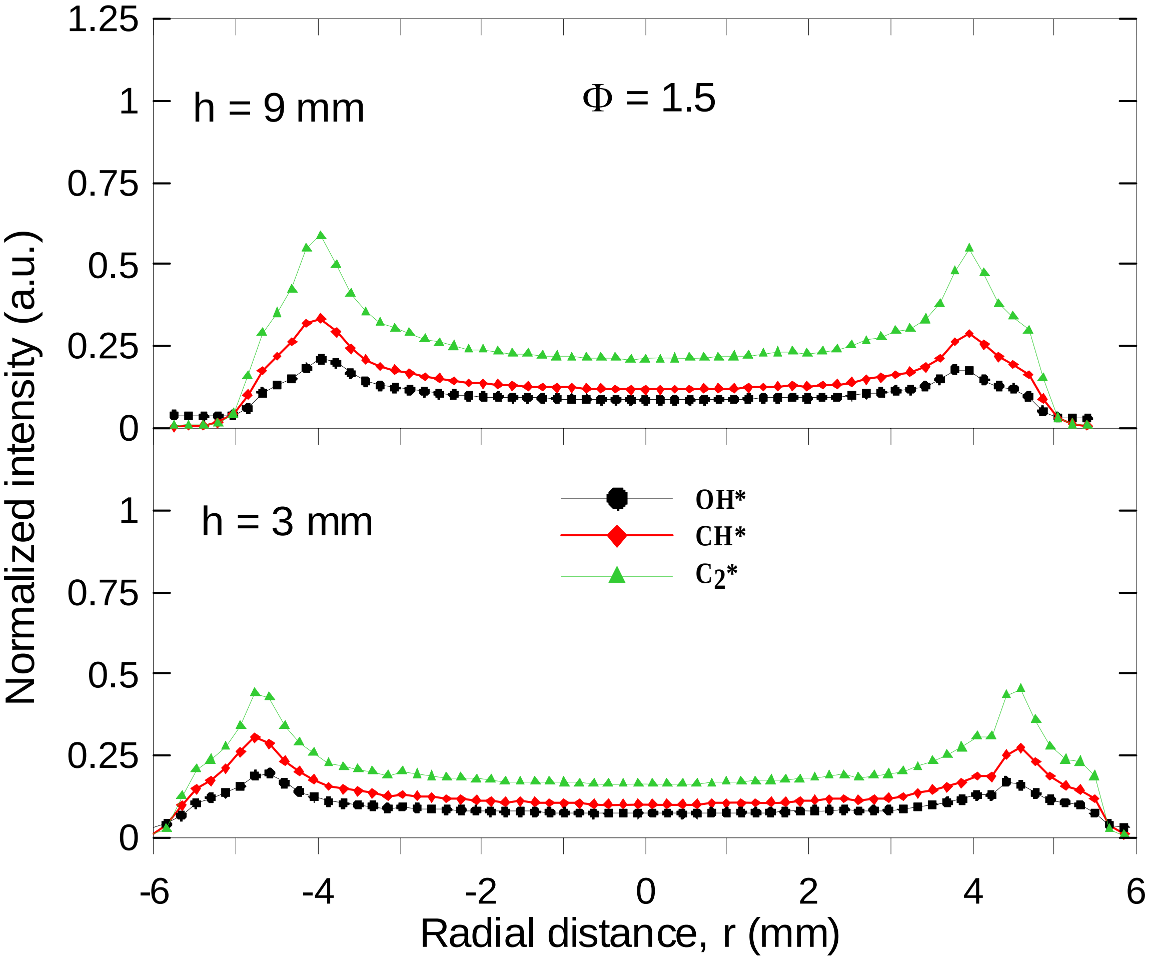

Fig. 21. Radial distribution of the OH*, CH*, and C_2* chemiluminescence intensities at *h* = 3 and 9 mm for ϕ = 1.35 flame.

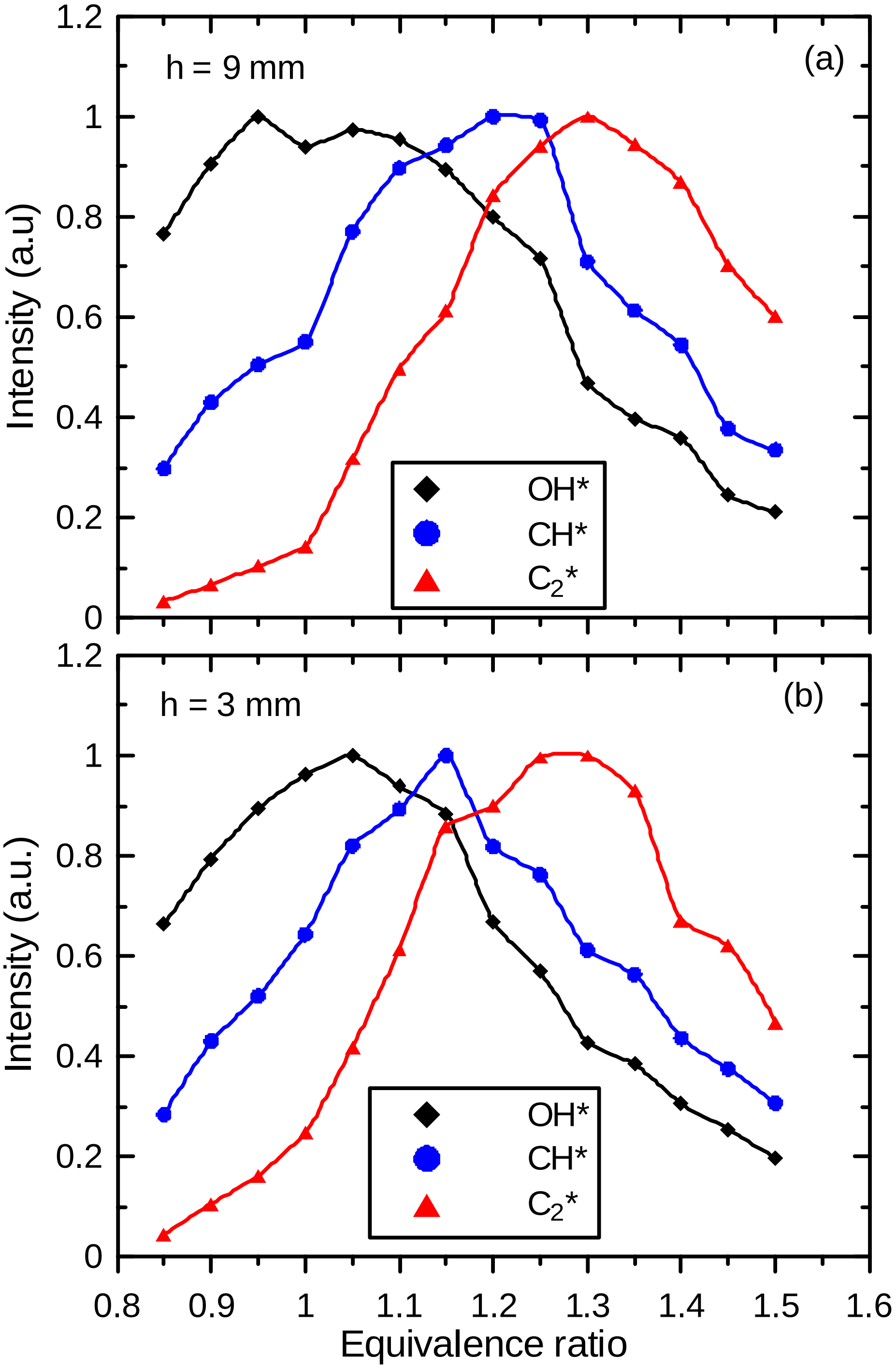

Fig. 22. Variations of the maximum chemiluminescence intensities with the equivalence ratio at $h = 3$ and 9 mm.

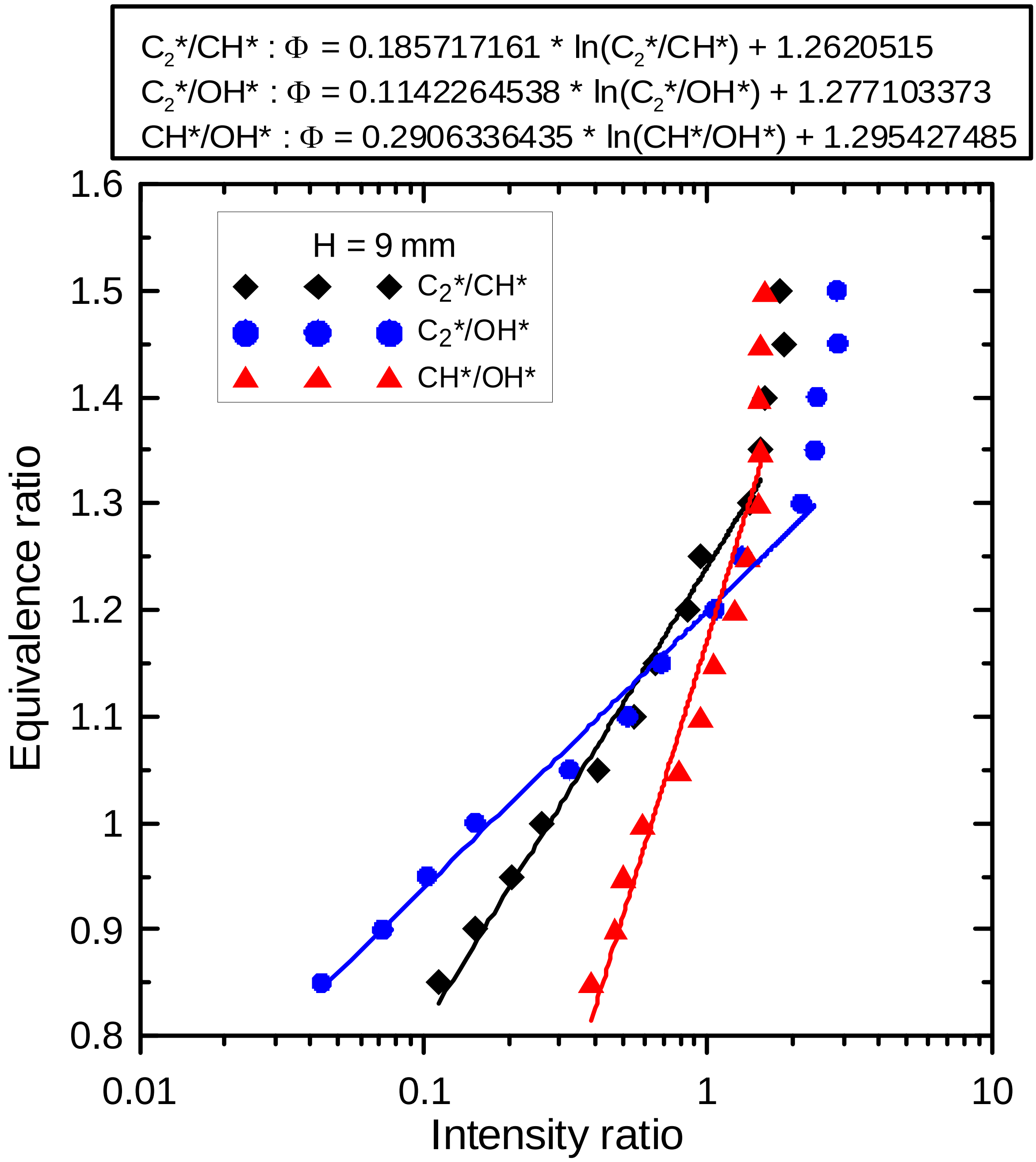

Fig. 23. Correlation of the intensity ratios of C_2*/CH*, C_2*/OH* and CH*/OH* to the equivalence ratios at *h* = 9 mm.

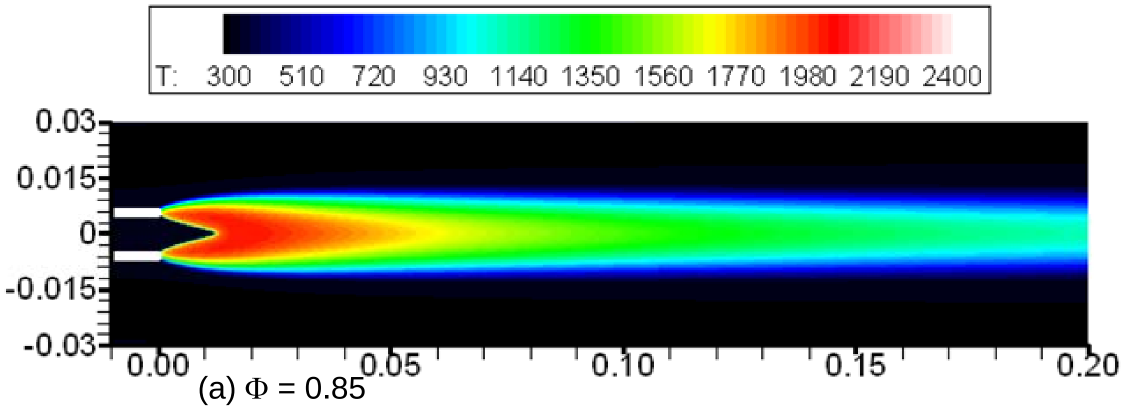

(a) $\Phi = 0.85$

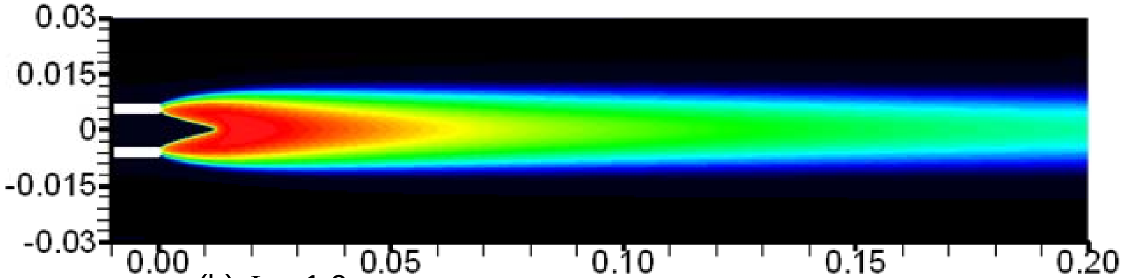

(b) $\Phi = 1.0$

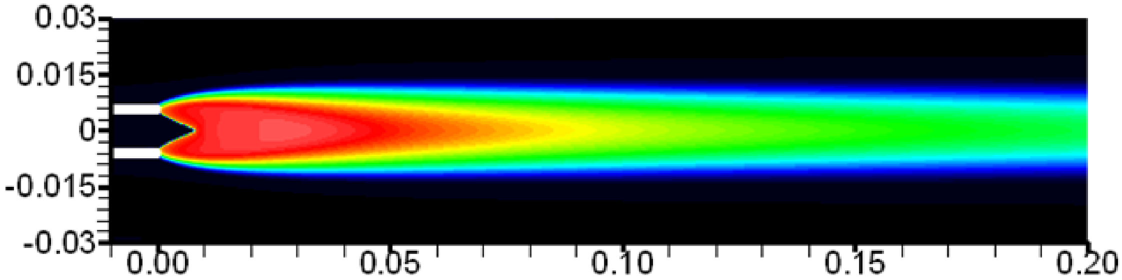

(c) $\Phi = 1.2$

Fig. 24. Computed temperature isopleths for laminar premixed CH_4-air flames at $\phi = 0.85$, 1.0, and 1.2.

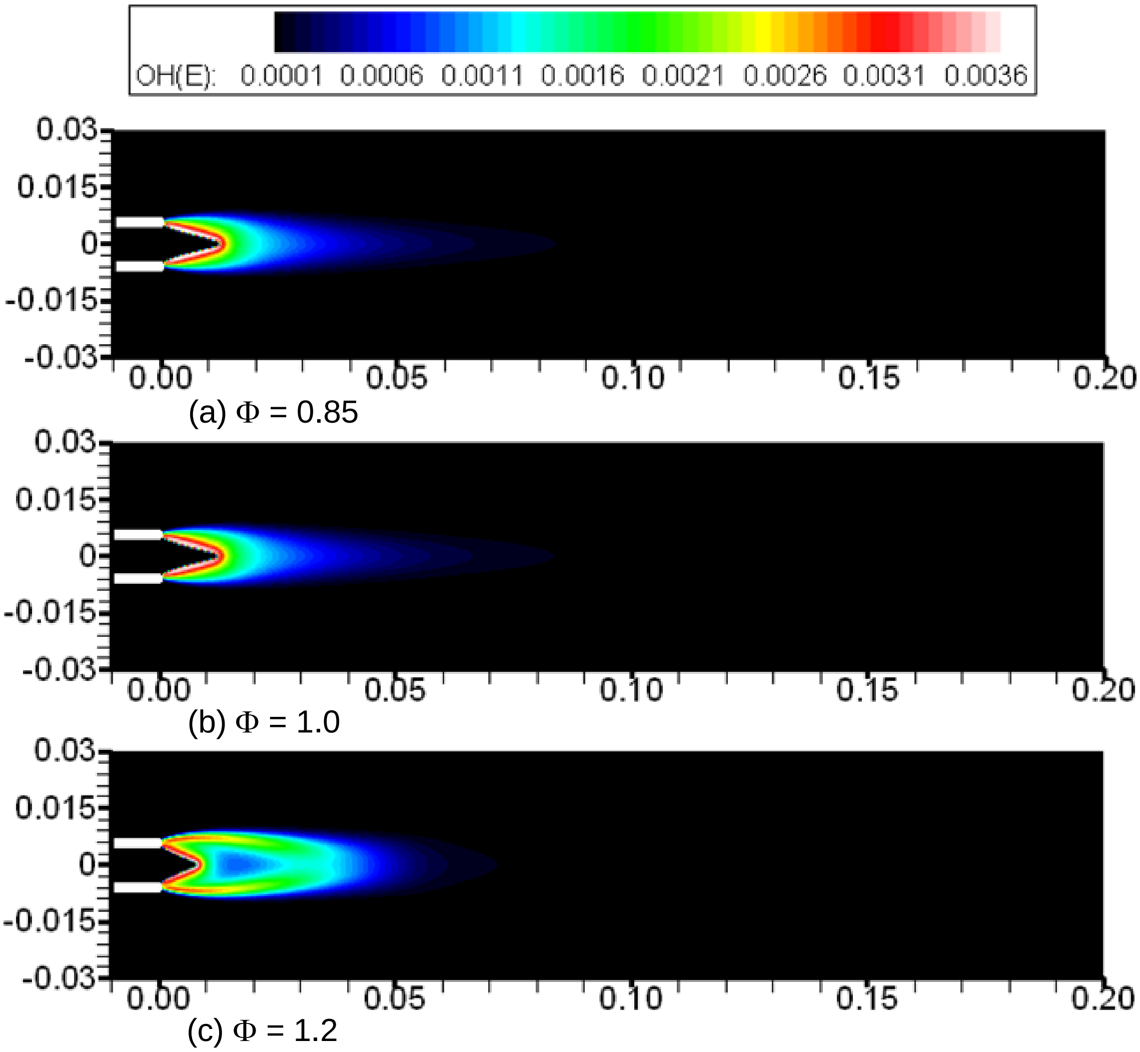

(a) Φ = 0.85

(b) Φ = 1.0

(c) Φ = 1.2

Fig. 25. Computed OH* mass fraction isopleths for laminar premixed CH_4-air flames at ϕ = 0.85, 1.0, and 1.2.

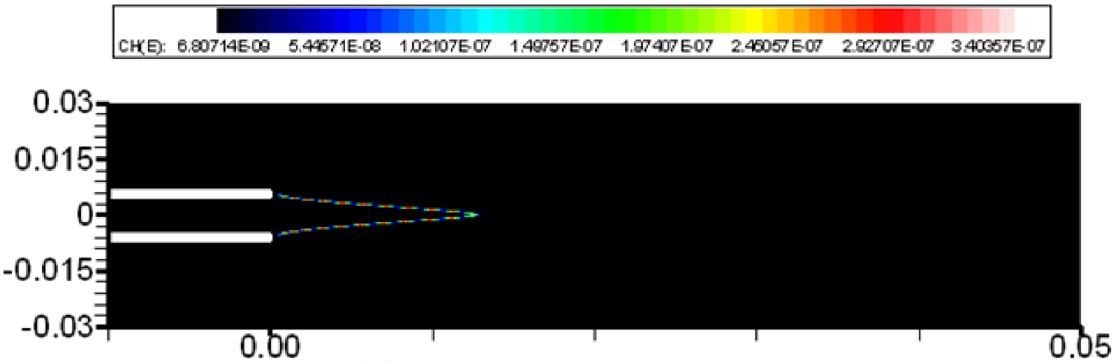

(a) Φ = 0.85

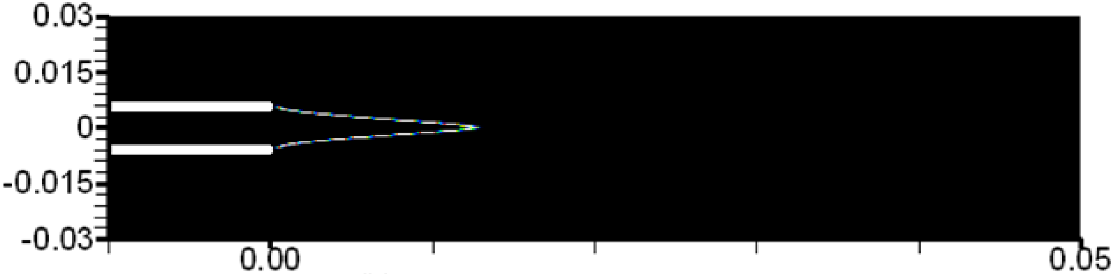

(b) Φ = 1.0

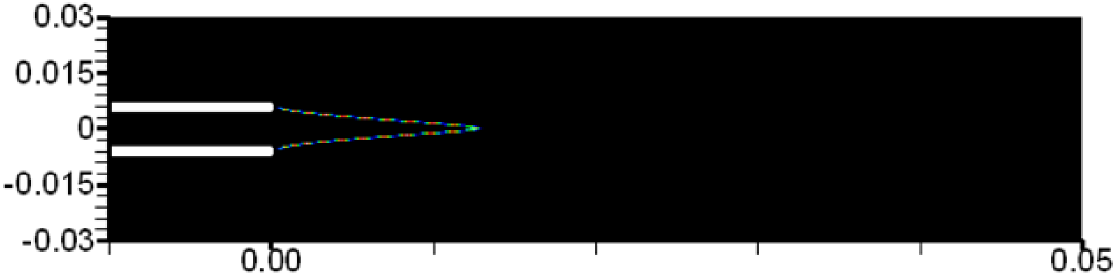

(c) Φ = 1.2

Fig. 26. Computed CH* mass fraction isopleths for laminar premixed CH_4-air flames at ϕ = 0.85, 1.0, and 1.2.

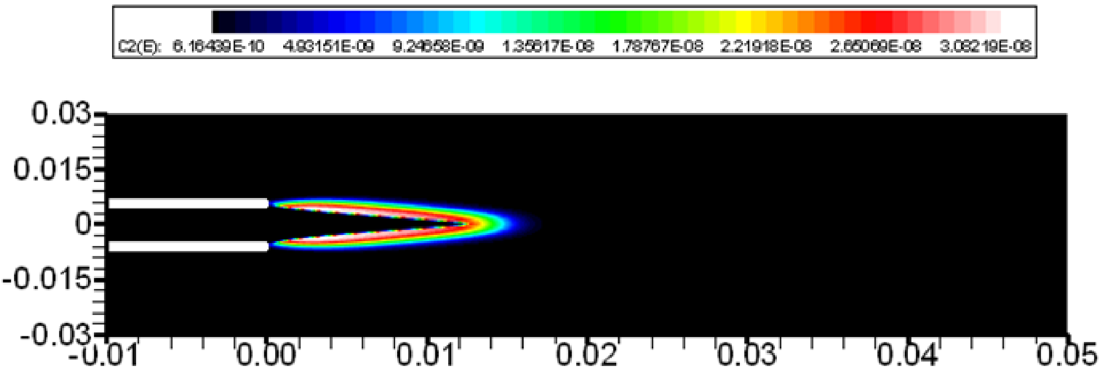

(a) $\Phi = 0.85$

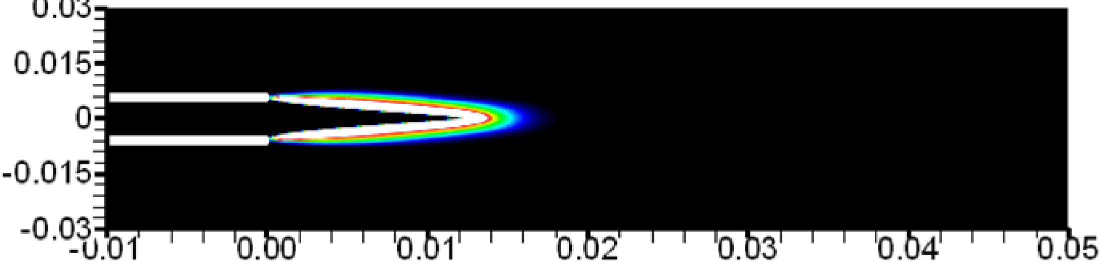

(b) $\Phi = 1.0$

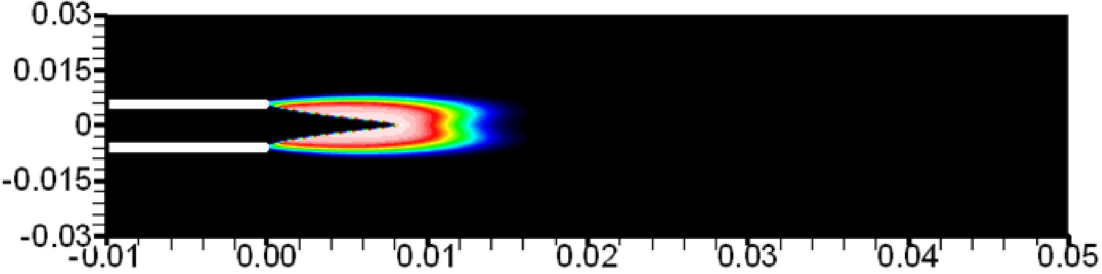

(c) $\Phi = 1.2$

Fig. 27. Computed C_2* mass fraction isopleths for laminar premixed CH_4-air flames at $\phi = 0.85$, 1.0, and 1.2.

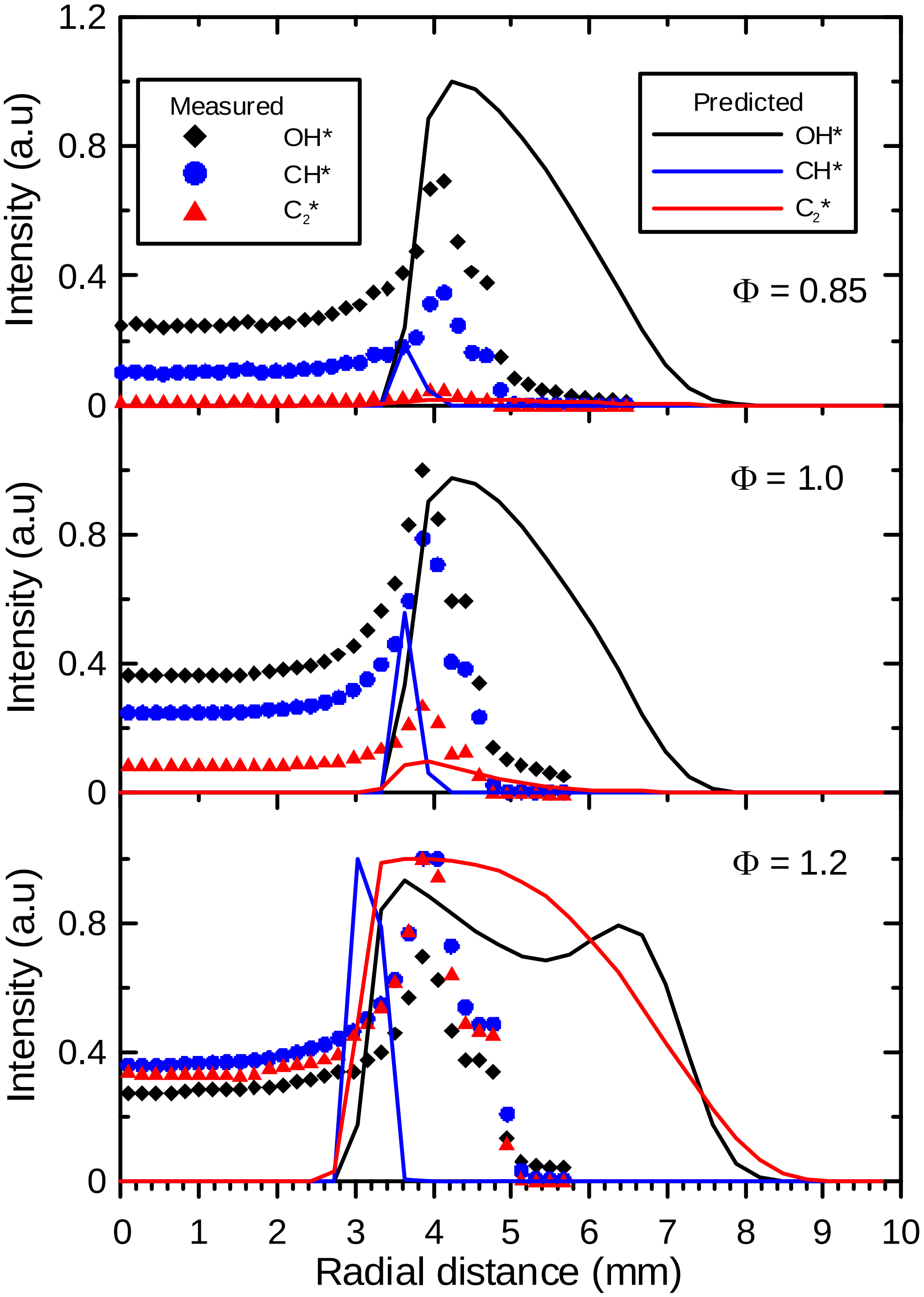

Fig. 28. Comparisons of measured and predicted radial distributions of OH*, CH*, and C_2* emissions in laminar premixed CH_4-air flames (ϕ = 0.85, 1.0, and 1.2) at *h* = 3 mm.

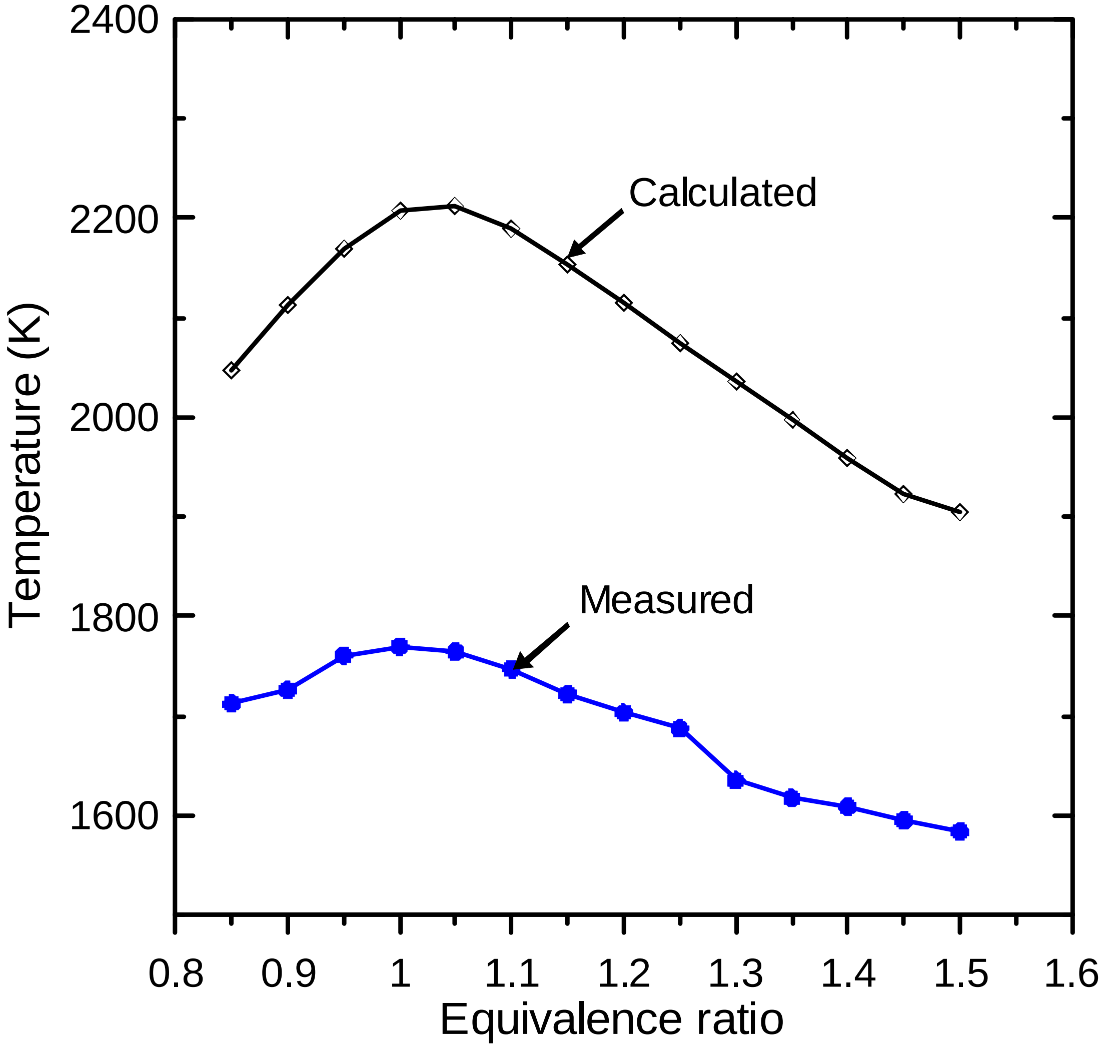

Fig. 29. Comparison of the measured and calculated adiabatic flame temperatures in laminar premixed CH_4-air flames.

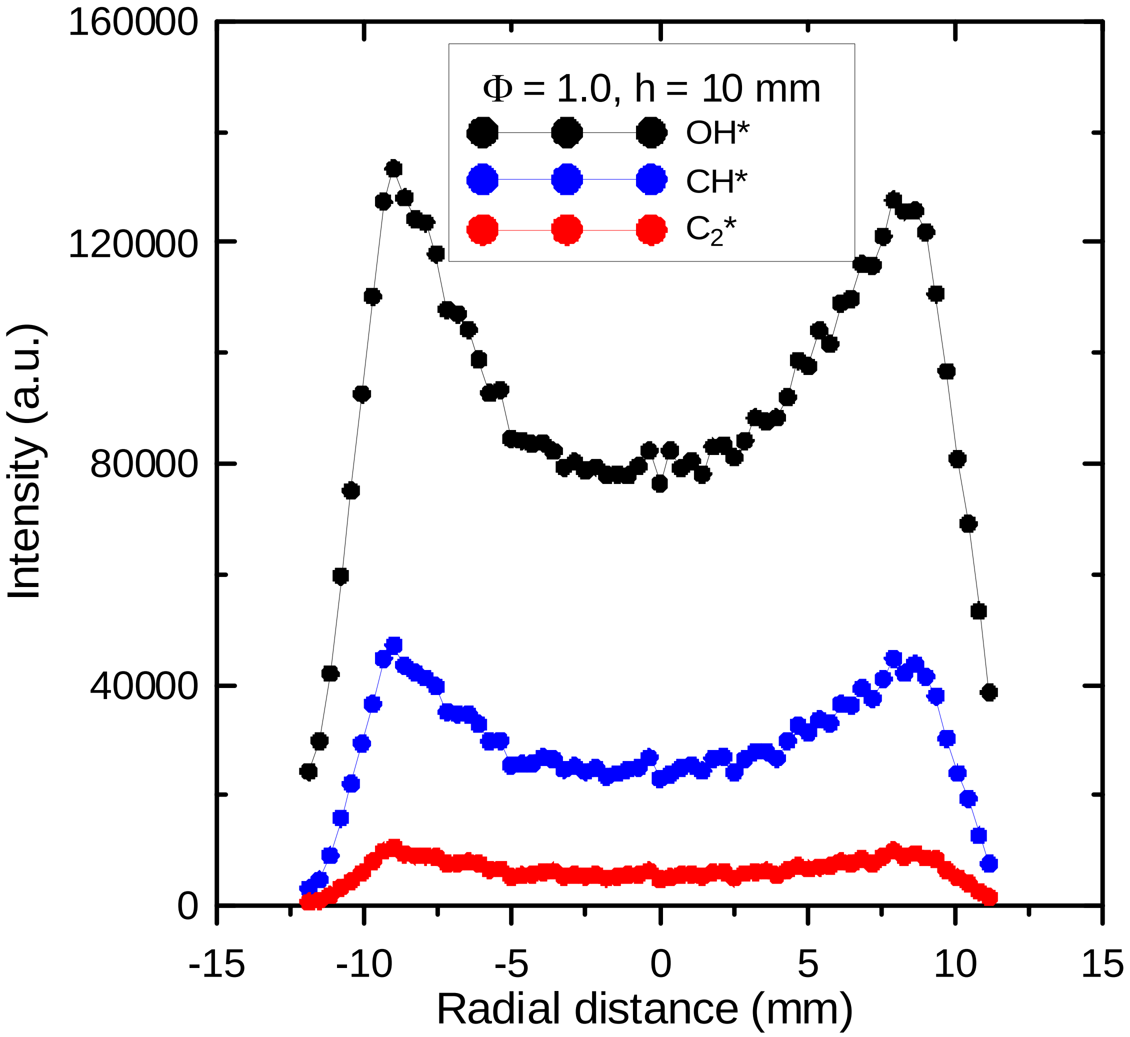

Fig. 30. Radial distribution of the OH*, CH*, and C_2 emissions in turbulent premixed stoichiometric CH_4-air flame at *h* = 10 mm.

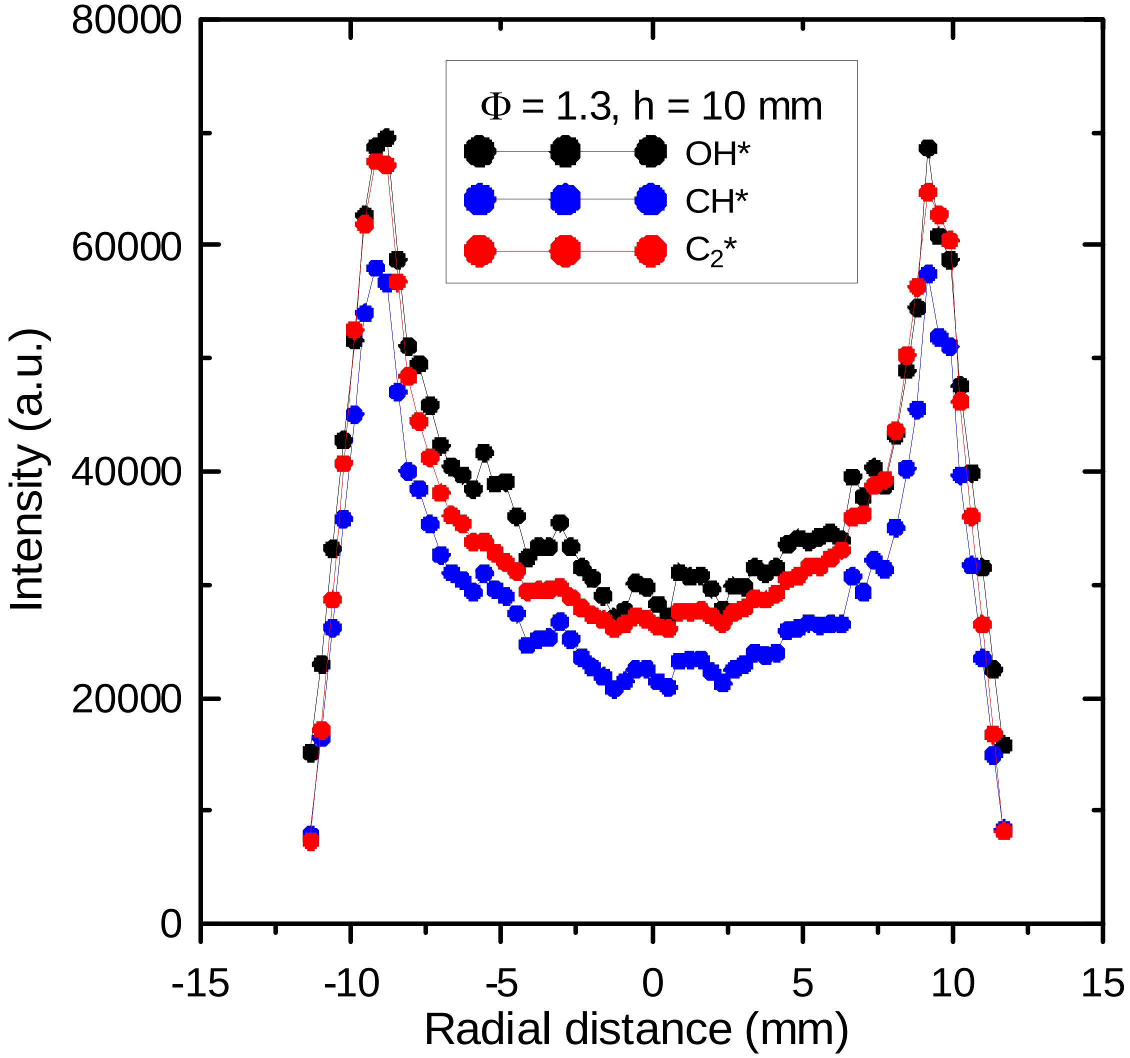

Fig. 31. Radial distribution of the OH*, CH*, and C_2 emissions in turbulent premixed rich CH_4-air flame at *h* = 10 mm.

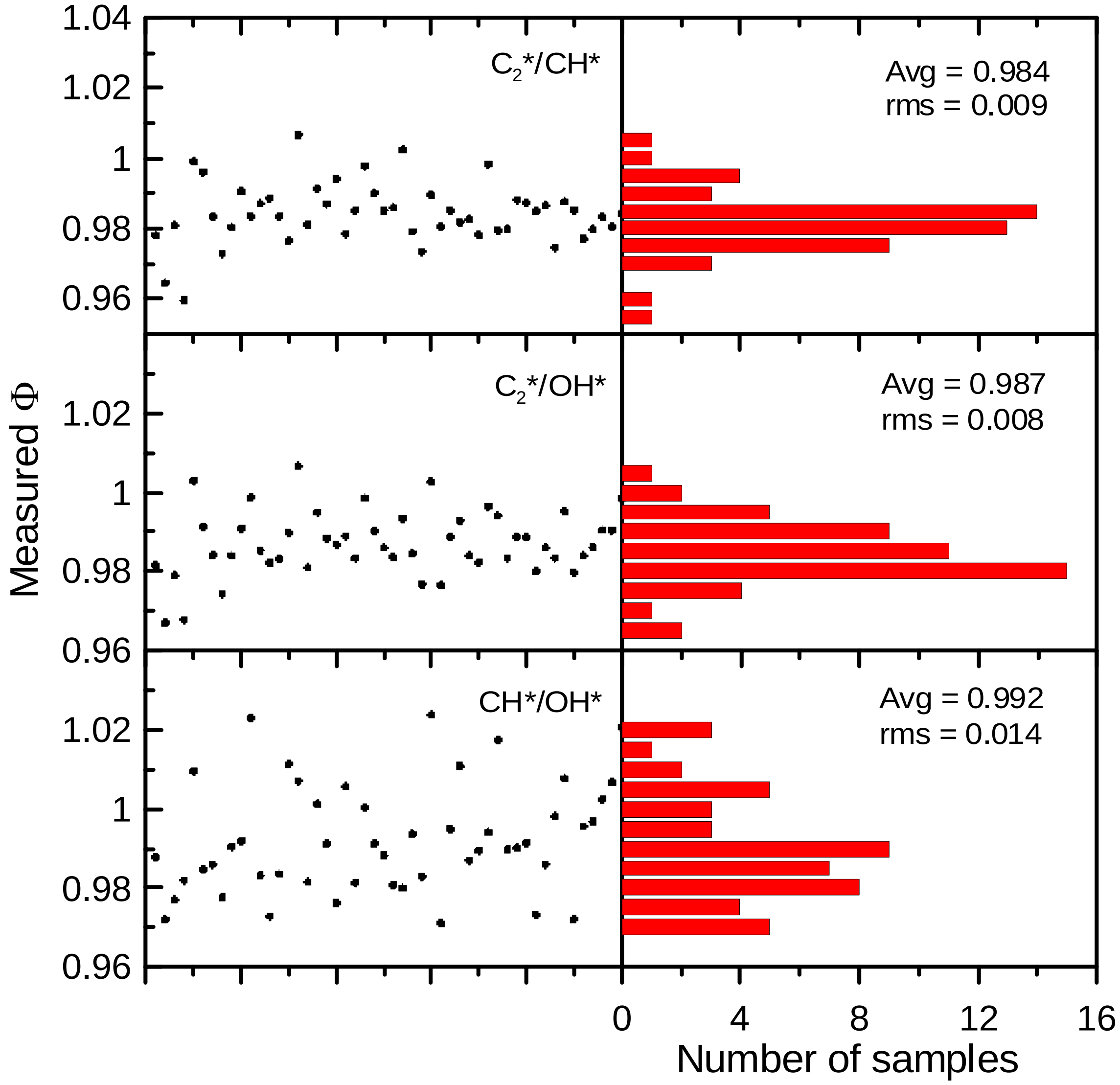

Fig. 32. Histograms of measured equivalence ratio in turbulent premixed stoichiometric CH_4-air flame at *h* = 10 mm and *r* = -9 mm.

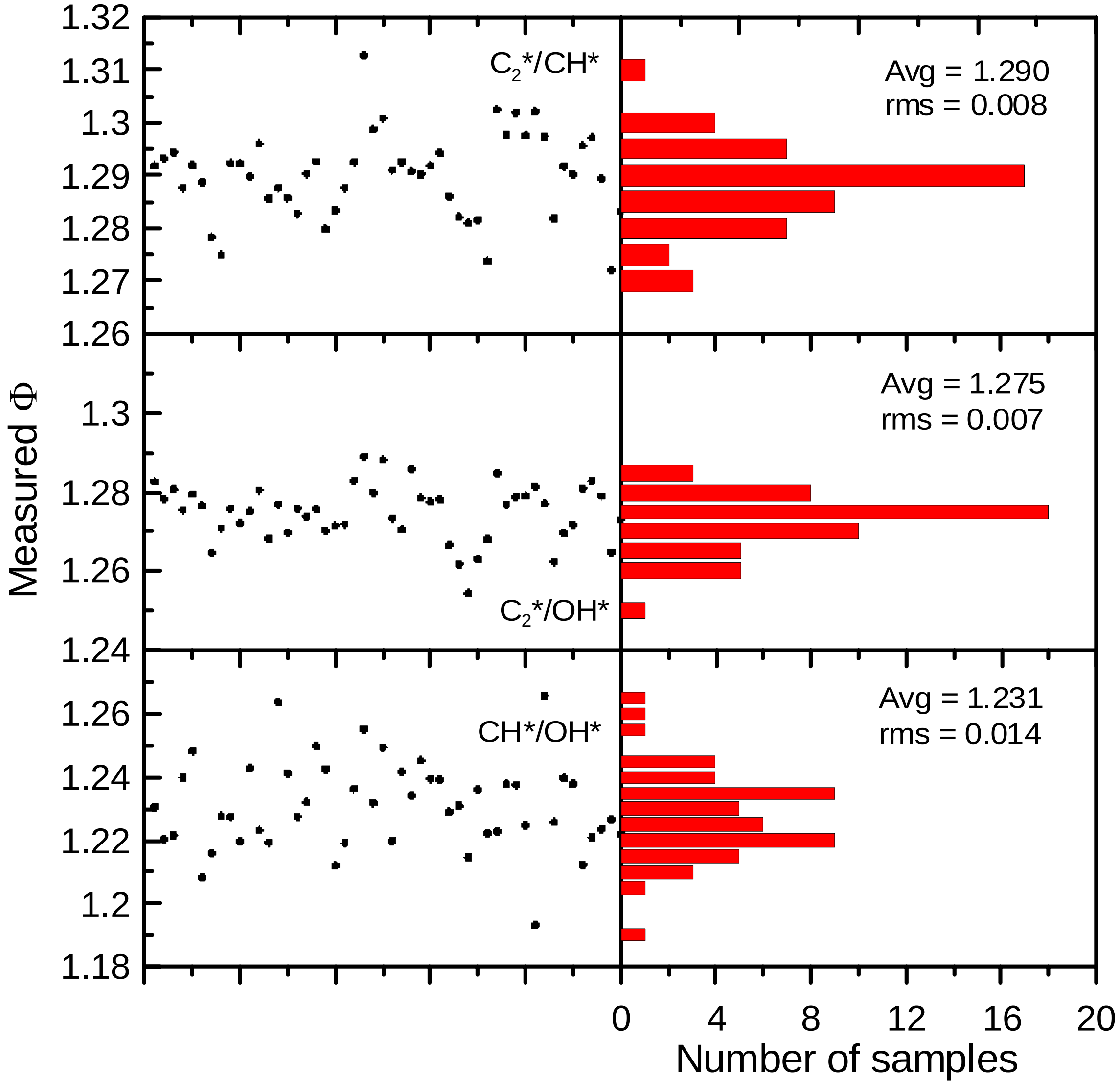

Fig. 33. Histograms of measured equivalence ratio in turbulent premixed rich CH_4-air flame at *h* = 10 mm and *r* = -9.18 mm.

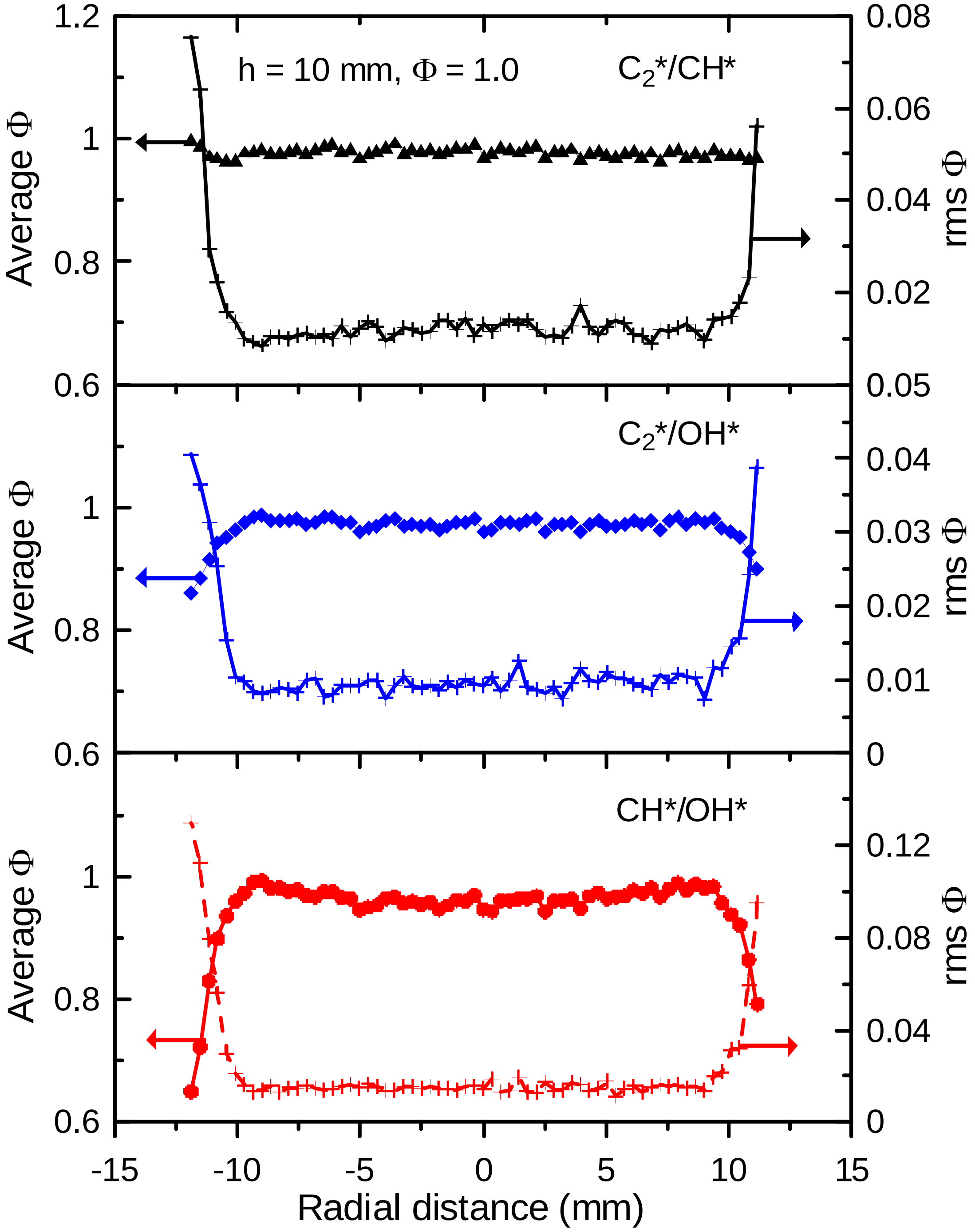

Fig. 34. Radial distribution of average and rms equivalence ratios in turbulent premixed stoichiometric CH_4-air flame measured by three different intensity ratios at *h* = 10 mm.

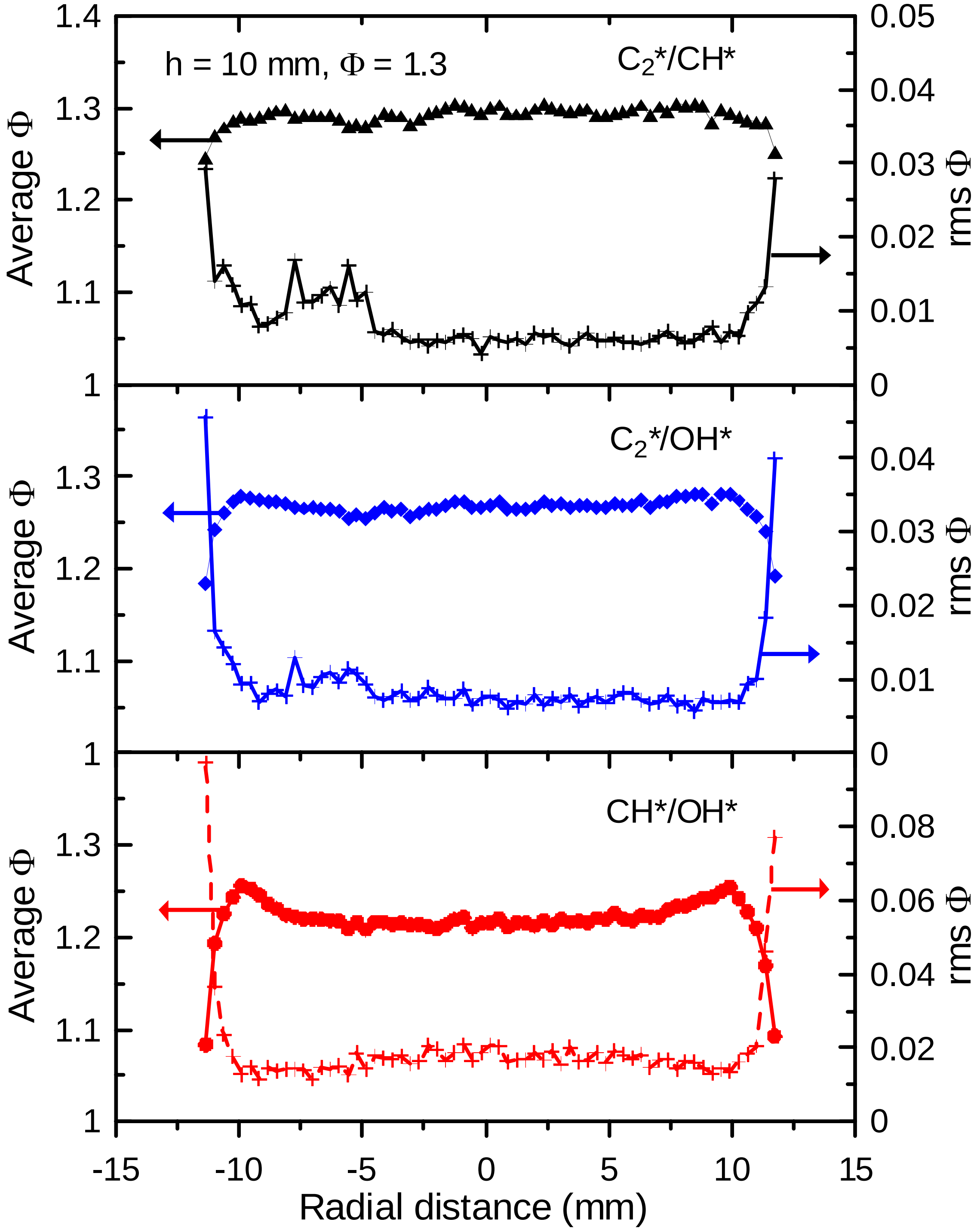

Fig. 35. Radial distribution of average and rms equivalence ratios in turbulent premixed rich CH_4-air flame measured by three different intensity ratios at *h* = 10 mm.

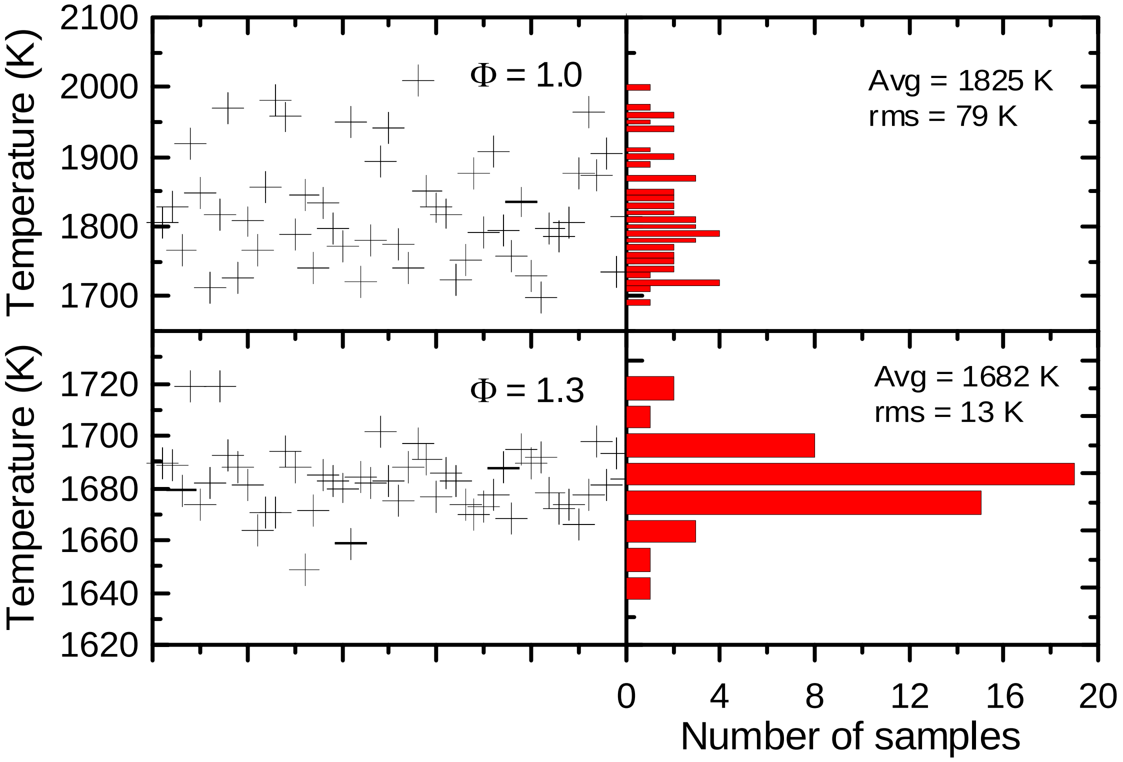

Fig. 36. Histograms of measured temperature in turbulent premixed stoichiometric and rich CH_4-air flames at h = 10 mm and r = -9 mm.

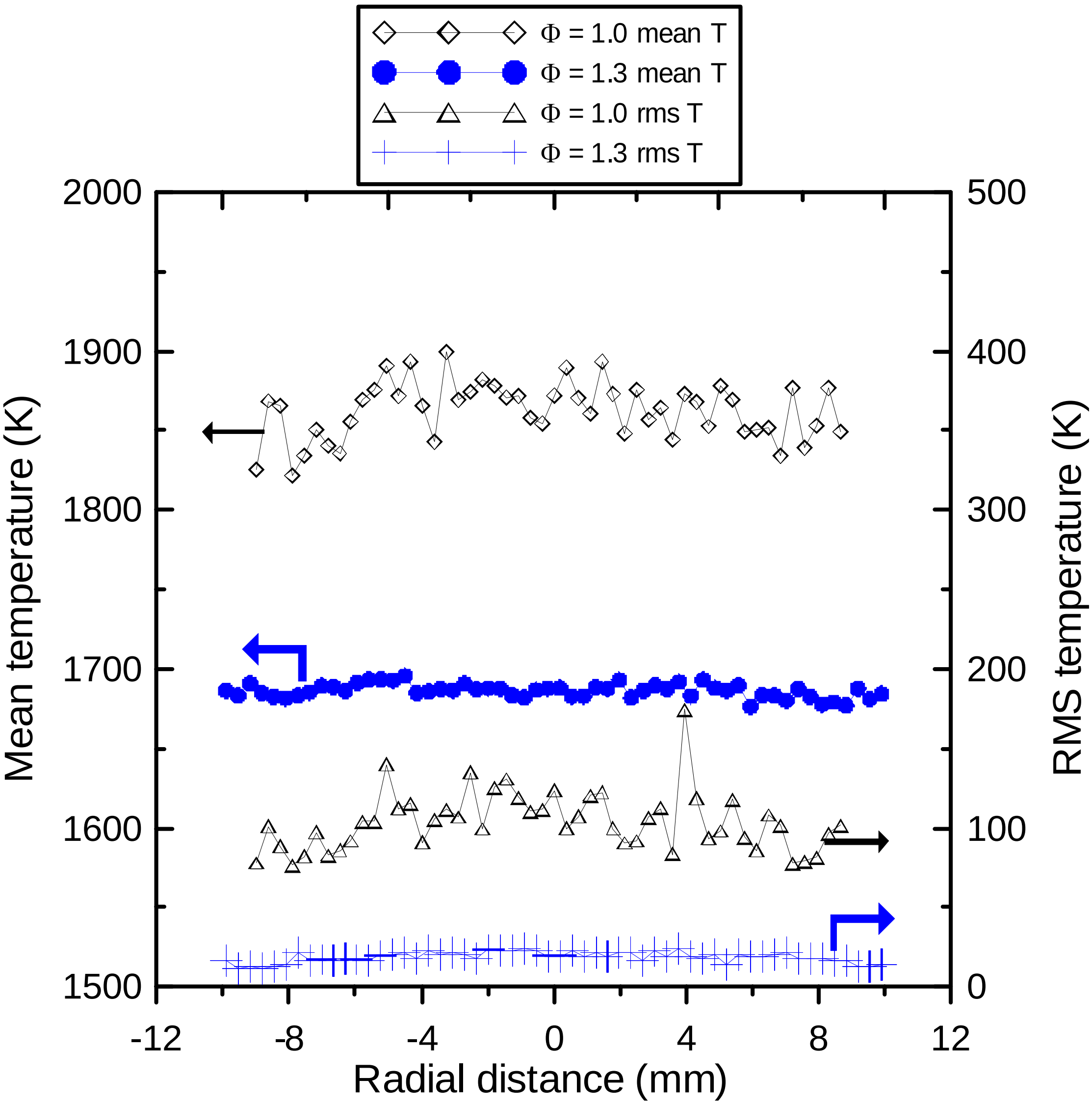

Fig. 37. Radial distribution of average and rms temperatures in turbulent premixed stoichiometric and rich CH_4-air flames at *h* = 10 mm.

APPENDIX

Development of Chemiluminescence Sensor for Combustion Measurements

火焰自燃螢光感測器之研發

T. S. Cheng

Department of Mechanical Engineering
Chung Hua University, Hsinchu, Taiwan, 300, ROC

Y.-C. Chien, Y.-C. Chao, Y.-H Li, C.-Y. Wu, Y.-Y. Cheng

Department of Aeronautics and Astronautics, National Cheng Kung University
National Cheng Kung University, Tainan, 701, Taiwan, ROC

Abstract

The objective of this research is to develop a low cost, non-laser based optical sensor for measurements of local equivalence ratio in turbulent premixed hydrocarbon flames. The ultimate goal is the application of the developed sensor in industrial furnaces for monitoring combustion process. The measurement system consists of a Cassegrain optics coupled with an optical fiber and a spectroscopic unit. This paper reports the performance of the developed optical sensor by measuring the chemiluminescence emissions of OH*, CH*, and C_2* in laminar premixed methane-air jet flames operated at several equivalence ratios ranging from 0.85 to 2.0. Experimental results indicate that this non-laser based chemiluminescence sensor can accurately measure the radial distributions of OH*, CH*, and C_2*. The ability of using the intensity ratio of C_2*/OH*, C_2*/CH*, and CH*/OH* obtained in laminar flames to measure local equivalence ratio in turbulent flames is discussed.

Keywords: Optical sensor, Cassegrain mirror, Premixed flame, Chemiluminescence

摘要

本研究之主要目的為開發可量測碳氫火焰當量比之低成本無雷射之光學感測器，將來亦可推展此量測技術為大型燃燒器之即時監控系統。本研究所開發之光學感測系統係由卡塞格倫反射鏡、光纖及裝有濾光片與光電倍增管之光譜箱組合而成。本論文探討應用所研發之光學感測器於層流預混甲烷-空氣噴流火焰之 OH*、CH*及 C_2*螢光量測，實驗結果顯示本研究所研發之光學感測器可準確的量測 OH*、CH*及 C_2*的螢光強度分佈。同時，利用層流火焰所量測之螢光強度比值作為量測紊流火焰局部當量比之可行性亦將進行討論。

關鍵字：光學感測器、卡塞格倫反射鏡、預混火焰、自然螢光

1. Introduction

According to the energy consumption report [1], the amount of energy (77,875 KLOE) consumed by the industrial and transportation sectors was 72.1% of the total annual energy consumption in Taiwan during the year of 2005. In these two sectors, about 90% of energy sources (fossil fuels) were used to generate power, process heat, and electricity through combustion. Extensive fossil fuel consumptions have resulted in rapid fuel depletion over the world as well as atmospheric and environmental pollutions. In order to burn the fuel more efficiently and effectively, the development of combustion heating and energy saving technologies is of vital importance. Various types of turbulent flames, premixed, non-premixed, or partially premixed, are employed in industrial boilers, process heating burners, internal combustion engines, hazardous waste incinerators, and both aircraft and land-based gas turbine engine combustors, etc. In order to control the turbulent combustion for reducing pollutant emission [2-4], increasing combustion efficiency [5], and obtaining stable flame holding [6, 7], the detailed structure at turbulent flame-front must be known.

It has been shown that the chemiluminesce emissions of OH*, CH*, and C_2*, resulted from electronically excited state, in hydrocarbon flames can be related to chemical reaction rate and heat release rate [8-10]. The ratios of chemiluminescence of CH*/OH* and C_2*/OH* were used to determine local equivalence ratio in laminar and turbulent flames [11, 12], atmospheric pressure micro-gas turbine combustor [13], and swirl and liquid fuel combustors [14]. Most of these chemiluminescence measurements used traditional lenses to collect the global emissions, and there is insufficient spatial resolution to measure the local equivalence ratio at the flame front. To overcome this deficiency, a Cassegrain optics with high spatial resolution must be used [12, 13, 15, 16]. In the present study, a Cassegrain optics coupled with an optical fiber and a spectroscopic unit is used to simultaneously detect OH*, CH*, and C_2* emissions in laminar premixed methane/air flames. The correlation between the intensity ratio (CH*/OH*, C_2*/CH*, and C_2*/OH*) and the equivalence ratio is obtained to elucidate the possibility of using this corrlation for local equivalence ratio measurements in turbulent premixed flames.

2. Experimental Apparatus

The schematic diagram of the Cassegrain optics is shown in Fig. 1. The Cassegrain optics consists of a primary and a secondary mirror, which avoids the generation of chromatic aberrations for different wavelengths. The Cassegrain optics is designed by the ray-tracing method. The designed rms spot size of Cassegrain optics is 328 μm and the magnification ratio is 2.36. In order to improve the Cassegrain optics for a micro-level adjustment and to connect with the optical fiber for light collection, the optical holder is re-designed. In addition, a circular mask with different slit widths at the center can be placed in front of Cassegrain optics at the secondary mirror so that the background flame emission signals located away from the effective sample volume is minimized [16].

The schematic diagram and photograph of the measurement system are shown in Fig. 2. A jet burner (i.d. = 10 mm) is used to produce laminar premixed methane-air flames operated at several different equivalence ratios ranging from fuel-lean to fuel-rich conditions (ϕ = 0.85-2.0) for the emission measurements. Chemiluminescence signals emanating from the sample volume are collected and focused by the Cassegrain optics and relayed to the entrance slit of a spectroscopic unit through a 2-m long optical fiber (core diameter = 100 μm). A collimated lens is coupled to the end of optical fiber for expanding the light rays. In the spectroscopic unit, three dichroic mirrors are used to separate different wavelengths of optical emissions. Particular regions of wavelength corresponding to OH*, CH*, and C_2* are extracted through the narrowband interference filters and detected by the side-on type photomultiplier tubes (PMTs). The specifications (center wavelength/full width at half maximum) of the interference filters for OH*, CH*, and C_2* are 307.3/22.2 nm, 432.1/10.5 nm, and 516.3/8.5 nm, respectively. The current output from the PMTs are simultaneously amplified and digitized with a 12-bit A/D converter. The output signals are stored in a personal computer for data reduction.

3. Results and Discussion

In order to understand the capability of the Cassegrain optics for “point” measurements of optical emissions, the spatial resolution of the Cassegrain optics is measured using an inverse ray tracing method. A diode laser is used to shine the red-light from the back-end of the optical fiber and to form a red spot at the focal point of the Cassegrain mirror. A CCD camera is directly placed at the focal point and moved along the optical axis to measure the light intensity profile. The measured light intensity distribution is depicted in Fig. 3. Figure 3a shows the light-collection rate distribution at the focal point. It can be seen that the distribution of light intensity is not in a perfectly circular shape. This could be due to slightly misalignment between the laser light and the optical fiber or due to non-uniformity of the CCD chip. However, the high-intensity region indicates that a circular focal point with approximately 40 μm in diameter is achieved for the Cassegrain optics. The light intensity, defined by setting the threshold value at e^{-2} times the peak value, along the optical axis and its 3-D distribution are shown in Figs. 3b and 3c, respectively. The effective probe volume determined from Fig. 3c is found to be 40 μm in diameter and 600 μm in length. The effective probe volume of the present Cassegrain optics is slightly better than that (100 μm in diameter and 800 μm in length) designed by Kojima et al. [16].

Prior to the chemiluminescence emission measurements, the effect of the slit width of the eye-mask on the reduction of background flame emissions is examined. Figure 4 shows that the measured OH* with the mask have narrower profiles, while that without the mask yields a broader profile due to a contribution from background flame emissions collected outside the effective probe volume. We also rotate the slit angles and found that the measured OH* has a narrower profiles when the slit centerline is parallel to the flame axis. This findings is in agreement with that observed by Kojima et al. [16]. After considering a trade-off relation between the slit width and the signal-to-noise ratio of the peak value, we found that the best performance of the eye-mask for the present study is a 5-mm-wide slit with the slit centerline arranged parallel to the flame axis (see Fig. 2).

Simultaneous measurements of OH*, CH*, and C_2* chemiluminescence emissions are made in laminar premixed methane-air jet flames (ϕ = 0.85-2.0) to examine the applicability of the developed sensor system. The radial distributions of normalized OH*, CH*, and C_2* intensities at h = 3 and 9 mm for ϕ = 0.85, 1.0, 1.1, 1.2, and 1.3 flames are shown in Figs. 5-9, respectively. The measured maximum intensity of OH*, CH*, and C_2* in the flames studied is used to respectively normalize each of emission signals, so that direct comparison of chemiluminescence intensity for different flame conditions can be made. It is noted that the radial location of local maximum chemiluminescence intensity is an indication of flame front position. In addition, the OH*, CH*, and C_2* intensities of the hydrocarbon flames are functions of the relative heat release rate and their concentrations. Moreover, the profile of the OH* spectra has been correlated to the flame temperature and the CH* is an important indicator of the prompt NO formation [17].

Figure 5 shows the radial distributions of OH*, CH*, and C_2* intensities at h = 3 and 9 mm for ϕ = 0.85 flame. It can be seen that the peak OH* and CH* chemiluminescence signals occur at r = 3.51 mm and no C_2* signal is detected near the burner exit (h = 3 mm). At downstream location (h = 9 mm), the C_2* signal increases and three emission signals peak at r = 2.25 mm. The shift of peak intensity location from r = 3.51 to 2.25 mm indicates that the flame front position moves towards the center of the flame with increasing downstream location. The low C_2* emissions in lean flame conditions have also been observed by Kojima et al. [12]. Similar radial distributions of OH*, CH*, and C_2* intensities at h = 3 and 9 mm for ϕ = 1.0, 1.1, 1.2, and 1.3 flames are shown in Figs. 6-9. It is noted that the high level of intensities between the two peaks is due to background flame emissions. This fact suggests that although the present sensor is designed for "point" measurement, the emissions outside the probe volume are not completely eliminated by the eye mask. Figures 5-9 also indicate that the flame width is increased as the euqivalence ratio is increased from fuel-lean to fuel-rich conditions. For instance, the peak OH* intensity locates at r = 3.51 mm for the ϕ = 0.85 flame at h = 3 mm and it shifts to r = 4.14 mm for ϕ = 1.3 at the same height. The increase of the flame width in the richer flames indicates that it requires a broader region for the fuel to be consumed.

Comparisons of the measured maximum intensity for ϕ = 0.85-2.0 at h = 3 and 9 mm are shown in Fig. 10. Results indicate that at both heights the maximum OH*, CH*, and C_2* intensities occur approximately at ϕ = 1.0, 1.1, and 1.25 respectively. These findings are in good agreement with experimental results of Kojima et al. [12], but depart from those measured by Jeong et al. [18]. Kojima et al. found that the peak OH* intensity occurred at ϕ = 1.1, CH* at 1.2, and C_2* at 1.3. Whereas Jeong et al. measured the peak intensities of OH*, CH*, and C_2* at ϕ = 0.86, 0.91, and 1.06, respectively. The closer agreement between our results and the data of Kojima et al. could be due to that a similar Cassegrain light collection system was used for the measurements.

It has been suggested that the chemiluminescence intensity ratio of CH* to OH* or C_2* to CH* or OH* and the equivalence ratio in hydrocarbob flames have a nearly linear relationship [12, 13, 19]. These suggestions were based on results showing that the chemiluminescence intensity was very sensitive to the equivalence ratio. In addition, the possibilities that the effects of temperature, pressure, and the size of the flame on the emission intensity could be canceled to detect the equivalence ratio. Therefore, the correlation between the chemiluminescence intensity ratio and the euqivalence ratio at the flame front is investigated.

Figure 11 shows the results of C_2*/CH*, C_2*/OH*, and CH*/OH* against the equivalence ratio for the local flame front of the laminar premixed methane-air jet flames at h = 3 and 9 mm. In Fig. 11, the peak emission intensities of OH*, CH*, and C_2* shown in Fig. 10 are used to determine C_2*/CH*, C_2*/OH*, and CH*/OH*. It can be seen in Fig. 11b that near the burner exit (h = 3 mm) the fluctuational levels of C_2*/CH* and C_2*/CH* are higher than that of CH*/OH* due to low C_2* emissions are produced at this downstream location. At h = 9 mm (Fig. 11a), the scatter of the C_2*/CH*, C_2*/OH*, and CH*/OH* is greatly reduced because higher emission intensities of OH*, CH*, and C_2* are generated. Figure 11 shows that the correlation of C_2*/CH*, C_2*/OH*, and CH*/OH* to the equivalence ratio is nearly linear when the equivalence ratio is less than 1.35. The high degree of correlation suggests that the local flame stoichiometry at the flame front of premixed methane-air flames can be determined by the spatially resolved chemiluminescence measurements. However, it seems difficult to measure the equivalence ratio in methane-air flames for $\phi > 1.35$ by using this system because nonlinear relationship is observed within this range. These findings are in excellent agreement with those obtained by Kojima et al [12].

Figure 11 also indicates that the variation of C_2*/OH* curve is most sensitive to the equivalence ratio and C_2*/CH* is the next most sensitive. However, the use of C_2*/OH* and C_2*/CH* correlations for determining the local equivalence ratio becomes less reliable for lean flame conditions, because the C_2* emission intensity is very low at $\phi < 1.0$, as shown in Fig. 5. On the other hand, the correlation of CH*/OH* can be used for determining the equivalence ratio in lean premixed flame conditions, because the CH* and OH* emissions can be observed clearly, as shown in Fig. 5. These results suggest that the spatially resolved emission intensity ratio of CH*/OH* can be used to determine the local flame stoichiometry in the reaction zone of premixed hydrocarbon flames for a wider range of equivalence ratios.

4. Conclusions

A low cost, non-laser based optical sensor that consists of a Cassegrain optics coupled with an optical fiber and a spectroscopic unit is developed. The effective probe volume of the present Cassegrain optics is determined to be 40 μm in diameter and 600 μm in length. The performance of the developed optical sensor is verified by measuring the chemiluminescence emissions of OH*, CH*, and C_2* in laminar premixed methane-air jet flames operated at several equivalence ratios ranging from 0.85 to 2.0. Experimental results show that no C_2* emission is produced in the reaction zone of lean flames ($\phi \leq 0.95$) near the burner exit. And the flame width, indicated by the radial distributions of peak intensities of OH*, CH*, and C_2*, is increased as the equivalence ratio is increased from fuel-lean to fuel-rich conditions. The maximum OH*, CH*, and C_2* intensities are found to occur approximately at ϕ = 1.0, 1.1, and 1.25 respectively. Moreover, the high corelations between the peak intensity ratios of C_2*/CH*, C_2*/OH*, and CH*/OH* and the equivalence ratio can be used to determine the local flame stoichiometry. Of these three intensity ratios, the C_2*/OH* curve is the most sensitive to the equivalence ratio when $1.0 \leq \phi \leq 1.35$. The CH*/OH* can be used to determine the local flame stoichiometry in the reaction zone of premixed hydrocarbon flames for a wider range of equivalence ratios.

Acknowledgements

This work was supported by the National Science Council of the Republic of China under Grant numbers NSC 95-2212-E-216-018-MY2.

References

[1] Bureau of Energy, Ministry of Economic Affairs. http://www.moeaec.gov.tw/ecw.asp

[2] Lefebvre, A. H., Gas Turbine Combustion (2nd ed), Taylor & Francis, Philadelphia, 1999.

[3] Grosshandler, W., Hamins, A., McGrattan, K. and Rao Charagundla, S. and Presser, C., "Suppression of a Non-Premixed Flame Behind a Step", *Proc. Comb. Inst.* **28**: 2957-2964, 2000.

[4] Demayo, T. N., Miyasato, M. M. and Samuelsen, G. S., "Hazardous Air Pollutant and Ozone Precursor Emissions From a Low-NOx Natural Gas-Fired Industrial Burner", *Proc. Comb. Inst.* **27**: 1283-1291, 1998.

[5] Kuo, K. K., Principles of Combustion, John Wiley and Sons, Inc., NY, 1986.

[6] Hayashi, S., Yamada, H., Shimodaira, K. and Machida, T., "NOx Emissions From Non-Premixed, Direct Fuel Injection Methane Burners at High-Temperature and Elevated

Pressure Conditions", *Proc. Comb. Inst.* **27**: 1833-1839, 1998.

[7] Lieuwen, T. and Zinn, B. T., "The Role of Equivalence Ratio Oscillations in Driving Combustion Instabilities in Low NOx Gas Turbines", *Proc. Comb. Inst.* **27**: 1809-1816, 1998.

[8] Gaydon, A. G. and Wolfhard, H. G. *Flames: Their Structure, Radiation, and Temperature.* Fourth edition, Chapman and Hall, 1978.

[9] Lawn, C. J., "Distributions of instantaneous heat release by the cross-correlation of chemiluminescent emissions", *Combust. Flame*, **123**, 227-240, 2000.

[10] Najm, H. N., Paul, P. H., Mueller, C. J. and Wyckoff, P. S., "On the adequacy of certain experimental observables as measurements of flame burning rate", *Combust. Flame*, **113**:312-332, 1998.

[11] Roby, R. J., Reaney, J .E. and Johnsson, E. L., "Detection of Temperature and Equivalence Ratio in Turbulent Premixed Flames Using Chemiluminescence", *Proceedings of the 1998 International. Joint Power Generation Conference*, **1**: 593-602, 1998.

[12] Kojima, J., Ikeda, Y., and Nakajima, T., "Spatially resolved measurement of OH*, CH* and C_2* chemiluminescence in the reaction zone of laminar methane/air premixed flames", *Proc. Combust. Inst.*, **28**, 1757-1764, 2000.

[13] Hardalupas, Y., Orain, M., Panoutsos, C. S., Taylor, A.M.K.P., Olofsson, J., Seyfrid, H., Richter, M., Hult, J., Aldén, M., Hermann, F. and Klingmann, J., "Chemiluminescence sensor for local equivalence ratio of reacting mixtures of fuel and air (FLAMESEEK)". *Appl. Therm. Eng.* **24**, 1619-1632, 2004.

[14] Muruganandam, T. M., Kim, B.-H., Morrell, M. R., Nori, V., Patel, M., Romig, B. W. and Seitzman, J. M., "Optical equivalence ratio sensors for gas turbine combustors", *Proc. Combust. Inst.*, **30**, 1601-1609, 2005.

[15] Akamatsu, F., Wakabayashi, T., Tsushima, S., Mizutani, Y., Ikeda, Y., Kawahara, N. and Nakajima, T., "The development of a light-collecting probe with high spatial resolution applicable to randomly fluctuating combustion fields", *Meas. Sci. Technol.* **10**, 1240–1246, 1999.

[16] Kojima, J., Ikeda, Y. And Nakajima, T., "Basic aspects of OH(A), CH(A), and C_2(d) chemiluminescence in the reaction zone of laminar methane-air premixed flames", *Combust. Flame*, **140**, 34-45, 2006.

[17] Lee, C. L., Oh, C. B. and Kim, J. H., "Numerical and experimental investigations of the NO_x emission characteristics of CH_4-air co-flow jet flames", Fuel, 83, 2323-2334, 2004.

[18] Jeong, Y. K., Jeon, C. H. and Chang, Y. J., "Evaluation of the equivalence ratio of the reacting mixture using intensity ratio of chemiluminescence in laminar partially premixed CH_4-air flames", *Experimental Thermal and Fluid Science.* **30**: 663-673, 2006.

[19] Chou, T. and Patterson, D. J., "In-cylinder measurement of mixture maldistribution in a L-head engine", *Combustion and Flame.* **101**(1-2): 45-57, 1995.

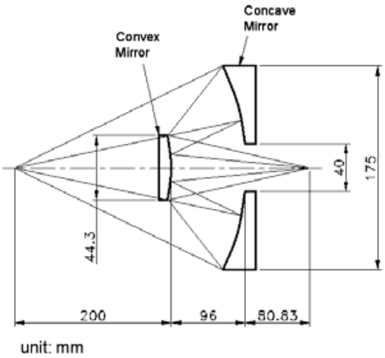

Fig. 1. Schematic diagram of the Cassegrain optics.

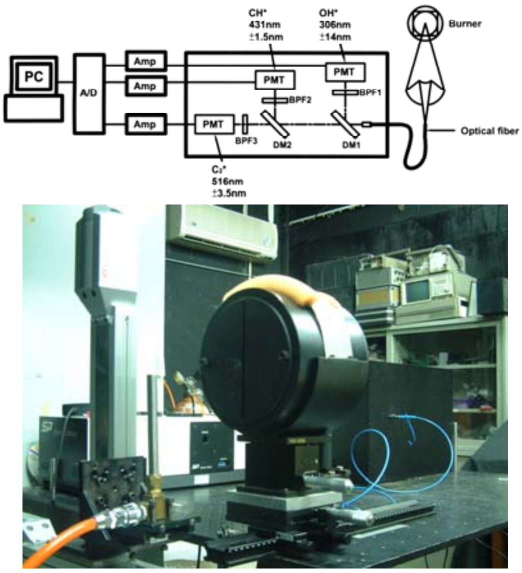

Fig. 2. Schematic diagram and photograph of the measurement system.

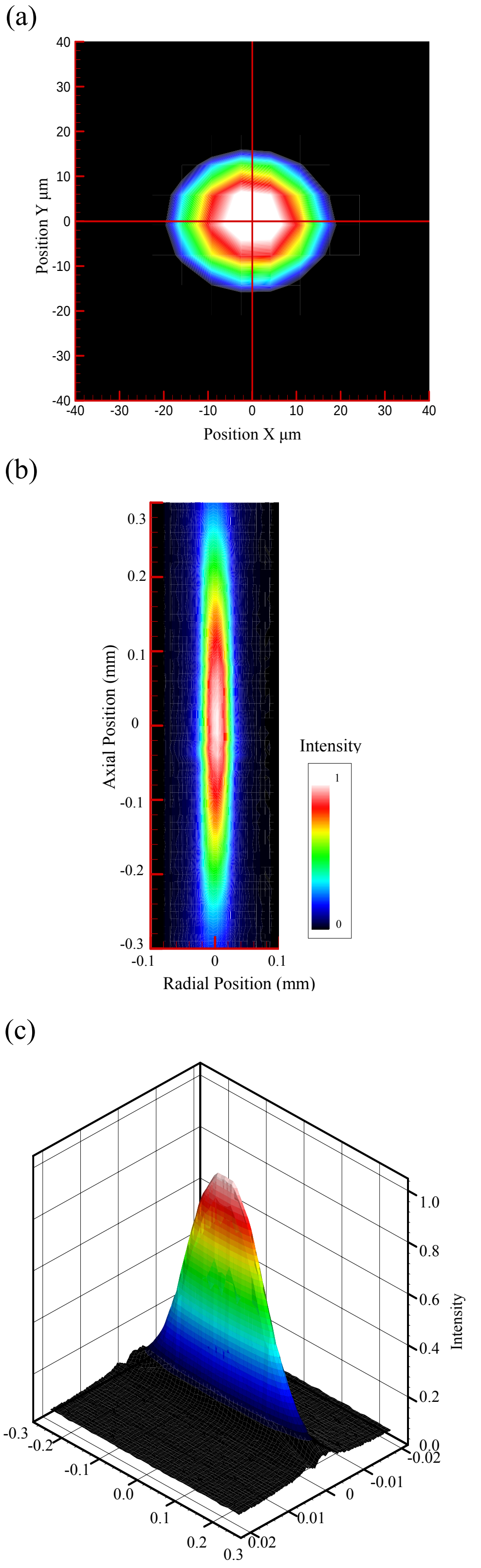

Fig. 3. The light-collection-rate distribution around the probe volume. (a) at the focal point, (b) 2-D distribution, and (c) 3-D profile.

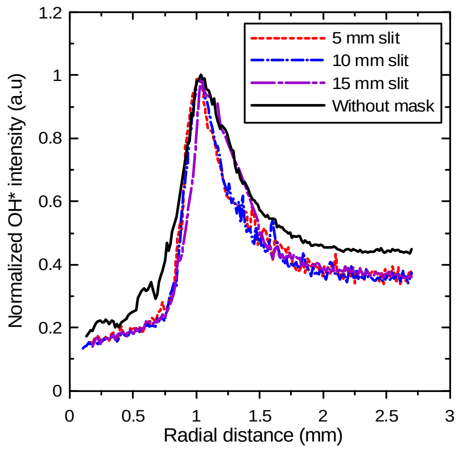

Fig. 4. Effect of the different slit widths of the eye mask on the OH* chemiluminescence intensity profiles (premixed CH_4-air jet flame, $\phi = 1.36$).

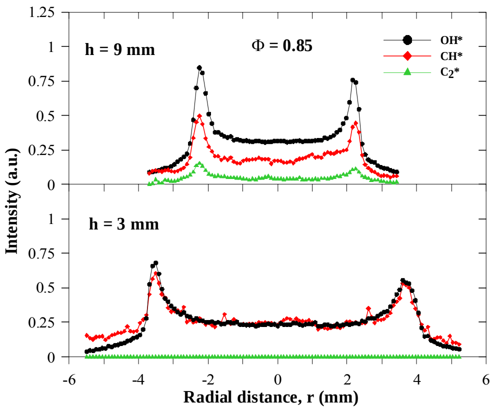

Fig. 5. Radial distribution of the OH*, CH*, and C_2* chemiluminescence intensities at h = 3 and 9 mm for $\phi = 0.85$ flame.

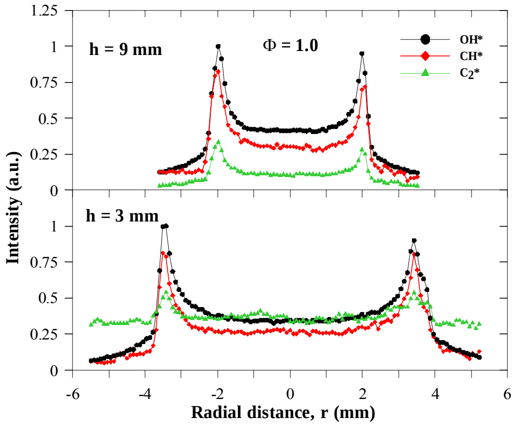

Fig. 6. Radial distribution of the OH*, CH*, and C_2* chemiluminescence intensities at h = 3 and 9 mm for $\phi = 1.0$ flame.

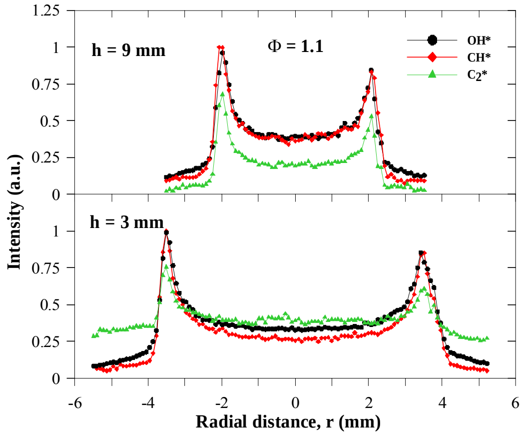

Fig. 7. Radial distribution of the OH*, CH*, and C_2* chemiluminescence intensities at h = 3 and 9 mm for ϕ = 1.1 flame.

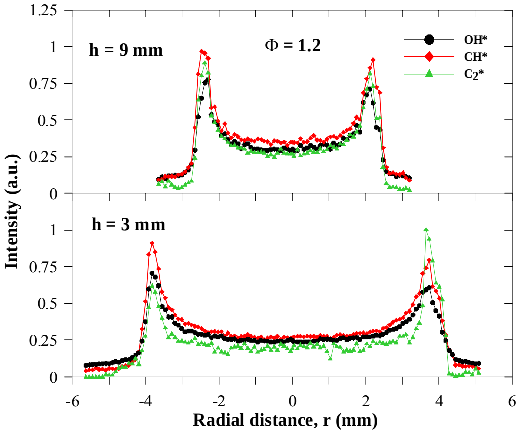

Fig. 8. Radial distribution of the OH*, CH*, and C2* chemiluminescence intensities at h = 3 and 9 mm for ϕ = 1.2 flame.

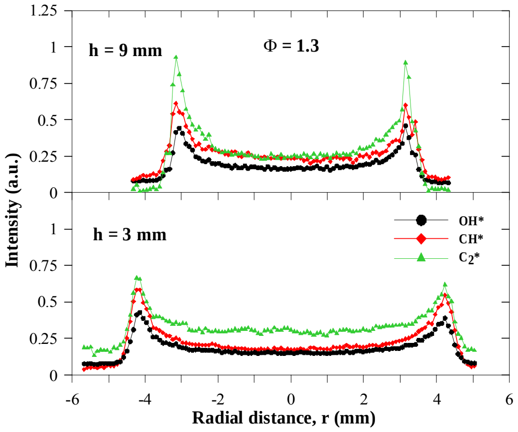

Fig. 9. Radial distribution of the OH*, CH*, and C_2* chemiluminescence intensities at h = 3 and 9 mm for ϕ = 1.3 flame.

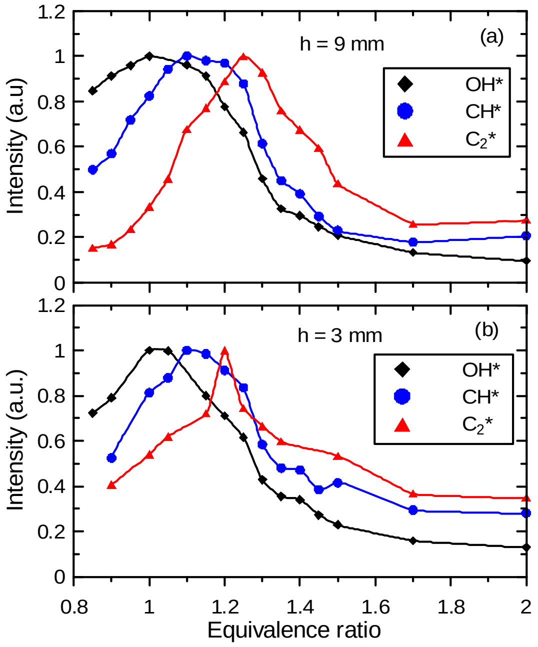

Fig. 10. Variations of the maximum chemiluminescence intensities with the equivalence ratio at h = 3 and 9 mm.

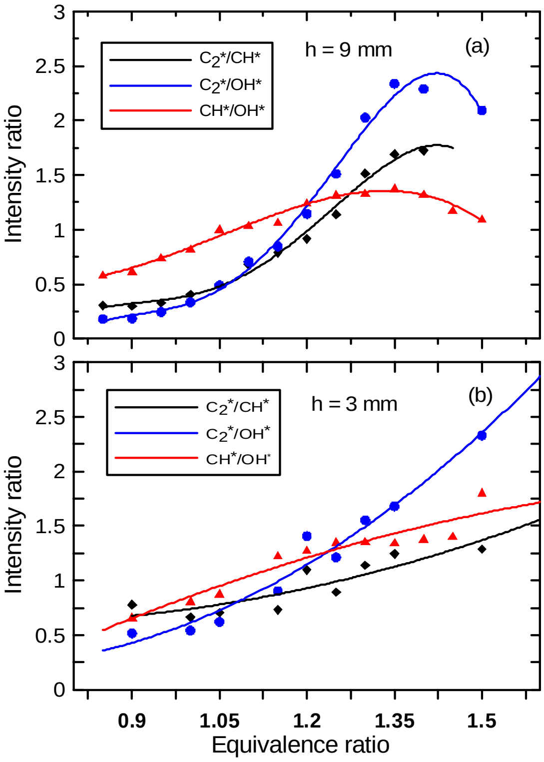

Fig. 11. Correlation of the intensity ratios of C2*/CH*, C2*/OH* and CH*/OH* to the equivalence ratios at h = 3 and 9 mm.

行政院國家科學委員會補助國內專家學者出席國際學術會議報告

97 年 8 月 15 日

附件三

報告人姓名	鄭藏勝	服務機構及職稱	中華大學機械系暨機航所 教授
會議 時間 地點	97.8.3~97.8.8 德國、海德堡	本會核定補助文號	NSC 95-2221-E-216-018-MY2
會議名稱	(中文)第 32 屆國際燃燒會議 (英文)Thirty-Second International Symposium on Combustion		
發表論文題目	(中文)1.兩平行預混甲烷火焰貧油燃燒交互作用之廣泛研究 2.紊流甲烷/一氧化碳噴流火焰熄滅現象之研究 (英文)1. A comprehensive study of two interactive parallel premixed methane flames on lean combustion 2. A study of blowout phenomena of turbulent CH_4/CO jet flames		

報告內容應包括下列各項：

一、參加會議經過

二、與會心得

三、考察參觀活動(無是項活動者省略)

四、建議

五、攜回資料名稱及內容

六、其他

表 Y04

一、參加會議經過

本人於八月二日午夜搭乘長榮航空公司班機啟程直飛加拿大溫哥華並轉機至蒙特婁後，再搭車到會議地點 McGill 大學參加第 32 屆國際燃燒會議，此次前往蒙特婁參與會議的人員尚有成功大學航太系趙怡欽教授及其博士生李約亨、林河川、連永生、碩士生利鴻源，中央大學施聖洋教授，台灣大學潘國隆助理教授，以及北台灣科技學院黃俊賢助理教授等共九人，陣容可謂龐大。八月三日上午八點抵達蒙特婁之後前往會議地點 McGill 大學學生宿舍辦理住宿登記。八月三日下午五點與趙怡欽教授及其研究生等人到 McGill 大學會議中心辦理報到手續之後，並參加主辦單位所舉辦之歡迎酒會，在酒會中遇到燃燒總會前任主席普林斯頓大學的 Prof. C. K. Law，加州大學柏克萊機械系的陳志源(J.-Y. Chen)教授，Stanford 大學的 Professor Ron Hanson，漢城國立大學的鄭仁碩及鄭時浩教授，加州大學爾灣分校的 Professor Derek Dunn-Rankin，美國 Sandia 國家實驗室的 Dr. Rob Barlow，上海理工大學的陳永辰教授及本人的恩師 Prof. Bob Pitz 等人。八月四日起至八月八日連續五天論文發表及海報張貼，這次會議約有 1000 多位來自 30 多個不同國家的學者專家參與，大部份來自美國、日本、法國、德國及其他歐洲國家。

此次會議每天安排七個不同主題同時進行論文宣讀，主題及進行時程如下:

Monday	Hottel Lecture: Multiscale combustion and turbulence, Norbert Peters						
morning	Gas turbine combustion	Turbulent non-premixed jet flames	Laminar flame speeds	Detonations	New technology concepts	Fire suppression	Particulates
afternoon	Topical review & IC engines	Turbulent flames-DNS & LES	Premixed laminar flames	Elementary reactions	Micro-combustors	Radiation effects	Furnaces
	Break						
	Soot formation	Turbulent flames-Tabulated chemistry	Micro-combustors	Small hydrocarbons	Supersonic combustion	Flame chemistry/ Diagnostic studies	Stationary combustion systems
Accepted poster presentations							
Tuesday	Plenary Lecture: From elementary reactions to evaluated chemical mechanisms for combustion models, Michael J. Pilling						
morning	Real fuels	Peroxy radical reactions	Turbulent Non-premixed flames	Soot-temperature effects	Coal	Fire in the environment	New technology concepts
	Break						
	Spherical/ Tubular flames	Peroxy radical reactions	Catalytic micro-combustors	HCCI	Coal	Flame spread	Explosions
afternoon	Topic review and soot	Modeling	Turbulent flames	HCCI	Oxygenates and Biodiesel	Coal/Char	Shocks/ Scramjets/ Explosions
	Break						
	Soot studies	Transport effects	Mild/Oxy-fuel combustion	Engines-other topics	NO	Metal oxides	Ignition
Accepted poster presentations							
Wednesday	Plenary Lecture: Science based policy for addressing energy and environment problems, Robert F. Sawyer						
morning	Micro-combustors	Turbulent flames-modeling	Edge flames	Diesel engine combustion	Chlorine	Soot modeling & Experiments	Fire
	Break						
	Topical review &	Turbulent flames	Methane combustion	Diesel engine combustion	Elementary reactions	Soot chemistry	Fire

	polymers					studies	
Thursday	Plenary Lecture: Flame dynamics, Moshe Matalon						
morning	Rotating burners	Turbulent flames	Micro-combustors	Dynamic mechanism reduction	Diamond films	Soot morphology	Droplet combustion & hydrothermal reaction
	Break						
	Diagnostics	Turbulent premixed & partially premixed flame	Chemistry studies	Mechanisms reduction	Aluminum combustion	Soot modeling & Experiments	Droplet combustion
afternoon	Topical Review & Diagnostics	Thermo-acoustic-diffusion studies	Turbulent premixed flames	Ignition	Aluminum propellants	Soot chemistry studies	Spray & droplet combustion
	Break						
	New technology concepts	Transfer function	Turbulent stratified flames	Ignition	N/C interaction	Soot studies	Counterflow spray combustion
Work-in-Progress Presentations							
Friday	Plenary Lecture: Detonation in gases, E. Shepherd						
morning	Turbulent premixed & partially premixed flame	Diagnostics	Flame vortex interactions	Iron	Ignition	New technology concepts	Spray combustion
	Break						
	Turbulent premixed flame	Diagnostics	Ignition & extinction	Heterogeneous /homogenous combustion	Fuels-kinetic modeling	Spark ignition engines	Spray combustion-DNS & modeling
Afternoon	Flame studies	Diagnostics-CARS	Turbulent flames	Heterogeneous studies	Laminar premixed flame studies	Swirling flames	Spray combustion-LES & modeling
	Break						
	Laser-induced phenomena	Diagnostics-Diode laser	Turbulent premixed flames	Biomass	Pyrolysis	H_2/CH_4 blends	Plasma-aided combustion
Work-in-Progress presentations							

由本人與成大航太所趙怡欽老師及其研究生共同發表之論文分別被安排在第三天(八月六日)上午由博士候選人林河川口頭報告及第五天(八月八日)下午以海報展示方式進行，題目分別是兩平行預混甲烷火焰貧油燃燒交互作用之廣泛研究(A comprehensive study of two interactive parallel premixed methane flames on lean combustion)及紊流甲烷/一氧化碳噴流火焰熄滅現象之研究(A study of blowout phenomena of turbulent CH_4/CO jet flames)。兩篇論文發表時皆獲得很多位與會學者專家的興趣。由於國際燃燒會議出版的論文集(Proceedings of the Combustion Institute)在 2006 年時被 ISI 取消而沒列入 SCI 期刊等級，以致於今年的研討會投稿件數大降，本人也是因為這原因而沒有再撰寫文投稿。在國際燃燒學會於 2007 年聘請律師對 ISI 提出告訴之後，ISI 決定將國際燃燒會議出版的論文集恢復列入 SCI 期刊等級，而此論文集之 2007 年 Impact Factor 則為 2.647，此 Impact Factor 高於燃燒著名期刊 Combustion and Flame 之 Impact Factor，由此可見國際燃燒會議所出版之論文集的重要性，相信在經過此事件之後，下一屆之研討會將會有更踴躍的投稿件數。

二、 與會心得

這次會議是由 McGill 大學負責主辦，由於 McGill 大學的大型會議室較分散，從這個 Session 結束要到下一個 Session 聽報告需要花較多的時間，同時海報展示之張貼會場離主會場也較遠，因此聽到不少抱怨聲。同時由這次會議讓我覺得從事燃燒實驗或是數值模擬研究已走向合作研究的方向，尤其是光學量測燃燒流場的研究更非合作不可，昂貴儀器設備的購買與維護已不再是每個研究單位都可負擔，共同合作一起發表論文才能提升我們的學術國際聲望。

三、考察參觀活動

無

四、建議

感謝國科會對出席國際研討會的補助，希望國科會能繼續補助國內學者參加國際燃燒相關會議，期盼有朝一日我們亦能在台灣舉辦此類會議。

五、攜回資料名稱及內容

此次會議所攜回的資料是與會者通訊錄及海報摘要各一本。

Available online at www.sciencedirect.com
ScienceDirect
Proceedings of the Combustion Institute xxx (2009) xxx–xxx
Proceedings of the Combustion Institute
www.elsevier.com/locate/proci

A comprehensive study of two interactive parallel premixed methane flames on lean combustion

Ho-Chuan Lin[a], Tsarng-Sheng Cheng[b], Bi-Chian Chen[a], Chun-Chin Ho[a], Yei -Chin Chao[a,*]

[a] *Institute of Aeronautics and Astronautics, National Cheng Kung University, Tainan 701, Taiwan, ROC*
[b] *Department of Mechanical Engineering, Chung Hua University, Hsinchu 300, Taiwan, ROC*

Abstract

This study aims to investigate interactive parallel lean premixed methane flames issued from twin rectangular slot burners with variable jet spacing, equivalence ratios and inlet speeds. The flowfield and combustion chemical reactions are predicted by detailed numerical simulation with Skeletal and GRI-v3.0 mechanisms. Numerical results such as velocity streamlines, temperature, flame height and flame shape are validated with those obtained by experimental particle image velocimetry (PIV) and flame measurements. When moved closer beyond a threshold jet spacing, these twin flames become interactive and both flames tilt outward in appearance with a wider operational range of lean and velocity conditions. Numerical predictions of flowfields found that there are three different interacting stages: entrainment, recirculation and reverse flows according to jet-to-jet spacing and they are named by their characteristic postflame flowfields between jet burners. At the reverse flow stage, a stagnating flowfield termed lateral impingement is generated along the symmetric axis between the flames, which is similar but not identical to that found in the counter-flow flames. As the jet spacing is reduced, the flowfield transition of the interacting postflame stages is believed to be the main mechanism to enhance the flame stabilization, especially in lean conditions. This reverse flow pattern provides a hot and slow postflame flowfield and transports the residual OH radicals from the main flames to heat and burn the fuel escaping from the stand-off gap between the flame base and burner rim through low temperature burning process. In other words, the stabilization of the interactive twin flames is enhanced by a number of crucial factors such as lateral stagnating flow, low dissipation of thermal and interacting chemical species supplied from the main flames.

Keywords: Lean combustion; Lateral impingement; Stagnating flow and interactive flames

---

1. Introduction

Lean combustion is generally considered as a timely solution to the more stringent environmental regulations and global weather concerns in a new era. However, the instability associated with the lean flame significantly keeps the lean combustion technique from being widely accepted as a major combustion technique for general applications. The past studies indicate some methods to improve the combustion instability such as vortex [1], swirling, interacting side-by-side diffusion burner array or matrix [2], hydrogen addition [3,4]

---

[*] Corresponding author. Fax: +886 6 238 9940.
E-mail address: ycchao@mail.ncku.edu.tw (Y.-C. Chao).

1540-7489/$ - see front matter © 2009 The Combustion Institute. Published by Elsevier Inc. All rights reserved.
doi:10.1016/j.proci.2008.07.030

Please cite this article in press as: H.-C. Lin et al., *Proc. Combust. Inst.* (2009), doi:10.1016/j.proci.2008.07.030

and reactor temperature oscillation [5]. The first two combustion techniques improve the flame instability by means of flow oscillation resonance and transverse wash of swirling flow to the adjacent flames respectively. The swirling flow is a typical flowfield for gas turbines but it is not common for other applications and the flame oscillation is likely limited to a specific situation. The third one uses side-by-side jet array to create an interactive hydrodynamic effect to generate vortex or flow recirculation between the jets and broaden the blow-out limits. However, the difficulty of oxygen supply does create a limit to bring these two diffusion flames in an even shorter jet spacing so the enhancement of extending blowout limit is not as good as expected. Therefore this method works very well only to certain jet spacing as reported. The fourth method attracts more attention recently because it also improves the NO_x emission. Nevertheless, the cost of hydrogen is quite high. From the preceding reviews, this study suggests the side-by-side jet array as a reasonable solution to the stability problem associated with lean premixed flames.

Jet flame arrays impinging upon a surface were widely reported by the researchers [6–8]. Their focuses are on the heat transfer coefficients of the span-wise stream and the impingement surface as well as the heat transfer rate of flowfield velocity, turbulence and convection. Recently research papers [9–15] addressed the effects of jet-to-jet spacing and nozzle-to-plate distance on the heat transfer of jet flame arrays impinging upon a surface, which is not the concern of this paper though, but they did notice the tilted flame shape caused by a positive pressure gradient at the interacting site. However, this positive pressure gradient was not appreciated and discussed further owing to different research objectives of these studies. For burner arrays, Kimura and Ukawa [16] and Singer [17] revealed the combustion characteristics of the two-dimensional rectangular burner. Menon and Gollahali [18,19] studied the interaction of multiple jet flames in still air and crossflow. Roper [20] reported the interactions of two laminar jet diffusion flames. Recently, Seigo et al. [21] studied the flame characteristics of low load rich-lean burner. Most of the research mentioned above emphasized on the interactions of the jet diffusion flames but scant attention is paid to the flame structure, operation characteristics and stabilization mechanism of the interactive premixed flames on lean combustion. Thus, such interactive features deserve further studies.

On top of the previous studies [22,23] on stability limits of interactive flames, the present study intends to explore the detailed flame structure and stabilization mechanism of interactive twin jet flames, based on the measurements of flow and thermal field and detailed numerical simulation of flame speed, heat release rate and chemical reactions on lean combustion conditions. To simplify the interactive premixed flames for numerical and experimental studies we used two 50 mm × 5 mm rectangular slot burners to investigate the effects of the jet-to-jet spacing, inlet speed and equivalence ratio between the two burners.

2. Experimental setup

The experimental apparatus is shown in Fig. 1. The aluminum slot burner is 160 mm in height with rectangular exit made of 1 mm thick wall and opened to an inside cross-sectional dimension of 5 mm (called "d") by 50 mm. Both stainless steel meshes and ceramic rectifiers were used to straighten the flowfield. The flow in the vicinity of the burner exit was a fully developed velocity profile verified by particle image velocimetry (PIV) measurement. There was no inert gas sheath flow around the burners. Methane and air metered by electronic flow meters were premixed and guided into a manifold where the mixture was divided equally to two jets. Twin flames set in dimensionless jet spacing $L/d = 2 \sim 6$ were investigated in mean inlet flow velocities ranging from 0.7 to 3 m/s and equivalence ratio ϕ was in the range of 0.55–1.38. The temperature distributions were measured by thermocouples, and the global flame appearance was captured by a digital CCD camera. The flowfield of the interactive flames was carefully examined by using PIV technique.

Figure 1 shows the current PIV experimental setup for flow and postflame field velocity measurements. This PIV digital camera was equipped with a mechanical shutter to prevent the PIV image from flame-illumination contamination. The measurement system was made up of two Nd: YAG lasers, a digital CCD camera, a pulse generator, a mechanical shutter and a controller. This laser system possessed two Q-switched Nd: YAG pulse lasers (LOTIS TII) lasing at the fundamental wavelength (1064 nm) and second harmonic (532 nm). The wavelength of 532 nm was utilized for whole-field illumination and the maximum pulse energy was 170 mJ. A high-resolution and high-performance digital CCD camera (**sharpVISION**™) was used. Each image contained 1024 × 1280 pixels, which rendered a spatial resolution of 6.7 μm/pixel in the setup. The interframe time for double-shutter mode could go as low as 200 ns.

3. Numerical method

To numerically simulate the laminar premixed methane twin flames, the relevant governing equations were solved by using the commercial package ESI-CFD for flow, heat transfer and chemistry/mixing computations. A flame-zone

Please cite this article in press as: H.-C. Lin et al., *Proc. Combust. Inst.* (2009), doi:10.1016/j.proci.2008.07.030

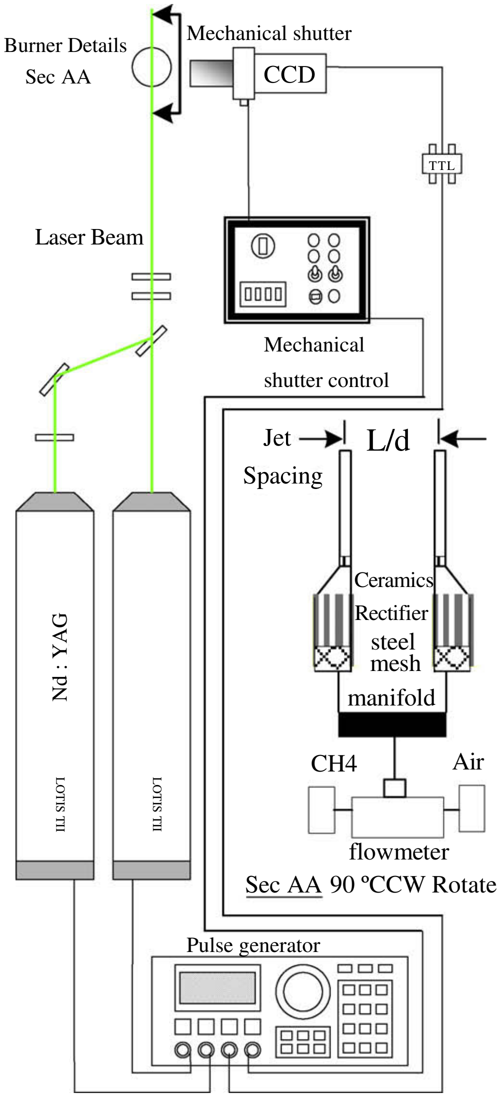

Fig. 1. Experimental apparatus.

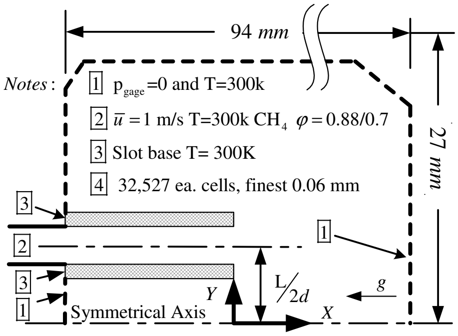

Fig. 2. Illustration of CFD computational domain and boundary conditions.

reinforced grid system was used to solve the discretized equations with a control volume formulation in accordance with the SIMPLEC algorithm as shown in Fig. 2. The inlet and boundary conditions are shown in Fig. 2. The surrounding boundary condition marked with was set as gage static pressure $p = 0$, temperature of 300 k and chemical mixture of pure air in case of flow-into-system situation. The burner inlet marked was set as a uniform velocity profile of 1 m/s, temperature of 300 k and contained methane–air mixture of equivalence ratio of 0.88 or 0.7. The burner end surface marked with was set as constant temperature of 300 k. The rest portion of the burner located inside the computational domain was conjugated into the whole calculation with material specification of aluminum alloy with density of 2700 kg/m^3, specific heat of 880 J/kg k and thermal conductivity of 190 W/m k but the wall effect model was not specified. Symmetric condition was applied at the symmetric axis in the lower boundary of the Fig. 2. All of the governing equations were solved by using the second-order scheme except the velocity equation handled by second-order plus 50% upwind scheme. Input of the molecular transport data was obtained from the CHEMKIN Rev. 3.0 package. In order to save the computational time, we started with Skeletal mechanism and followed by GRI Rev. 3.0 package for preliminary and detailed calculations respectively. The radiation effect had not been embodied into current numerical calculation due to the limited contribution.

4. Results and discussion

4.1. Flame configuration versus equivalence ratio and inlet speed

Figure 3 shows 13 pairs of interactive flames side-by-side with jet-to-jet spacing $L/d = 2$ burning at equivalence ratio of 0.55, 0.6, 0.65, 0.7, 0.75, 0.8, 0.88, 0.98, 1.06, 1.14, 1.2, 1.28, and 1.38 respectively from left to right. As shown in middle part of Fig. 3 each pair of flames expels each other and looks like an “M-shape” flame on the mild lean area. They form a conical or up-side-down “U-shape” flame [1] as equivalence ratio goes richer than 1.4 and the inboard rim flames are lifted off. The “V-shape” flame consists of two half lift-off flames anchored on inboard side of each burner only on the extremely lean combustion. Figure 3 also shows that the $L/d = 2$ burners can sustain a flame even when the equivalence ratio goes lower than 0.55, lower than the ordinary flammability limit. As illustrated in Fig. 4 the flame offset angle is defined by the ratio of the offset distance of flame tip from jet central axis to the flame height. The offset angle becomes

Please cite this article in press as: H.-C. Lin et al., Proc. Combust. Inst. (2009), doi:10.1016/j.proci.2008.07.030

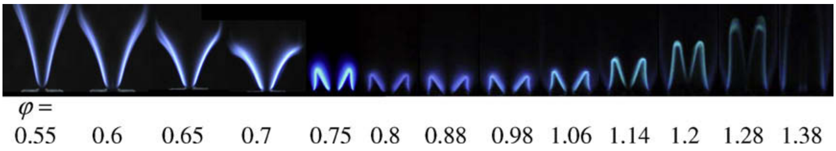

Fig. 3. Flame configurations vs. equivalence ratios.

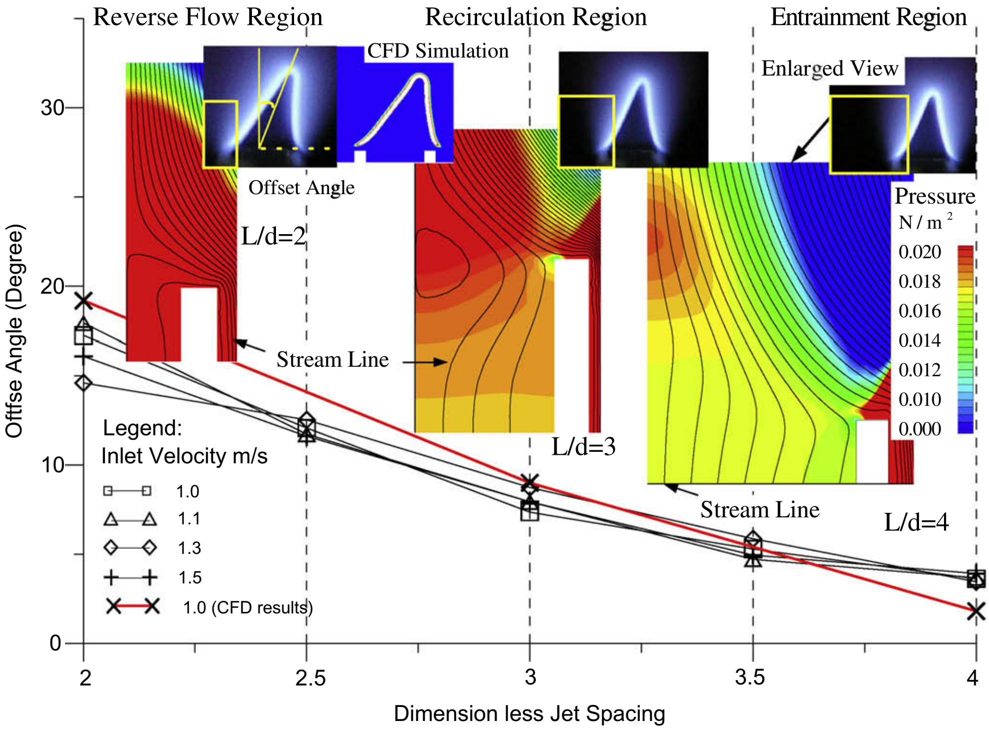

Fig. 4. Effects of jet-to-jet spacing on flame and flowfield characteristics.

larger or the flame tilts outward more as the burners approach each other from jet spacing of $L/d = 4$, 3.5, 3, 2.5 and all the way down to 2. Figure 4 shows that there is no apparent change to the offset angle accompanied with the variation of inlet speed from 1.0 to 1.5 m/s. The only difference is the flame height getting taller along increasing of the inlet speed.

4.2. Validation and deviation of computational results

To look further into this premixed twin flame interaction, interested cases were numerically simulated and their calculated pressure distributions and stream lines were presented in Fig. 4 for $L/d = 2$, 3 and 4. Because of the symmetrical nature of twin flames it is practical to just show one flame image out of the twin interactive flames in Fig. 4. To validate the computational flame shape with the experimental one, a drawing of the simulated flame heat release rate was placed side-by-side to the photographic image of the real flame operated at an identical condition on the left top corner of Fig. 4. It is very promising of this comparison in terms of the flame shape and the offset angle between these two pictures. However the highest flame temperature of CFD calculation is 2080 K, much higher than the experimental measurement of 1800 K for the $L/d = 2$ case. And the predicted flame height by numerical simulation is only 0.3 mm shorter than the photo flame.

4.3. Entrainment, recirculation and reverse flows

The flowfields near the inboard gap were numerically investigated and the flame base areas circled with yellow frames were carefully trimmed and enlarged in Fig. 4. As noted, the computed postflame streamline patterns changed when the jet spacing was reduced. The variation of the flow pattern in the inboard gap is believed to be

Please cite this article in press as: H.-C. Lin et al., *Proc. Combust. Inst.* (2009), doi:10.1016/j.proci.2008.07.030

strongly related with the enhancement of the inboard flame stabilization, especially for lean conditions. Along the decrease of jet spacing from $L/d = 4$–2, the flowfield near the inboard gap changed from entrainment flow for $L/d = 4$, recirculation flow for $L/d = 3$, and finally up to an "impingement" reverse flow for $L/d = 2$. The "impingement" reverse flow depicts a characteristic stagnating flow. The postflame flowfield for the $L/d = 4$ flame has a streamline pattern as straightforward as that of an ordinary postflame flow entraining the ambient air into the symmetric axis except a less pronounced local pressure peak outstanding from the yellow background. This local pressure peak is due to the limited space in this minor impinging area. For the case of $L/d = 3$, a local recirculation region of entrained flow at the symmetric axis is formed and the pressure peak at the symmetric axis becomes pronounced, pushing the flame outward more. When the jet spacing is $L/d = 2$, the postflame streamlines impinge each other severely and a reverse flow is generated, creating a flame and a flowfield structure similar to those found in the counter-flow flame. At this case entrainment of ambient air is completely blocked.

4.4. Flame stabilization and lateral impingement

The counter-flow can also create a hydrodynamic effect to enhance the flame stabilization. It [24] reported that a counter-flow flame can burn methane–air mixture with an equivalence ratio as lean as of 0.45. Figure 5 shows the lateral impingement demonstrated by overlapping streamlines and PIV uniform vectors in the background of the X_{OH} (left two pictures) and X_{CO} (right one) mole concentration. The three blank rectangular areas represent the left three burner rims of the twin jet burners at the jet spacing of $L/d = 2$. The origin of x-axis is located just right on the symmetrical line and that of y-axis is lined up with the tip of the rim. It also shows the calculated streamlines and the first three streamlines designated as IB-1, IB-2 and IB-3 for inboard rim and OB-1, OB-2 and OB-3 for outboard one respectively.

This impingement area has an obvious stagnation point and the computed streamlines were carefully verified by the PIV measurement as denoted in uniform velocity vectors (show only the direction) in the middle picture of Fig. 5. This effect can be designated as a lateral or an angled counter-flow and classified as a typical stagnation-flow flame. The differences between the inboard and outboard regions in the flowfield pattern significantly affect the characteristics of the flame and the reaction near the burner rim as depicted by the color-coded OH and CO concentration distributions in Fig. 5. The characteristics of the thermal and the flame near the burner rim will directly influence the flame stabilization. The inboard side has a taper-down flow velocity and taper-up static pressure flowfield as shown in Fig. 6 and the flow velocity needs to be reduced to around zero at the impinged point within a relatively short distance. Therefore in Fig. 6 the velocity magnitude of the entire inboard side is reduced while that of the outboard side is accelerated. The temperature along the streamlines IB-2 and IB-3 goes up between the streamline coordinate of 2 and 3 mm in the postflame of the gap region. These characteristics of the reduced velocity and the increasing temperature in the postflame provide extended residence time and richer chemical species, which in turn favor the combustion process in this region.

4.5. Calculated wall proximity effect of HO_2, H_2O_2

In addition to the flame stabilization discussed above, the calculated near-wall behaviors of the HO_2 and $H_2O_2$and their contributions to the flame stabilization near the inboard burner rim are illustrated in Fig. 7, called the wall proximity

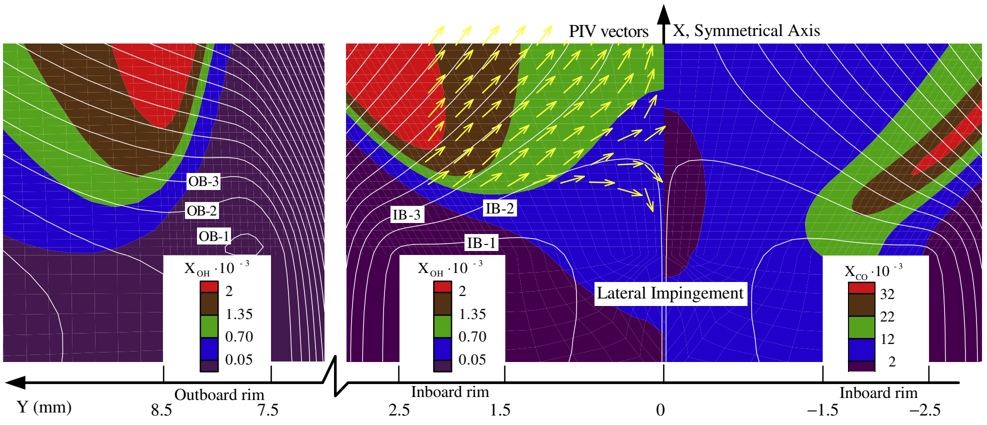

Fig. 5. Lateral impingement demonstrated by stream lines with OH and CO mole concentration background.

Please cite this article in press as: H.-C. Lin et al., *Proc. Combust. Inst.* (2009), doi:10.1016/j.proci.2008.07.030

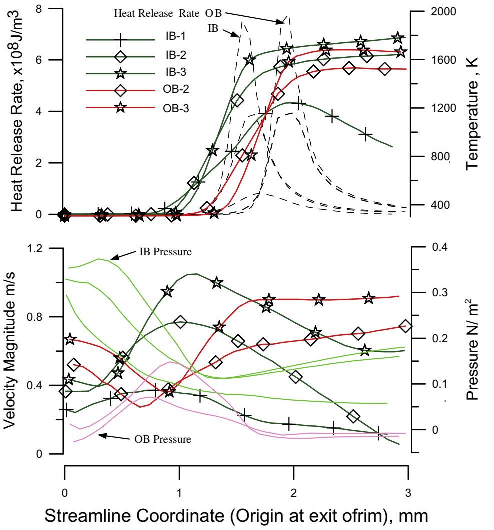

Fig. 6. Physical stabilization mechanisms by flow and thermal field along stream lines.

effect. The near-wall effect and low temperature reaction mechanism become important in the wall proximity region between the burners. Figure 7 indicates that the HO_2 concentration isopleth fades from level 5 of the main flame (left-upper corner of the picture) down to level 4 near the streamline IB-2 but rises back up to level 5 near the rim wall. In the meantime it is found that a pool of H_2O_2 builds up thicker and thicker between the streamline IB-1 and the rim wall of the burner. This H_2O_2 pool is generated by the promoted reaction of $2HO_2 \rightarrow O_2 + H_2O_2$ when HO_2 concentration becomes higher in the low temperature background near the rim. The H_2O_2 pool here works like storage of HO_2 as well as a more effective form for optimizing the HO_2 gathering effect. The OH concentration in one spot of the IB-1 streamline is rich enough to support the reaction of $OH + CH_4 \rightarrow CH_3 + H_2O$ because of the additional supply from stored HO_2 and H_2O_2 through the reactions of $H + HO_2 \rightarrow 2OH$ and $H + H_2O_2 \rightarrow H_2O +$ OH. As shown in Fig. 5, the surplus of inboard OH mole fraction is extended deeply into the gap of the two burners along the reverse flow, which implies a high temperature zone with active chemical species does exist between the two flames and provides an environment to stabilize the flame. As observed, the weighting of heat release contribution shifts from reaction of $OH + CH_4 \rightarrow CH_3 + H_2O$ to $HO_2 + CH_3 \rightarrow OH + CH_3O$ in the jet-to-jet gap area. This inboard wall proximity effect also helps many other chemical species as long as they can form an effective proximity area or a closed angle shape by the rim tip and the main flame concentration band. In this work those species are CH_3O, CH_3OH, C_2H_2, C_2H_4, C_2H_6, C_3H_8, CH_2O, H_2 and CO. As noted, the OH radical is not in the list above so the mole fraction of OH is reduced near the burner rim area since there is no wall proximity effect for OH. Fortunately this reduction of OH concentration fills up by the stored $HO_2$and H_2O_2. After all, the discussion mentioned above is based on the calculation findings which were physically validated with the temperature measured by thermal couple, the pictures of the flame shape and the flow fields of PIV measurement. In other words, all of the chemicals with wall proximity effect could have certain deviation in respect to quantitative aspect.

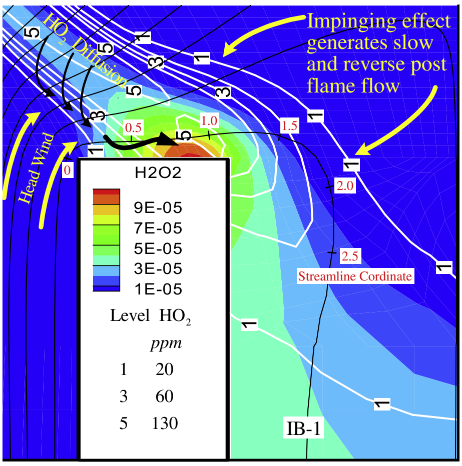

Fig. 7. Chemical aspect of wall proximity effect of HO_2 and H_2O_2.

In summary of the stabilization mechanism of the twin interactive flames, a schematic drawing compared the inboard and outboard flame stabilization was presented in Fig. 8 at the jet spacing of 2d and the reverse flow stage. At the reverse flow stage, a stagnating flowfield, termed lateral impingement, is generated along the symmetric axis between the flames, similar to that found in the opposed counter flames but the temperature is cooler than that of the vertical opposed jets. The transition of the postflame flowfield, at the short jet spacing scenario, is believed to be the main mechanism to enhance the flame stabilization, especially in lean conditions. By regulating the amount of entrainment flow, this lateral impingement flowfield provides a zone with low dissipation of both the heat and the chemical species in this area, which would favor the flame stabilization. The wall proximity effect also turns HO_2 into H_2O_2 to accommodate more incoming HO_2 leading to additional OH supply for the combustion. The OH radicals are diffused and transported by the reverse flow into the impinging area and react with the escaping fuel to generate the additional heat in the gap region. It dramatically helps the flame base to be stabilized near

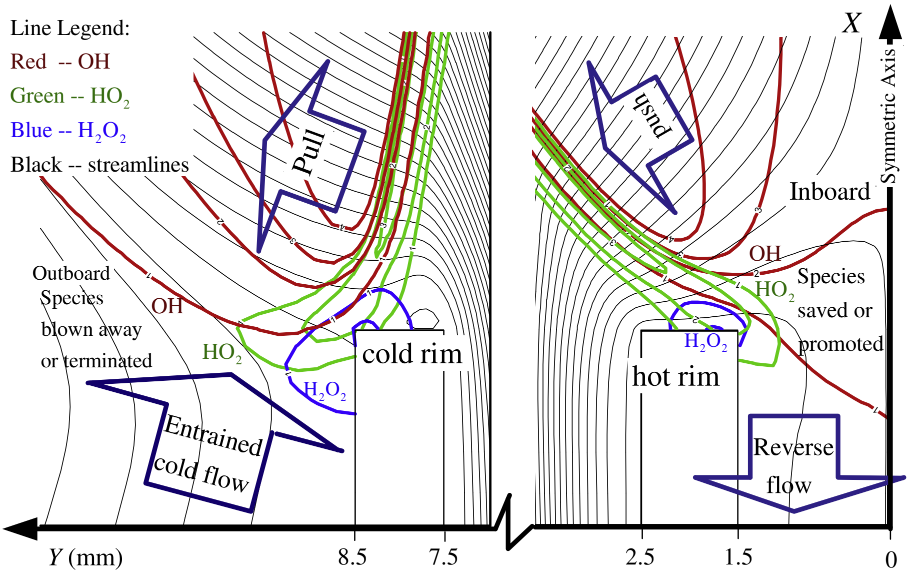

Fig. 8. Schematic comparison of the differences between inboard and outboard sides in respect of (1) heating or cooling burner rims, (2) cold entrained or hot reverse flows, and (3) blown away/cooling down or saved/promoted for chemical species.

the burner rim with the additional supply of OH, especially for lean combustion. On the contrary, the outboard flame, as shown in Fig. 8, suffers from the quench effect due to the cold entrainment flow which dissipates the heat as well as the active species near the rim tip.

5. Conclusions

This study is intended to look into the entire phenomenon of two lean premixed methane flames placed within interactive jet spacing. The parallel interactive premixed methane flames are identified numerically and experimentally as a phenomenon of lateral impingement of postflames or angled counter-flow flames. These parallel stagnation flames possess a few typical characteristics of counter-flow flames such as the flame stretching and the enhanced flame stabilization observed in this study. Besides, there are some new findings obtained to explain how the impingement flowfield in the gap region between the burners near the burner rim helps the stabilization of the flame in terms of hydrodynamic, thermal and chemical species contributions. This flame stabilization mechanism was comprehensively explained in this study.

References

[1] T. Schuller, D. Durox, S. Candel, *Combust. Flame* 135 (2003) 525–537.

[2] B.-J. Lee, J.-S. Kim, S. Lee, *Combust. Sci. Tech.* 176 (2004) 482–497.

[3] E.R. Hawkes, J.H. Chen, *Combust. Flame* 138 (2004) 242–258.

[4] J.-Y. Ren, F.N. Egolfopoulos, *Combust. Sci. Tech.* 174 (2002) 181–205.

[5] M. De Joannon, P. Sabia, A. Tregrossi, A. Cavaliere, 176 (2004) 769–783.

[6] R.N. Koopman, E.M. Sparrow, *Intl. J. Heat Mass Trans.* 19 (1976) 673–683.

[7] L.F.G. Geers, M.J. Tummers, K. Hanjalic, *Exp. Fluids* 36 (2004) 946–958.

[8] M. Can, A.B. Etemaglu, A. Avci, *Heat Mass Trans.* 38 (2002) 251–259.

[9] L.L. Dong, C.W. Leung, C.S. Cheung, *Intl. J. Heat Mass Trans.* 47 (2004) 489–500.

[10] L.L. Dong, C.W. Leung, C.S. Cheung, *Intl. J. Heat Mass Trans.* 46 (2003) 113–125.

[11] S. Chander, A. Ray, *Intl. J. Heat Mass Trans.* 50 (2007) 640–653.

[12] J. Wu, J. Seyed-Yagoobi, R.H. Page, *Combust. Flame* 125 (2001) 955–964.

[13] J.-Y. San, M.-D. Lai, *Intl. J. Heat Mass Trans.* 44 (2001) 3997–4007.

[14] S. Chander, A. Ray, *Energy Conver. Manage.* 46 (2005) 2803–2837.

[15] S. Chander, A. Ray, *Exp. H. Trans.* 19 (2006) 15–38.

[16] I. Kimura, H. Ukawa, Seventh Symposium (International) Combustion, *Combust. Inst.* (1956) 521–523.

[17] Singer, J.M., Fourth Symposium (International) Combustion, *Combust. Inst.* (1952) 352–358.

[18] R. Menon, S.R. Gollahalli, *ASME*, HTD Publ by ASME, New York,, 1985, pp. 45, 27–133..

[19] R. Menon, S.R. Gollahalli, *Combust. Sci. Tech.* 60 (1988) 375–389.

Please cite this article in press as: H.-C. Lin et al., *Proc. Combust. Inst.* (2009), doi:10.1016/j.proci.2008.07.030

[20] F.G. Roper, *Combust. Flame* 34 (1979) 19–27.

[21] K. Seigo, H. Satoshi, U. Yoshito, M. Syuichi, A. Katsuo, 20th ICDERS, Canada, 2005.

[22] H.-C. Lin, B.-C. Chen, C.-C. Ho, Y.-C. Chao, Asia-Pacific Conference on Combustion, 2007.

[23] H.-C. Lin, B.-C. Chen, C.-C. Ho, Y.-C. Chao, 21st ICDERS, Poitiers, France, July 23–July 27, 2007.

[24] H. Guo, G.J. Smallwood, L. GülderÖ, *Proc. Combust. Inst.* 31 (2007) 1197–1204.

Please cite this article in press as: H.-C. Lin et al., *Proc. Combust. Inst.* (2009), doi:10.1016/j.proci.2008.07.030

A STUDY OF THE BLOWOUT PHENOMENA OF TURBUELNT CH_4/CO JET FLAMES

C. –Y. Wu[1], Y. –C. Chao[1], T. S. Cheng[2], Y. –S. Lien[1], Y. –Y. Cheng[1]

[1] *Department of Aeronautics and Astronautics, National Cheng Kung University, Taiwan ROC;*

[2] *Department of Mechanical Engineering, Chung Hua University, 300, Taiwan ROC*

ycchao@mail.ncku.edu.tw

Abstract

Flame stabilization which generally involves different combustion characteristics of fundamental properties is an important issue of fundamental combustor design. Due to the environmental threats and depletion of fossil fuel, two timely alternatives strategies which are either to improve the combustion efficiency with considerable reductions in the pollutant emissions into the atmosphere or more significantly to replace fossil fuel usage as much as possible with environmentally friendly, clean and renewable energy sources attract researcher's attention recently. Among the renewable energy sources, gasified biomass that contains a mixture of carbon monoxide, hydrogen and methane, together with carbon dioxide and nitrogen, is more versatile and attractive than the original solid biomass. The combustion characteristics of carbon monoxide, which is a major species in gasified biomass fuels, are different from those of hydrogen and other alkane. It has been shown that the addition of small amount of hydrogen or methane to CO flames increases the laminar flame speed and extinction strain rate by accelerating the main CO oxidation reaction. In the present study, the blowout velocities of the CH_4/CO blended fuels are theoretically and experimentally studied through phenomenological observation and the measured results are used to verify the existing theories of blowout. Furthermore, comparison of the measured results with theoretical predictions will be made to delineate the characteristics of blowout phenomena in turbulent jet flames.

The calculated and measured non-dimensional blowout out velocities of CH_4/CO turbulent diffusion flames are shown in Fig. 1. On the other hand, the calculated blowout parameters are shown in Fig. 2. Generally, blowout velocities of turbulent CH_4/CO diffusion jet flames still can be estimated by using universal formula which based on initial gas properties and the initial velocity at jet exit. The theoretically predicted stoichiometric contours of methane and carbon monoxide provide an explanation for the fact that the blowout velocities of turbulent CH_4/CO diffusion jet flames are mainly dominated by methane/air mixing.

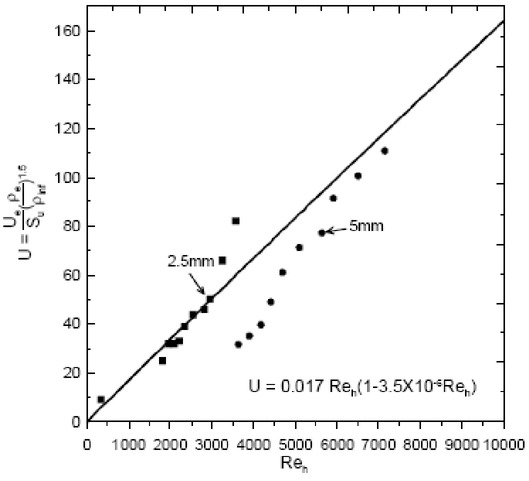

Fig. 1

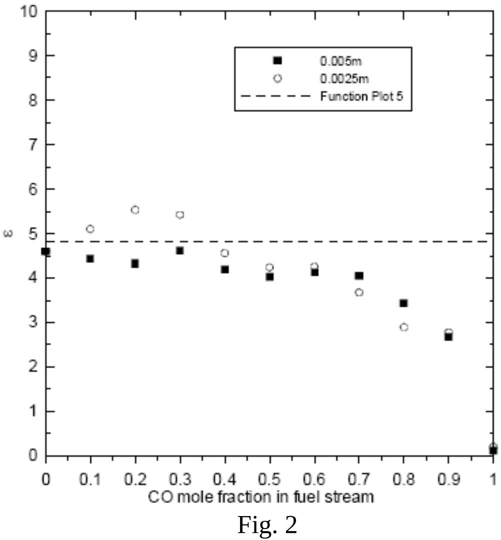

Fig. 2

行政院國家科學委員會補助國內專家學者出席國際學術會議報告

97 年 8 月 15 日

附件三

報告人姓名	鄭藏勝	服務機構及職稱	中華大學機械系暨機航所 教授
會議 時間 會議 地點	97.8.3~97.8.8 德國、海德堡	本會核定補助文號	NSC 95-2221-E-216-018-MY2
會議名稱	(中文)第 32 屆國際燃燒會議 (英文)Thirty-Second International Symposium on Combustion		
發表論文題目	(中文)1.兩平行預混甲烷火焰貧油燃燒交互作用之廣泛研究 2.紊流甲烷/一氧化碳噴流火焰熄滅現象之研究 (英文)1. A comprehensive study of two interactive parallel premixed methane flames on lean combustion 2. A study of blowout phenomena of turbulent CH_4/CO jet flames		

報告內容應包括下列各項：

一、參加會議經過

二、與會心得

三、考察參觀活動(無是項活動者省略)

四、建議

五、攜回資料名稱及內容

六、其他

表 Y04

一、參加會議經過

本人於八月二日午夜搭乘長榮航空公司班機啟程直飛加拿大溫哥華並轉機至蒙特婁後，再搭車到會議地點 McGill 大學參加第 32 屆國際燃燒會議，此次前往蒙特婁參與會議的人員尚有成功大學航太系趙怡欽教授及其博士生李約亨、林河川、連永生、碩士生利鴻源，中央大學施聖洋教授，台灣大學潘國隆助理教授，以及北台灣科技學院黃俊賢助理教授等共九人，陣容可謂龐大。八月三日上午八點抵達蒙特婁之後前往會議地點 McGill 大學學生宿舍辦理住宿登記。八月三日下午五點與趙怡欽教授及其研究生等人到 McGill 大學會議中心辦理報到手續之後，並參加主辦單位所舉辦之歡迎酒會，在酒會中遇到燃燒總會前任主席普林斯頓大學的 Prof. C. K. Law，加州大學柏克萊機械系的陳志源(J.-Y. Chen)教授，Stanford 大學的 Professor Ron Hanson，漢城國立大學的鄭仁碩及鄭時浩教授，加州大學爾灣分校的 Professor Derek Dunn-Rankin，美國 Sandia 國家實驗室的 Dr. Rob Barlow，上海理工大學的陳永辰教授及本人的恩師 Prof. Bob Pitz 等人。八月四日起至八月八日連續五天論文發表及海報張貼，這次會議約有 1000 多位來自 30 多個不同國家的學者專家參與，大部份來自美國、日本、法國、德國及其他歐洲國家。

此次會議每天安排七個不同主題同時進行論文宣讀，主題及進行時程如下:

Monday	Hottel Lecture: Multiscale combustion and turbulence, Norbert Peters						
morning	Gas turbine combustion	Turbulent non-premixed jet flames	Laminar flame speeds	Detonations	New technology concepts	Fire suppression	Particulates
afternoon	Topical review & IC engines	Turbulent flames-DNS & LES	Premixed laminar flames	Elementary reactions	Micro-combustors	Radiation effects	Furnaces
	Break						
	Soot formation	Turbulent flames-Tabulated chemistry	Micro-combustors	Small hydrocarbons	Supersonic combustion	Flame chemistry/ Diagnostic studies	Stationary combustion systems
Accepted poster presentations							
Tuesday	Plenary Lecture: From elementary reactions to evaluated chemical mechanisms for combustion models, Michael J. Pilling						
morning	Real fuels	Peroxy radical reactions	Turbulent Non-premixed flames	Soot-temperature effects	Coal	Fire in the environment	New technology concepts
	Break						
	Spherical/ Tubular flames	Peroxy radical reactions	Catalytic micro-combustors	HCCI	Coal	Flame spread	Explosions
afternoon	Topic review and soot	Modeling	Turbulent flames	HCCI	Oxygenates and Biodiesel	Coal/Char	Shocks/ Scramjets/ Explosions
	Break						
	Soot studies	Transport effects	Mild/Oxy-fuel combustion	Engines-other topics	NO	Metal oxides	Ignition
Accepted poster presentations							
Wednesday	Plenary Lecture: Science based policy for addressing energy and environment problems, Robert F. Sawyer						
morning	Micro-combustors	Turbulent flames-modeling	Edge flames	Diesel engine combustion	Chlorine	Soot modeling & Experiments	Fire
	Break						
	Topical review &	Turbulent flames	Methane combustion	Diesel engine combustion	Elementary reactions	Soot chemistry	Fire

	polymers					studies	
Thursday	Plenary Lecture: Flame dynamics, Moshe Matalon						
morning	Rotating burners	Turbulent flames	Micro-combustors	Dynamic mechanism reduction	Diamond films	Soot morphology	Droplet combustion & hydrothermal reaction
	Break						
	Diagnostics	Turbulent premixed & partially premixed flame	Chemistry studies	Mechanisms reduction	Aluminum combustion	Soot modeling & Experiments	Droplet combustion
afternoon	Topical Review & Diagnostics	Thermo-acoustic-diffusion studies	Turbulent premixed flames	Ignition	Aluminum propellants	Soot chemistry studies	Spray & droplet combustion
	Break						
	New technology concepts	Transfer function	Turbulent stratified flames	Ignition	N/C interaction	Soot studies	Counterflow spray combustion
Work-in-Progress Presentations							
Friday	Plenary Lecture: Detonation in gases, E. Shepherd						
morning	Turbulent premixed & partially premixed flame	Diagnostics	Flame vortex interactions	Iron	Ignition	New technology concepts	Spray combustion
	Break						
	Turbulent premixed flame	Diagnostics	Ignition & extinction	Heterogeneous /homogenous combustion	Fuels-kinetic modeling	Spark ignition engines	Spray combustion-DNS & modeling
Afternoon	Flame studies	Diagnostics-CARS	Turbulent flames	Heterogeneous studies	Laminar premixed flame studies	Swirling flames	Spray combustion-LES & modeling
	Break						
	Laser-induced phenomena	Diagnostics-Diode laser	Turbulent premixed flames	Biomass	Pyrolysis	H_2/CH_4 blends	Plasma-aided combustion
Work-in-Progress presentations							

由本人與成大航太所趙怡欽老師及其研究生共同發表之論文分別被安排在第三天(八月六日)上午由博士候選人林河川口頭報告及第五天(八月八日)下午以海報展示方式進行，題目分別是兩平行預混甲烷火焰貧油燃燒交互作用之廣泛研究(A comprehensive study of two interactive parallel premixed methane flames on lean combustion)及紊流甲烷/一氧化碳噴流火焰熄滅現象之研究(A study of blowout phenomena of turbulent CH_4/CO jet flames)。兩篇論文發表時皆獲得很多位與會學者專家的興趣。由於國際燃燒會議出版的論文集(Proceedings of the Combustion Institute)在2006年時被ISI取消而沒列入SCI期刊等級，以致於今年的研討會投稿件數大降，本人也是因為這原因而沒有再撰寫文投稿。在國際燃燒學會於2007年聘請律師對ISI提出告訴之後，ISI決定將國際燃燒會議出版的論文集恢復列入SCI期刊等級，而此論文集之2007年Impact Factor則為2.647，此Impact Factor高於燃燒著名期刊Combustion and Flame之Impact Factor，由此可見國際燃燒會議所出版之論文集的重要性，相信在經過此事件之後，下一屆之研討會將會有更踴躍的投稿件數。

二、 與會心得

這次會議是由 McGill 大學負責主辦，由於 McGill 大學的大型會議室較分散，從這個 Session 結束要到下一個 Session 聽報告需要花較多的時間，同時海報展示之張貼會場離主會場也較遠，因此聽到不少抱怨聲。同時由這次會議讓我覺得從事燃燒實驗或是數值模擬研究已走向合作研究的方向，尤其是光學量測燃燒流場的研究更非合作不可，昂貴儀器設備的購買與維護已不再是每個研究單位都可負擔，共同合作一起發表論文才能提升我們的學術國際聲望。

三、**考察參觀活動**

無

四、**建議**

感謝國科會對出席國際研討會的補助，希望國科會能繼續補助國內學者參加國際燃燒相關會議，期盼有朝一日我們亦能在台灣舉辦此類會議。

五、**攜回資料名稱及內容**

此次會議所攜回的資料是與會者通訊錄及海報摘要各一本。

Available online at www.sciencedirect.com
ScienceDirect
ELSEVIER
Proceedings of the Combustion Institute xxx (2009) xxx–xxx
Proceedings of the Combustion Institute
www.elsevier.com/locate/proci

A comprehensive study of two interactive parallel premixed methane flames on lean combustion

Ho-Chuan Lin [a], Tsarng-Sheng Cheng [b], Bi-Chian Chen [a], Chun-Chin Ho [a], Yei -Chin Chao [a,*]

[a] *Institute of Aeronautics and Astronautics, National Cheng Kung University, Tainan 701, Taiwan, ROC*
[b] *Department of Mechanical Engineering, Chung Hua University, Hsinchu 300, Taiwan, ROC*

Abstract

This study aims to investigate interactive parallel lean premixed methane flames issued from twin rectangular slot burners with variable jet spacing, equivalence ratios and inlet speeds. The flowfield and combustion chemical reactions are predicted by detailed numerical simulation with Skeletal and GRI-v3.0 mechanisms. Numerical results such as velocity streamlines, temperature, flame height and flame shape are validated with those obtained by experimental particle image velocimetry (PIV) and flame measurements. When moved closer beyond a threshold jet spacing, these twin flames become interactive and both flames tilt outward in appearance with a wider operational range of lean and velocity conditions. Numerical predictions of flowfields found that there are three different interacting stages: entrainment, recirculation and reverse flows according to jet-to-jet spacing and they are named by their characteristic postflame flowfields between jet burners. At the reverse flow stage, a stagnating flowfield termed lateral impingement is generated along the symmetric axis between the flames, which is similar but not identical to that found in the counter-flow flames. As the jet spacing is reduced, the flowfield transition of the interacting postflame stages is believed to be the main mechanism to enhance the flame stabilization, especially in lean conditions. This reverse flow pattern provides a hot and slow postflame flowfield and transports the residual OH radicals from the main flames to heat and burn the fuel escaping from the stand-off gap between the flame base and burner rim through low temperature burning process. In other words, the stabilization of the interactive twin flames is enhanced by a number of crucial factors such as lateral stagnating flow, low dissipation of thermal and interacting chemical species supplied from the main flames.

Keywords: Lean combustion; Lateral impingement; Stagnating flow and interactive flames

---

1. Introduction

Lean combustion is generally considered as a timely solution to the more stringent environmental regulations and global weather concerns in a new era. However, the instability associated with the lean flame significantly keeps the lean combustion technique from being widely accepted as a major combustion technique for general applications. The past studies indicate some methods to improve the combustion instability such as vortex [1], swirling, interacting side-by-side diffusion burner array or matrix [2], hydrogen addition [3,4]

---

[*] Corresponding author. Fax: +886 6 238 9940.
E-mail address: ycchao@mail.ncku.edu.tw (Y.-C. Chao).

1540-7489/$ - see front matter © 2009 The Combustion Institute. Published by Elsevier Inc. All rights reserved.
doi:10.1016/j.proci.2008.07.030

Please cite this article in press as: H.-C. Lin et al., *Proc. Combust. Inst.* (2009), doi:10.1016/j.proci.2008.07.030

and reactor temperature oscillation [5]. The first two combustion techniques improve the flame instability by means of flow oscillation resonance and transverse wash of swirling flow to the adjacent flames respectively. The swirling flow is a typical flowfield for gas turbines but it is not common for other applications and the flame oscillation is likely limited to a specific situation. The third one uses side-by-side jet array to create an interactive hydrodynamic effect to generate vortex or flow recirculation between the jets and broaden the blow-out limits. However, the difficulty of oxygen supply does create a limit to bring these two diffusion flames in an even shorter jet spacing so the enhancement of extending blowout limit is not as good as expected. Therefore this method works very well only to certain jet spacing as reported. The fourth method attracts more attention recently because it also improves the NO_x emission. Nevertheless, the cost of hydrogen is quite high. From the preceding reviews, this study suggests the side-by-side jet array as a reasonable solution to the stability problem associated with lean premixed flames.

Jet flame arrays impinging upon a surface were widely reported by the researchers [6–8]. Their focuses are on the heat transfer coefficients of the span-wise stream and the impingement surface as well as the heat transfer rate of flowfield velocity, turbulence and convection. Recently research papers [9–15] addressed the effects of jet-to-jet spacing and nozzle-to-plate distance on the heat transfer of jet flame arrays impinging upon a surface, which is not the concern of this paper though, but they did notice the tilted flame shape caused by a positive pressure gradient at the interacting site. However, this positive pressure gradient was not appreciated and discussed further owing to different research objectives of these studies. For burner arrays, Kimura and Ukawa [16] and Singer [17] revealed the combustion characteristics of the two-dimensional rectangular burner. Menon and Gollahali [18,19] studied the interaction of multiple jet flames in still air and crossflow. Roper [20] reported the interactions of two laminar jet diffusion flames. Recently, Seigo et al. [21] studied the flame characteristics of low load rich-lean burner. Most of the research mentioned above emphasized on the interactions of the jet diffusion flames but scant attention is paid to the flame structure, operation characteristics and stabilization mechanism of the interactive premixed flames on lean combustion. Thus, such interactive features deserve further studies.

On top of the previous studies [22,23] on stability limits of interactive flames, the present study intends to explore the detailed flame structure and stabilization mechanism of interactive twin jet flames, based on the measurements of flow and thermal field and detailed numerical simulation of flame speed, heat release rate and chemical reactions on lean combustion conditions. To simplify the interactive premixed flames for numerical and experimental studies we used two 50 mm × 5 mm rectangular slot burners to investigate the effects of the jet-to-jet spacing, inlet speed and equivalence ratio between the two burners.

2. Experimental setup

The experimental apparatus is shown in Fig. 1. The aluminum slot burner is 160 mm in height with rectangular exit made of 1 mm thick wall and opened to an inside cross-sectional dimension of 5 mm (called “d”) by 50 mm. Both stainless steel meshes and ceramic rectifiers were used to straighten the flowfield. The flow in the vicinity of the burner exit was a fully developed velocity profile verified by particle image velocimetry (PIV) measurement. There was no inert gas sheath flow around the burners. Methane and air metered by electronic flow meters were premixed and guided into a manifold where the mixture was divided equally to two jets. Twin flames set in dimensionless jet spacing $L/d = 2 \sim 6$ were investigated in mean inlet flow velocities ranging from 0.7 to 3 m/s and equivalence ratio ϕ was in the range of 0.55–1.38. The temperature distributions were measured by thermocouples, and the global flame appearance was captured by a digital CCD camera. The flowfield of the interactive flames was carefully examined by using PIV technique.

Figure 1 shows the current PIV experimental setup for flow and postflame field velocity measurements. This PIV digital camera was equipped with a mechanical shutter to prevent the PIV image from flame-illumination contamination. The measurement system was made up of two Nd: YAG lasers, a digital CCD camera, a pulse generator, a mechanical shutter and a controller. This laser system possessed two Q-switched Nd: YAG pulse lasers (LOTIS TII) lasing at the fundamental wavelength (1064 nm) and second harmonic (532 nm). The wavelength of 532 nm was utilized for whole-field illumination and the maximum pulse energy was 170 mJ. A high-resolution and high-performance digital CCD camera (**sharpVISION**™) was used. Each image contained 1024 × 1280 pixels, which rendered a spatial resolution of 6.7 μm/pixel in the setup. The inter-frame time for double-shutter mode could go as low as 200 ns.

3. Numerical method

To numerically simulate the laminar premixed methane twin flames, the relevant governing equations were solved by using the commercial package ESI-CFD for flow, heat transfer and chemistry/mixing computations. A flame-zone

Please cite this article in press as: H.-C. Lin et al., *Proc. Combust. Inst.* (2009), doi:10.1016/j.proci.2008.07.030

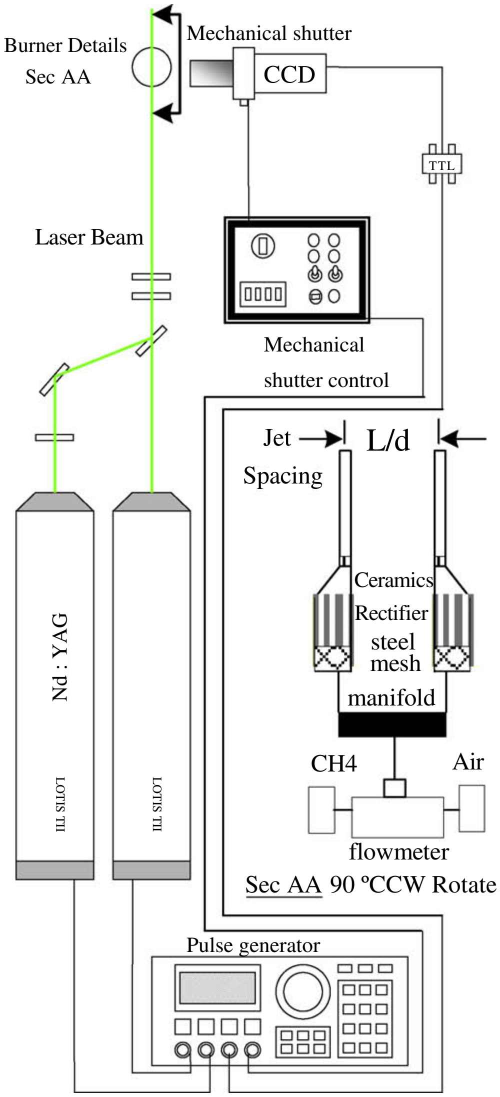

Fig. 1. Experimental apparatus.

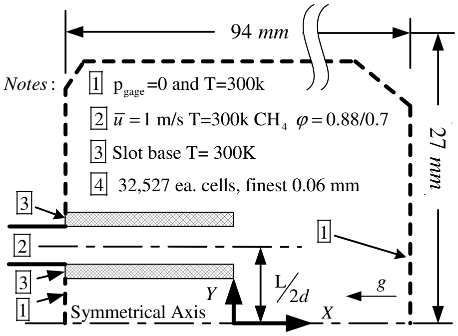

Fig. 2. Illustration of CFD computational domain and boundary conditions.

reinforced grid system was used to solve the discretized equations with a control volume formulation in accordance with the SIMPLEC algorithm as shown in Fig. 2. The inlet and boundary conditions are shown in Fig. 2. The surrounding boundary condition marked with was set as gage static pressure $p = 0$, temperature of 300 k and chemical mixture of pure air in case of flow-into-system situation. The burner inlet marked was set as a uniform velocity profile of 1 m/s, temperature of 300 k and contained methane–air mixture of equivalence ratio of 0.88 or 0.7. The burner end surface marked with was set as constant temperature of 300 k. The rest portion of the burner located inside the computational domain was conjugated into the whole calculation with material specification of aluminum alloy with density of 2700 kg/m^3, specific heat of 880 J/kg k and thermal conductivity of 190 W/m k but the wall effect model was not specified. Symmetric condition was applied at the symmetric axis in the lower boundary of the Fig. 2. All of the governing equations were solved by using the second-order scheme except the velocity equation handled by second-order plus 50% upwind scheme. Input of the molecular transport data was obtained from the CHEMKIN Rev. 3.0 package. In order to save the computational time, we started with Skeletal mechanism and followed by GRI Rev. 3.0 package for preliminary and detailed calculations respectively. The radiation effect had not been embodied into current numerical calculation due to the limited contribution.

4. Results and discussion

4.1. Flame configuration versus equivalence ratio and inlet speed

Figure 3 shows 13 pairs of interactive flames side-by-side with jet-to-jet spacing $L/d = 2$ burning at equivalence ratio of 0.55, 0.6, 0.65, 0.7, 0.75, 0.8, 0.88, 0.98, 1.06, 1.14, 1.2, 1.28, and 1.38 respectively from left to right. As shown in middle part of Fig. 3 each pair of flames expels each other and looks like an “M-shape” flame on the mild lean area. They form a conical or up-side-down “U-shape” flame [1] as equivalence ratio goes richer than 1.4 and the inboard rim flames are lifted off. The “V-shape” flame consists of two half lift-off flames anchored on inboard side of each burner only on the extremely lean combustion. Figure 3 also shows that the $L/d = 2$ burners can sustain a flame even when the equivalence ratio goes lower than 0.55, lower than the ordinary flammability limit. As illustrated in Fig. 4 the flame offset angle is defined by the ratio of the offset distance of flame tip from jet central axis to the flame height. The offset angle becomes

Please cite this article in press as: H.-C. Lin et al., *Proc. Combust. Inst.* (2009), doi:10.1016/j.proci.2008.07.030

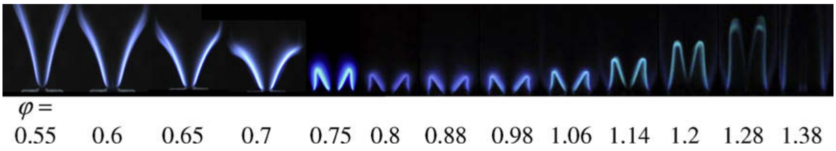

Fig. 3. Flame configurations vs. equivalence ratios.

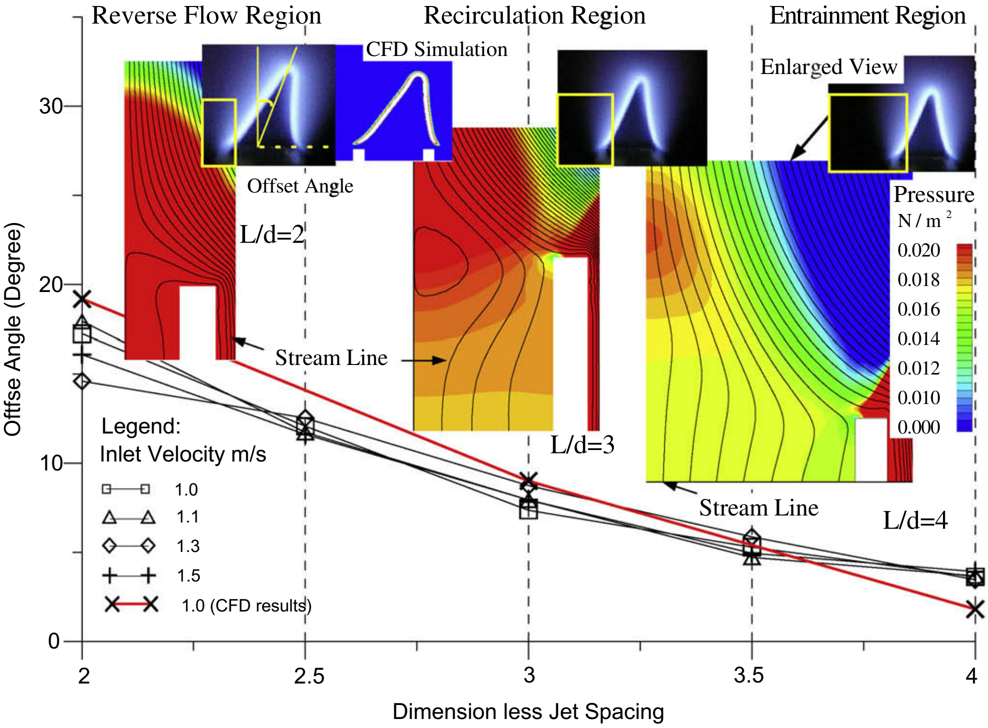

Fig. 4. Effects of jet-to-jet spacing on flame and flowfield characteristics.

larger or the flame tilts outward more as the burners approach each other from jet spacing of $L/d = 4$, 3.5, 3, 2.5 and all the way down to 2. Figure 4 shows that there is no apparent change to the offset angle accompanied with the variation of inlet speed from 1.0 to 1.5 m/s. The only difference is the flame height getting taller along increasing of the inlet speed.

4.2. Validation and deviation of computational results

To look further into this premixed twin flame interaction, interested cases were numerically simulated and their calculated pressure distributions and stream lines were presented in Fig. 4 for $L/d = 2$, 3 and 4. Because of the symmetrical nature of twin flames it is practical to just show one flame image out of the twin interactive flames in Fig. 4. To validate the computational flame shape with the experimental one, a drawing of the simulated flame heat release rate was placed side-by-side to the photographic image of the real flame operated at an identical condition on the left top corner of Fig. 4. It is very promising of this comparison in terms of the flame shape and the offset angle between these two pictures. However the highest flame temperature of CFD calculation is 2080 K, much higher than the experimental measurement of 1800 K for the $L/d = 2$ case. And the predicted flame height by numerical simulation is only 0.3 mm shorter than the photo flame.

4.3. Entrainment, recirculation and reverse flows

The flowfields near the inboard gap were numerically investigated and the flame base areas circled with yellow frames were carefully trimmed and enlarged in Fig. 4. As noted, the computed postflame streamline patterns changed when the jet spacing was reduced. The variation of the flow pattern in the inboard gap is believed to be

Please cite this article in press as: H.-C. Lin et al., *Proc. Combust. Inst.* (2009), doi:10.1016/j.proci.2008.07.030

strongly related with the enhancement of the inboard flame stabilization, especially for lean conditions. Along the decrease of jet spacing from $L/d = 4$–2, the flowfield near the inboard gap changed from entrainment flow for $L/d = 4$, recirculation flow for $L/d = 3$, and finally up to an "impingement" reverse flow for $L/d = 2$. The "impingement" reverse flow depicts a characteristic stagnating flow. The postflame flowfield for the $L/d = 4$ flame has a streamline pattern as straightforward as that of an ordinary postflame flow entraining the ambient air into the symmetric axis except a less pronounced local pressure peak outstanding from the yellow background. This local pressure peak is due to the limited space in this minor impinging area. For the case of $L/d = 3$, a local recirculation region of entrained flow at the symmetric axis is formed and the pressure peak at the symmetric axis becomes pronounced, pushing the flame outward more. When the jet spacing is $L/d = 2$, the postflame streamlines impinge each other severely and a reverse flow is generated, creating a flame and a flowfield structure similar to those found in the counter-flow flame. At this case entrainment of ambient air is completely blocked.

4.4. Flame stabilization and lateral impingement

The counter-flow can also create a hydrodynamic effect to enhance the flame stabilization. It [24] reported that a counter-flow flame can burn methane–air mixture with an equivalence ratio as lean as of 0.45. Figure 5 shows the lateral impingement demonstrated by overlapping streamlines and PIV uniform vectors in the background of the X_{OH} (left two pictures) and X_{CO} (right one) mole concentration. The three blank rectangular areas represent the left three burner rims of the twin jet burners at the jet spacing of $L/d = 2$. The origin of x-axis is located just right on the symmetrical line and that of y-axis is lined up with the tip of the rim. It also shows the calculated streamlines and the first three streamlines designated as IB-1, IB-2 and IB-3 for inboard rim and OB-1, OB-2 and OB-3 for outboard one respectively.

This impingement area has an obvious stagnation point and the computed streamlines were carefully verified by the PIV measurement as denoted in uniform velocity vectors (show only the direction) in the middle picture of Fig. 5. This effect can be designated as a lateral or an angled counter-flow and classified as a typical stagnation-flow flame. The differences between the inboard and outboard regions in the flowfield pattern significantly affect the characteristics of the flame and the reaction near the burner rim as depicted by the color-coded OH and CO concentration distributions in Fig. 5. The characteristics of the thermal and the flame near the burner rim will directly influence the flame stabilization. The inboard side has a taper-down flow velocity and taper-up static pressure flowfield as shown in Fig. 6 and the flow velocity needs to be reduced to around zero at the impinged point within a relatively short distance. Therefore in Fig. 6 the velocity magnitude of the entire inboard side is reduced while that of the outboard side is accelerated. The temperature along the streamlines IB-2 and IB-3 goes up between the streamline coordinate of 2 and 3 mm in the postflame of the gap region. These characteristics of the reduced velocity and the increasing temperature in the postflame provide extended residence time and richer chemical species, which in turn favor the combustion process in this region.

4.5. Calculated wall proximity effect of HO_2, H_2O_2

In addition to the flame stabilization discussed above, the calculated near-wall behaviors of the HO_2 and $H_2O_2$and their contributions to the flame stabilization near the inboard burner rim are illustrated in Fig. 7, called the wall proximity

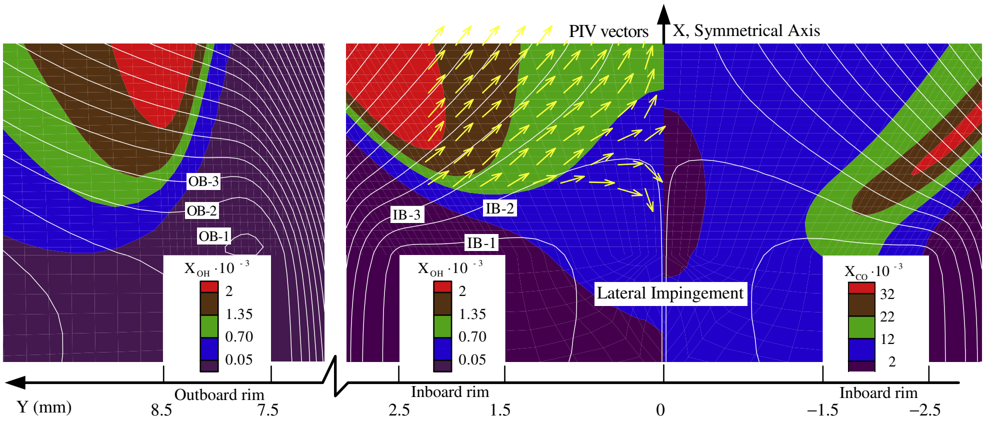

Fig. 5. Lateral impingement demonstrated by stream lines with OH and CO mole concentration background.

Please cite this article in press as: H.-C. Lin et al., *Proc. Combust. Inst.* (2009), doi:10.1016/j.proci.2008.07.030

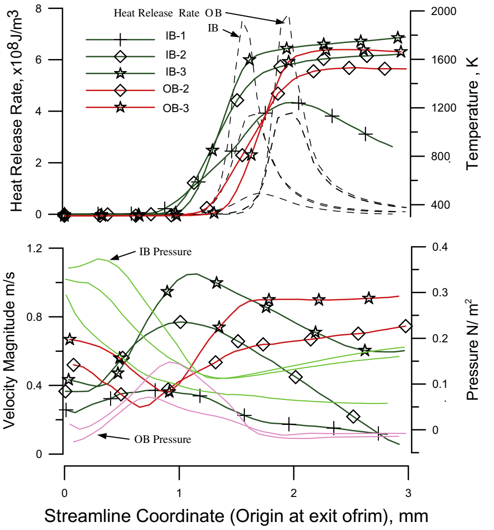

Fig. 6. Physical stabilization mechanisms by flow and thermal field along stream lines.

effect. The near-wall effect and low temperature reaction mechanism become important in the wall proximity region between the burners. Figure 7 indicates that the HO_2 concentration isopleth fades from level 5 of the main flame (left-upper corner of the picture) down to level 4 near the streamline IB-2 but rises back up to level 5 near the rim wall. In the meantime it is found that a pool of H_2O_2 builds up thicker and thicker between the streamline IB-1 and the rim wall of the burner. This H_2O_2 pool is generated by the promoted reaction of $2HO_2 \rightarrow O_2 + H_2O_2$ when HO_2 concentration becomes higher in the low temperature background near the rim. The H_2O_2 pool here works like storage of HO_2 as well as a more effective form for optimizing the HO_2 gathering effect. The OH concentration in one spot of the IB-1 streamline is rich enough to support the reaction of $OH + CH_4 \rightarrow CH_3 + H_2O$ because of the additional supply from stored HO_2 and H_2O_2 through the reactions of $H + HO_2 \rightarrow 2OH$ and $H + H_2O_2 \rightarrow H_2O +$ OH. As shown in Fig. 5, the surplus of inboard OH mole fraction is extended deeply into the gap of the two burners along the reverse flow, which implies a high temperature zone with active chemical species does exist between the two flames and provides an environment to stabilize the flame. As observed, the weighting of heat release contribution shifts from reaction of $OH + CH_4 \rightarrow CH_3 + H_2O$ to $HO_2 + CH_3 \rightarrow OH + CH_3O$ in the jet-to-jet gap area. This inboard wall proximity effect also helps many other chemical species as long as they can form an effective proximity area or a closed angle shape by the rim tip and the main flame concentration band. In this work those species are CH_3O, CH_3OH, C_2H_2, C_2H_4, C_2H_6, C_3H_8, CH_2O, H_2 and CO. As noted, the OH radical is not in the list above so the mole fraction of OH is reduced near the burner rim area since there is no wall proximity effect for OH. Fortunately this reduction of OH concentration fills up by the stored $HO_2$and H_2O_2. After all, the discussion mentioned above is based on the calculation findings which were physically validated with the temperature measured by thermal couple, the pictures of the flame shape and the flow fields of PIV measurement. In other words, all of the chemicals with wall proximity effect could have certain deviation in respect to quantitative aspect.

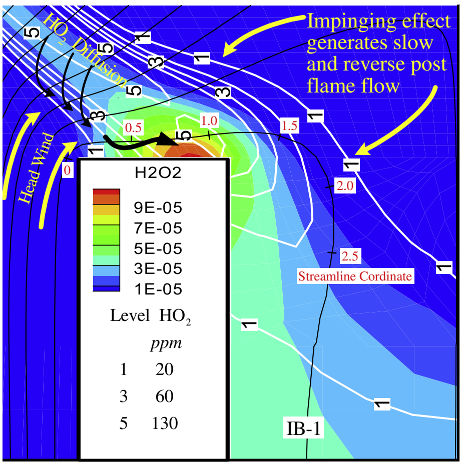

Fig. 7. Chemical aspect of wall proximity effect of HO_2 and H_2O_2.

In summary of the stabilization mechanism of the twin interactive flames, a schematic drawing compared the inboard and outboard flame stabilization was presented in Fig. 8 at the jet spacing of 2d and the reverse flow stage. At the reverse flow stage, a stagnating flowfield, termed lateral impingement, is generated along the symmetric axis between the flames, similar to that found in the opposed counter flames but the temperature is cooler than that of the vertical opposed jets. The transition of the postflame flowfield, at the short jet spacing scenario, is believed to be the main mechanism to enhance the flame stabilization, especially in lean conditions. By regulating the amount of entrainment flow, this lateral impingement flowfield provides a zone with low dissipation of both the heat and the chemical species in this area, which would favor the flame stabilization. The wall proximity effect also turns HO_2 into H_2O_2 to accommodate more incoming HO_2 leading to additional OH supply for the combustion. The OH radicals are diffused and transported by the reverse flow into the impinging area and react with the escaping fuel to generate the additional heat in the gap region. It dramatically helps the flame base to be stabilized near

Please cite this article in press as: H.-C. Lin et al., *Proc. Combust. Inst.* (2009), doi:10.1016/j.proci.2008.07.030

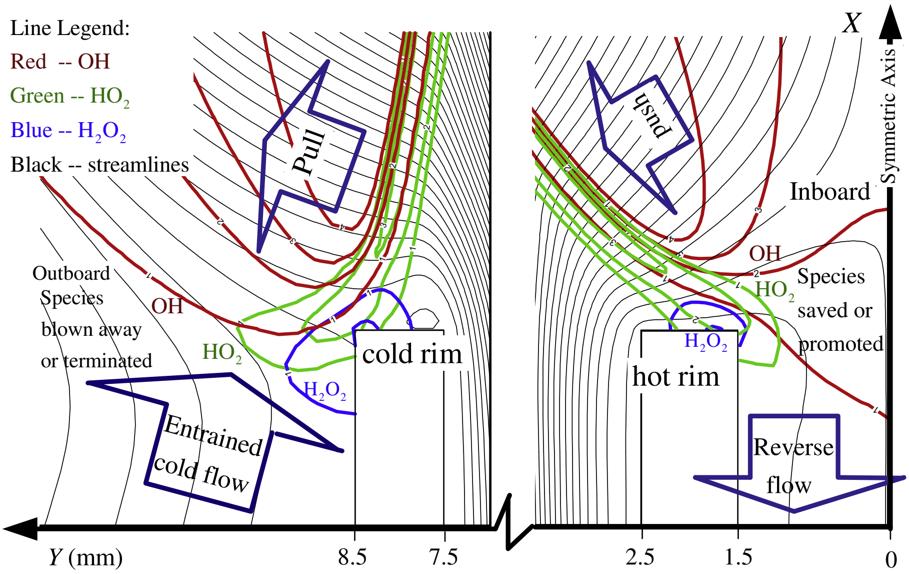

Fig. 8. Schematic comparison of the differences between inboard and outboard sides in respect of (1) heating or cooling burner rims, (2) cold entrained or hot reverse flows, and (3) blown away/cooling down or saved/promoted for chemical species.

the burner rim with the additional supply of OH, especially for lean combustion. On the contrary, the outboard flame, as shown in Fig. 8, suffers from the quench effect due to the cold entrainment flow which dissipates the heat as well as the active species near the rim tip.

5. Conclusions

This study is intended to look into the entire phenomenon of two lean premixed methane flames placed within interactive jet spacing. The parallel interactive premixed methane flames are identified numerically and experimentally as a phenomenon of lateral impingement of postflames or angled counter-flow flames. These parallel stagnation flames possess a few typical characteristics of counter-flow flames such as the flame stretching and the enhanced flame stabilization observed in this study. Besides, there are some new findings obtained to explain how the impingement flowfield in the gap region between the burners near the burner rim helps the stabilization of the flame in terms of hydrodynamic, thermal and chemical species contributions. This flame stabilization mechanism was comprehensively explained in this study.

References

[1] T. Schuller, D. Durox, S. Candel, *Combust. Flame* 135 (2003) 525–537.
[2] B.-J. Lee, J.-S. Kim, S. Lee, *Combust. Sci. Tech.* 176 (2004) 482–497.
[3] E.R. Hawkes, J.H. Chen, *Combust. Flame* 138 (2004) 242–258.
[4] J.-Y. Ren, F.N. Egolfopoulos, *Combust. Sci. Tech.* 174 (2002) 181–205.
[5] M. De Joannon, P. Sabia, A. Tregrossi, A. Cavaliere, 176 (2004) 769–783.
[6] R.N. Koopman, E.M. Sparrow, *Intl. J. Heat Mass Trans.* 19 (1976) 673–683.
[7] L.F.G. Geers, M.J. Tummers, K. Hanjalic, *Exp. Fluids* 36 (2004) 946–958.
[8] M. Can, A.B. Etemaglu, A. Avci, *Heat Mass Trans.* 38 (2002) 251–259.
[9] L.L. Dong, C.W. Leung, C.S. Cheung, *Intl. J. Heat Mass Trans.* 47 (2004) 489–500.
[10] L.L. Dong, C.W. Leung, C.S. Cheung, *Intl. J. Heat Mass Trans.* 46 (2003) 113–125.
[11] S. Chander, A. Ray, *Intl. J. Heat Mass Trans.* 50 (2007) 640–653.
[12] J. Wu, J. Seyed-Yagoobi, R.H. Page, *Combust. Flame* 125 (2001) 955–964.
[13] J.-Y. San, M.-D. Lai, *Intl. J. Heat Mass Trans.* 44 (2001) 3997–4007.
[14] S. Chander, A. Ray, *Energy Conver. Manage.* 46 (2005) 2803–2837.
[15] S. Chander, A. Ray, *Exp. H. Trans.* 19 (2006) 15–38.
[16] I. Kimura, H. Ukawa, Seventh Symposium (International) Combustion, *Combust. Inst.* (1956) 521–523.
[17] Singer, J.M., Fourth Symposium (International) Combustion, *Combust. Inst.* (1952) 352–358.
[18] R. Menon, S.R. Gollahalli, *ASME*, HTD Publ by ASME, New York,, 1985, pp. 45, 27–133..
[19] R. Menon, S.R. Gollahalli, *Combust. Sci. Tech.* 60 (1988) 375–389.

[20] F.G. Roper, *Combust. Flame* 34 (1979) 19–27.
[21] K. Seigo, H. Satoshi, U. Yoshito, M. Syuichi, A. Katsuo, 20th ICDERS, Canada, 2005.
[22] H.-C. Lin, B.-C. Chen, C.-C. Ho, Y.-C. Chao, Asia-Pacific Conference on Combustion, 2007.
[23] H.-C. Lin, B.-C. Chen, C.-C. Ho, Y.-C. Chao, 21st ICDERS, Poitiers, France, July 23–July 27, 2007.
[24] H. Guo, G.J. Smallwood, L. GülderÖ, *Proc. Combust. Inst.* 31 (2007) 1197–1204.

Please cite this article in press as: H.-C. Lin et al., *Proc. Combust. Inst.* (2009), doi:10.1016/j.proci.2008.07.030

A STUDY OF THE BLOWOUT PHENOMENA OF TURBUELNT CH_4/CO JET FLAMES

C. –Y. Wu[1], Y. –C. Chao[1], T. S. Cheng[2], Y. –S. Lien[1], Y. –Y. Cheng[1]

[1] *Department of Aeronautics and Astronautics, National Cheng Kung University, Taiwan ROC;*

[2] *Department of Mechanical Engineering, Chung Hua University, 300, Taiwan ROC*

ycchao@mail.ncku.edu.tw

Abstract

Flame stabilization which generally involves different combustion characteristics of fundamental properties is an important issue of fundamental combustor design. Due to the environmental threats and depletion of fossil fuel, two timely alternatives strategies which are either to improve the combustion efficiency with considerable reductions in the pollutant emissions into the atmosphere or more significantly to replace fossil fuel usage as much as possible with environmentally friendly, clean and renewable energy sources attract researcher's attention recently. Among the renewable energy sources, gasified biomass that contains a mixture of carbon monoxide, hydrogen and methane, together with carbon dioxide and nitrogen, is more versatile and attractive than the original solid biomass. The combustion characteristics of carbon monoxide, which is a major species in gasified biomass fuels, are different from those of hydrogen and other alkane. It has been shown that the addition of small amount of hydrogen or methane to CO flames increases the laminar flame speed and extinction strain rate by accelerating the main CO oxidation reaction. In the present study, the blowout velocities of the CH_4/CO blended fuels are theoretically and experimentally studied through phenomenological observation and the measured results are used to verify the existing theories of blowout. Furthermore, comparison of the measured results with theoretical predictions will be made to delineate the characteristics of blowout phenomena in turbulent jet flames.

The calculated and measured non-dimensional blowout out velocities of CH_4/CO turbulent diffusion flames are shown in Fig. 1. On the other hand, the calculated blowout parameters are shown in Fig. 2. Generally, blowout velocities of turbulent CH_4/CO diffusion jet flames still can be estimated by using universal formula which based on initial gas properties and the initial velocity at jet exit. The theoretically predicted stoichiometric contours of methane and carbon monoxide provide an explanation for the fact that the blowout velocities of turbulent CH_4/CO diffusion jet flames are mainly dominated by methane/air mixing.

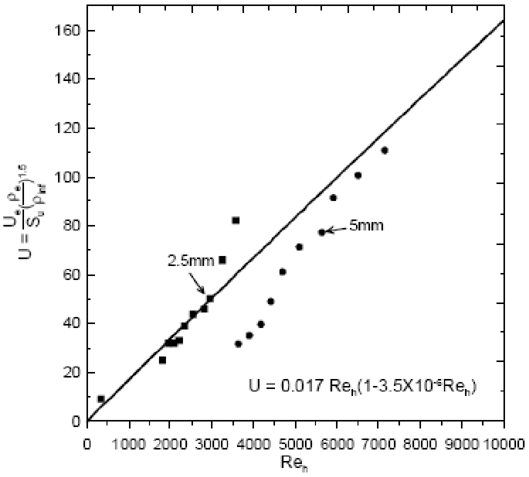

Fig. 1

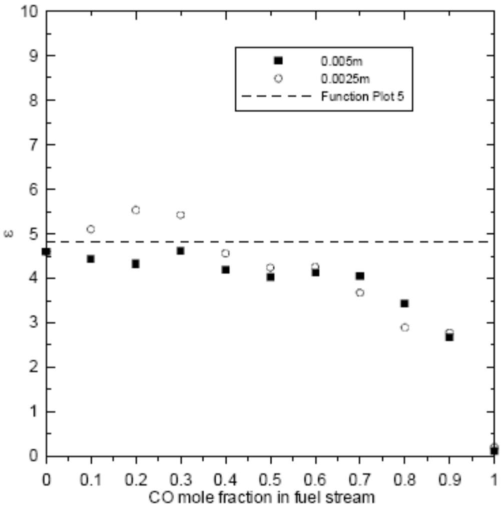

Fig. 2